UNIVERSITÁ DEGLI STUDI DI

CATANIA

International PhD in Chemical Sciences (XXX cycle)

Photoactivable Multimodal Antimicrobial Nanoconstructs

Author:

Marta PÉREZ-LLORET

Supervisor:

Prof. Salvatore SORTINO

A thesis submitted in fulfillment of the requirements

for the degree of Doctor of Philosophy

in the

Laboratory of Photochemistry

Department of Drug Sciences

Declaration of Authorship

I, Marta PÉREZ-LLORET, declare that this thesis titled, "Photoactivable Multimodal Antimicrobial Nanoconstructs" and the work presented in it are my own. I confirm that:

- This work was done wholly or mainly while in candidature for a research degree at this University.
- Where any part of this thesis has previously been submitted for a degree or any other qualification at this University or any other institution, this has been clearly stated.
- Where I have consulted the published work of others, this is always clearly attributed.
- Where I have quoted from the work of others, the source is always given. With the exception of such quotations, this thesis is entirely my own work.
- I have acknowledged all main sources of help.
- Where the thesis is based on work done by myself jointly with others, I have made clear exactly what was done by others and what I have contributed myself.

Signed:

_____

Date:

_____

"Prevention is better than cure."

Desiderius Erasmus (1466–1536)

Universitá Degli Studi di Catania

Abstract

Department of Drug Sciences

Doctor of Philosophy

Photoactivable Multimodal Antimicrobial Nanoconstructs

by Marta PÉREZ-LLORET

The search of novel antibacterial treatment modalities designed to face problems of antibiotic Multi Drug Resistance (MDR) associated with the alarmingly low turnover of new clinically approved antibiotic drugs is one of the main challenges in biomedicine. In this frame, the achievement of tailored systems able to release therapeutic agents in a controlled fashion is one of the growing area in the burgeoning field of nanomedicine. Light represents the most elegant and non-invasive trigger to deliver bio-active compounds on demand at the target site with superb control of three main factors, site, timing and dosage, determining for the therapeutic outcome. In addition, light triggering is biofriendly, provides fast reaction rates and offers the great benefit of not affecting physiological parameters such as temperature, pH and ionic strength, fundamental requisite for biomedical applications. Recent breakthroughs of nanotechnology offer the opportunity to characterize, manipulate and organize matter at the nanometer scale, controlling the size and shape of the resulting nanomaterials and greatly improving the biocompatibility and the cellular uptake efficiency. This thesis focuses on the design and fabrication of light-activated nanoconstructs for the controlled delivery of "unconventional" therapeutics such as reactive oxygen and nitrogen species, and heat which, in contrast to "conventional" drugs, do not suffer MDR problems and display reduced systemic effects. A range of nanosystems able to generate individually, sequentially or simultaneously the above cytotoxic agents is reported and, in

some case, their antibacterial activity is also investigated. This dissertation is divided in two sections: the first one regards nanomaterials, while the second focuses on molecular hybrid systems, all preceded by a brief in-troduction.

Contents

Dedicated to my family

Chapter 1

Introduction

1.1 Introduction to the PhD dissertation

Looking back, the discovery of new antibiotics was always succeeded by their complementary resistance. Before even been commercialized in 1942, some organisms were discovered being resistant to penicillin in 1941[1]. Thanks to the misuse of antibiotics, together with the natural evolution of microorganisms to survive in extreme environments, multidrug resistance (MDR) is spreading faster than the introduction of new compounds into the market, putting society into an emergency situation. The dwindling of conventional antibacterial drugs and the spread of organisms presenting MDR will be the cause the next global health crisis. The last family of antibiotics being discovered was daptomycin a lipopeptide-based drug, back in 1987[2]. After almost twenty years of discovery void, in 2015 a potential new class of antibiotic appeared with the breakthrough of teixobactin[4]. The main drawback of antibiotics pushed scientific community to look for unconventional strategies to fight superbugs.

1.2 Multi Drug Resistance

International health institutions are concerned about the upcoming situation, which was defined as "catastrophic". As the WHO's assistant director-general for health systems and

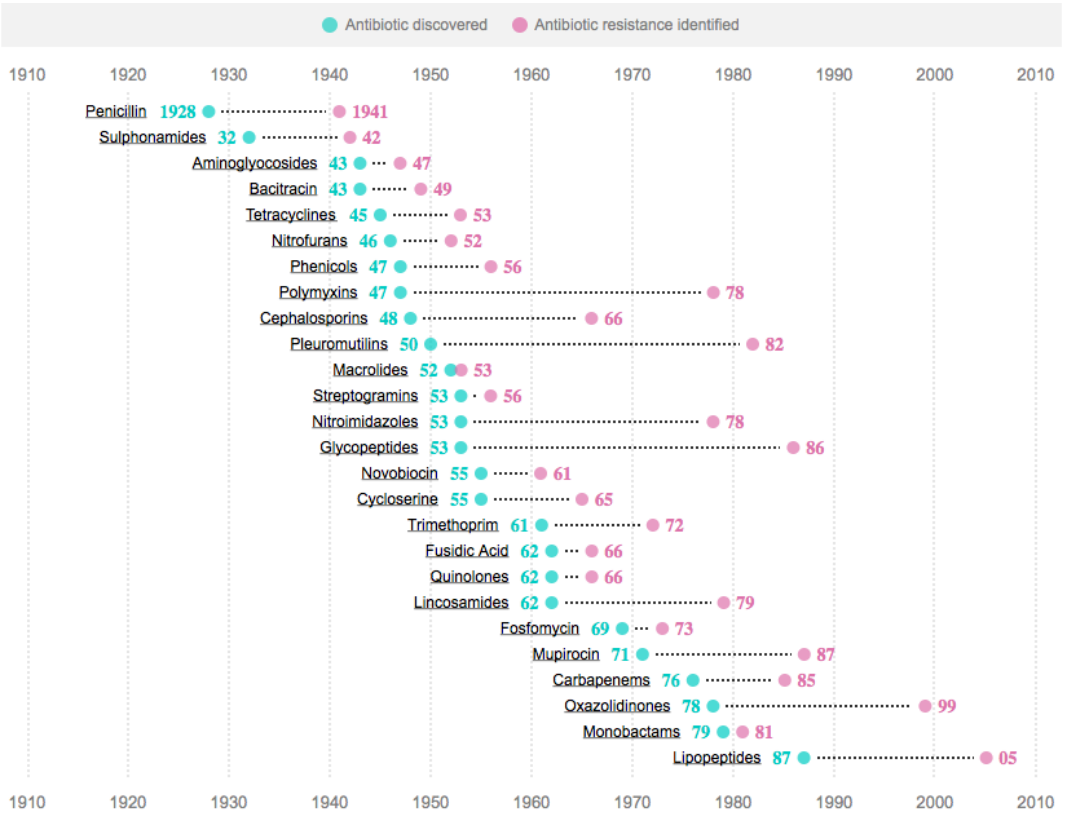

FIGURE 1.1: History of antibiotic resistance[3]

innovation, Marie-Paule Kieny said, "Antibiotic resistance is growing, and we are fast running out of treatment options".

The misuse of antibiotics, in addition with the lack of regulation about their prescription in several countries[5], accelerated the proliferation of antibiotic resistant bacteria. One of the most famous characters of this dramatic situation is *mycobacterium tuberculosis*; this particular strain is responsible of most tuberculosis (TB) cases in humans. Its resistance was even classified into three levels according to case severity:

- MDR, resistant to at least isoniazid and rifampicin
- Extensively drug-resistant (XDR), resistant to any of the fluoroquinolones (such as levofloxacin or moxifloxacin) and to at least one of the three injectable second-line

drugs (amikacin, capreomycin or kanamycin)[6]

- Total drug-resistance (TDR)[7]

Despite DR seems to be exclusive of bacteria, in fact is an emerging phenomenon present also in infectious diseases (VIH), or even cancer[8]. The main mechanisms of drug resistance (DR) are:

- Drug inactivation or modification
- Alteration of the target site of the drug
- Modification of metabolic pathways
- Drug efflux pomp[9]

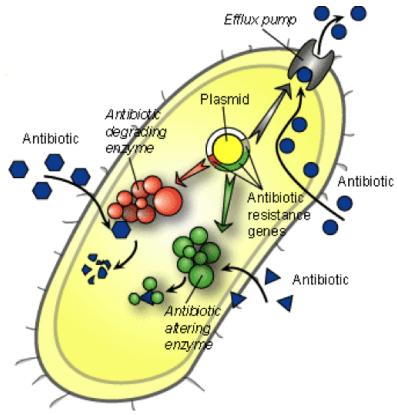

FIGURE 1.2: Scheme of Bacteria Pump mechanism.

The cost of DR is estimated in 50 000 people, just in Europe and USA. Obtaining a world-wide cypher is a challenge due to the miss of data in several countries, but the lower estimation is around 700 000 of people a year[10]. Most worrisome is that in the next 35 years, another 300 million people are expected to die by DR. Moreover, the economic impact of this upcoming crisis is trying to be calculated too. Hospital-acquired infections (HAI), also known as nosocomial infections, seems cost more to hospital than the disease which drive the patient to the hospital in first place. It is difficult to estimate the cost impact of HAI.

Hospital fees may considerably change depending on the country, for instance, the price of treating TB in USA costs 80 times more than in India[11]. In order to have an idea of this

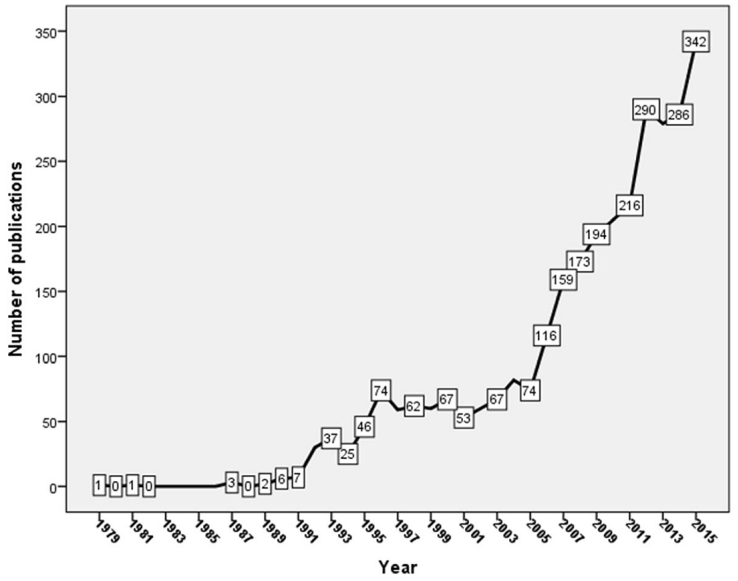

FIGURE 1.3: Growth of publications on MDR, XDR and TDR-TB in the past four decades[3]

amount, several studies have been followed in different hospitals around the world, and the increase can vary from 1 000 $ to more than 100 000 $ per patient, depending on the case and the country[12]. Other studies are more general, and talk about a frightening reduction of the gross domestic product (GDP): by 2050, 1,1% lost in the low-impact scenario and 3,8% in the high-impact[11]. But not only superbugs are spreading, the research on the field is booming too. The number of articles published concerning DR increased exponentially in the last ten years (Figure 1.3). This issue pushed also the scientific community to collaborate across countries and institutions more than usual.

1.3 Nanotechnology in medicine

The use of nanotechnology in medicine started in the 90's thanks to the development of devices that allowed observing and manipulating at nanometric scale. Since the discovery

of nanomaterials, scientific community has been shocked to observe size (and shape) dependant behave: a bridge between bulk materials and atomic structures. Sometimes, those unexpected proprieties are due to the increase of surface/volume ratio. The list of size dependant proprieties seems endless: optical, conductivity, magnetism, solubility... This discovery pushed scientists finding new applications for those "new materials". As well as biological process works at microscale, nanomaterials were founded to be the perfect tool to improve the understanding of human body. Particularly in the case that concerns us, nanotechnology represents a new era of drug delivery. This idea of "vehiculization", which sounds as a science fiction movie, is actually possible thanks to nanotechnology. Different materials with all kind of proprieties are exploited to this goal. The choice of the type of carrier will is correlated with the application until a final ideal nanostructure will be discovered. Meanwhile, several type materials have been enjoyed for this aim, the most common examples are liposomes[13], polymer-drug conjugates[14], micelles[15] and nanoparticles (NPs)[16].

Some advantages against classical carriers are their capacity to carry non-soluble or hydrophobic drugs into the cells, giving a second chance to drugs discarded years ago due to water insolubility. They are also able to control the drug pharmacokinetics[17]. Furthermore, the possibility of target release decreases the effective dose, and minimizes toxic side effects of drugs. Most of those nanocarriers are designed to have stimuli responsive release. Controlled release can be carried out enjoying several triggers, such pH, magnetic proprieties, or like in our case, light[18].

All those customizable parameters lead into a new era of medicine, where pharmaceuticals drugs will be more specific, less toxic, with lower dosage, and with better imaging. By reducing the concentration of drug administration, side effects will be reduced too, but not only for the patient health, also at environmental level. Another emerging issue nowadays is environmental contamination due to pharmaceuticals and personal care products (PPCPs)[19]. Naturally, studies are being conducted also to understand better how nanomaterials interact with environment, to minimize or even avoid the side effects.

This new generation of pharmaceutical drugs is supposed to be more “smart”, more ecological and environmental friendly, but also able to be more and more specific.

1.4 Light based strategies

1.4.1 Photodynamic Therapy

Even if light therapy was known since antiquity, the first report goes back to the beginning of the last century, thanks to the studies of Hermann von Tappeiner, who coined the term "photodynamic reaction". He conducted the first experiments on photodynamic therapay, via the topical application of photosensitive dye to skin diseases, and posterior exposure to light[20]. It was not until the 1970’s when photodynamic therapy started to be consider a suitable choice for disease treatments.

Light interaction with living cells can lead to survival or death. The most representative examples of this fact are plants and Porphyria. Both enjoy the power of photosensitizers (PS), which are molecules able to absorb light and excite molecular oxygen from a triplet state to a singlet. In the case of plants, this high oxidative transient molecule is enjoyed to produce energy, but in the cases of Porphyria, produces skin damage.

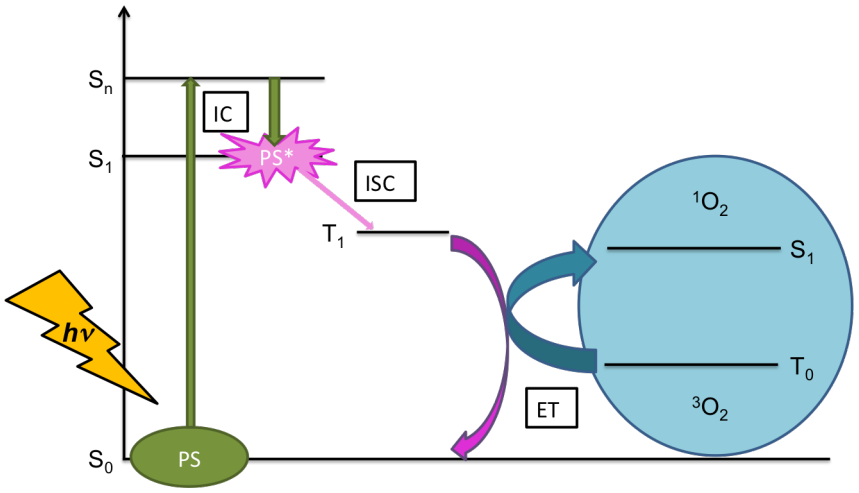

FIGURE 1.4: Mechanism for photosensitization of $^1O_2$

When PS is irradiated at an adequate wavelength, it gets excited from a singlet ground state (S_0) to superior level (S_n). Then, through internal conversion (IC), PS* relaxes back to first excited level S_1, where the transition to triplet excited state (T_1) is allowed, and results thanks to intersystem crossing (ISC). In the presence of molecular oxygen, energy transfer (ET) from PS* promotes oxygen from ground energy level T_0 to an excited level, S_1. All the process leads to the formation of $^1O_2$, a high reactive molecule from the family of reactive oxygen species (ROS).

This powerful oxidizing photoproduct has a short life time (μs) but also a short range of diffusion in cellular environment (up to 150 nm), producing irreversible damage to biological substrates of different nature: proteins, lipids and nucleic acids. In fact, this lack of specificity has been observed when regular bacteria and MDR bacteria were treated, showing no significant differences between them. Among all ROS, only $^1O_2$ is able to inactivate antioxidant enzymes, like catalase and superoxide dismutase[21]. In addition, repeated photosensitization does not increase drug resistance[22], making PDT an interesting tool to fight superbugs.

1.4.2 Nitric Oxide-based therapy

Nitric oxide (NO) used to have the status of pollutant gas, until 30 years ago. When it was shown to be produced naturally in the body, the interest of this molecule increased, leading to more studies and better understanding of its biological role in mammalians. Only a couple of years later, it received the award of "molecule of the year", organized by The American Association for the Advancement of Science[23]. Nitric oxide, known as an endothelium-derived relaxing factor (EDRF), has a key role in vasodilation, neurotransmission, immune system and penis erection[24]. This last discovery produced the most profitable drug of the history: sildenafil, commonly known as Viagra[25]. NO generation by phagocytes elicited interest on its possible application as antibacterial, tumoricidal, and other infectious diseases, since is also able to block viral replication[26].

This ephemeral inorganic free radical has half-life in tissues of ca. 5 s and diffuses in the range of 40-200 μm. Inasmuch as NO is a gas, how to store and delivery was challenging. Fortunately, several molecules have been design to face this issue[27]. Because its dosage-dependent effect, it is primordial to have a control-release system. The 4-nitro-3-(trifluoromethyl) aniline derivates developed in Prof. Sortino's group[28] allows the production of NO only under light stimulation trough a nitro-to- nitrite rearrangement (Figure 1.5), that generates a non-toxic and non-absorbing in visible region photoproduct.

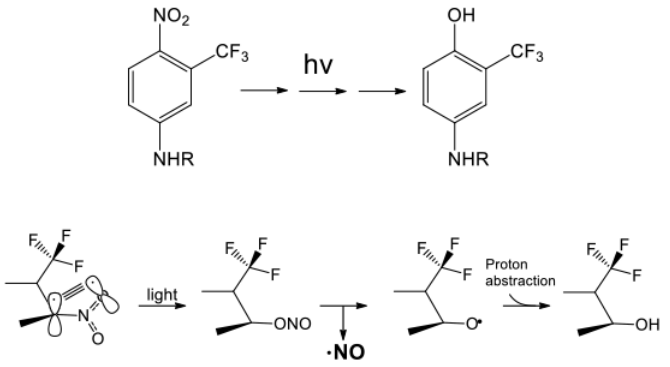

FIGURE 1.5: Mechanism of photorelease of NO from nitroaniline derivates

This molecule presents a particular UV-visible absorption spectrum, having a maximum absorption peak around 400 nm (depending on the nature of R, this value change), allowing us to follow the photobleaching by displaying the decrease of this maximum. It is been proved a linear correlation between the release of NO and the intensity and length of irradiation, which allows to monitor externally its photoproduction.

1.4.3 Photothermal Therapy

Heat was one of the first antibacterial instruments to be exploited by the human body, and remains the cheapest way to disinfect. In chirurgical ambiance, autoclave is a mandatory instrument. Beyond 43°C, tissue necrosis occurs in human body. For this reason hyperthermia therapy has been exploited for cancer treatment. In clinical, they are three mechanisms for heat production in the body:

- Thermal conduction of heat
- Mechanical losses due to molecular collisions from an applied ultrasound (US) pressure wave
- Resistive or dielectric losses from an applied electromagnetic (EM) field[29]

Thermal production can be achieved by high-intensity focused ultrasound (FUS). As a non invasive technique, it seemed one of the most promising therapies alternative to surgery[30]. But in the last years, the most common techniques in thermal therapies to treat cancer in literature are radiofrequency ablation (RFA) and microwave ablation (MWA)[31]. Newer, and so, less studied technologies like High-intensity focused ultrasound (HIFU) which works by the same concept than laser ablation, enjoy ultrasound beams for heat production[32]. New generation of nanomaterials will allow more specific heat generation, decreasing also the target zone: more effectiveness with less secondary effects. As an example, HIFU technique is possible to be combine with nanoparticles to enhance therapy results[33]. But probably the most promising technique among all is photothermal therapy (PTT). Light is an interesting candidate for photoproduction of heat because its fast response, and super spatio-temporary control. Gold nanoparticles (AuNP) and nano-graphene oxide (nGO) presents promising results in PTT for antibacterial[34] and anticancer therapies[35]. Under light excitation, they able to convert it into heat through nonradiative decay pathways, causing irreparable damage to bacteria[36]. One of the main functions of the skin is to protect the body from UV-visible light, which seems to limit the excitation window out of visible: in near infrared region (NIR, 700-900 nm). Thanks to the discovery of two photons excitation system[37], it would be possible to enjoy the photothermal effect of NPs which need to be excited in the visible region.

1.5 Nanomaterials

1.5.1 Metallic Nanoparticles

Silver Nanoparticles

Silver is a material well known as having antimicrobial effect. In the 19th century, using solutions 1% $AgNO_3$ in new-borns reduced dramatically the ocular infections causing blindness. Another application was found in burns, healing the patients from several infections. Silver complexes strongly to electron donor groups containing oxygen, nitrogen and sulphur, presents in microbial cells. With the discovery of penicillin, silver took a second place in medicine. Nowadays, the increasing resistance of bacteria to traditional antibiotics makes

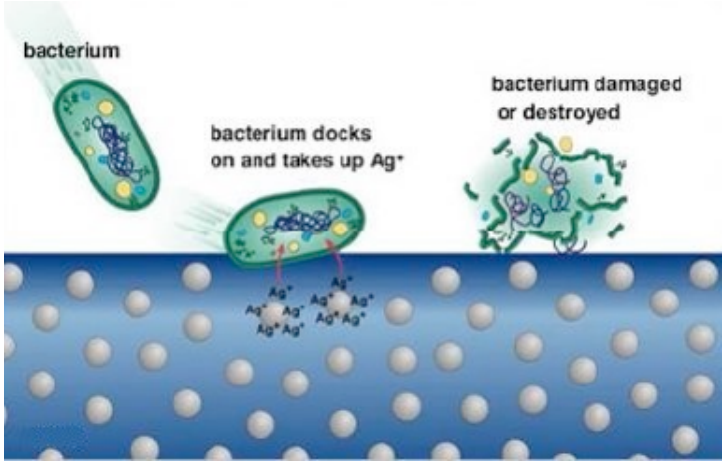

FIGURE 1.6: Hypothetical mechanisms of action of AgNPs

silver attractive again. Silver nanoparticles (AgNPs) are an interesting alternative to traditional antibiotics; due to their small size, they are able to produce the membrane disruption, resulting in the uptake made by the bacteria. Once inside, they suffer different physicochemical processes, such as the release of silver ions, which interact with cell membranes, proteins, electron transport, enzymes, nucleic acids and ATP mechanisms. They are also responsible of the production of reactive oxygen species (ROS), which induces oxidative stress, one of their most important toxicity mechanisms[38]. Antibacterial activity of AgNPs

against E. coli. as a model of Gram-negative bacteria showed accumulation of NP in the membrane, modifying its permeability, and killing it[39].

Gold Nanoparticles

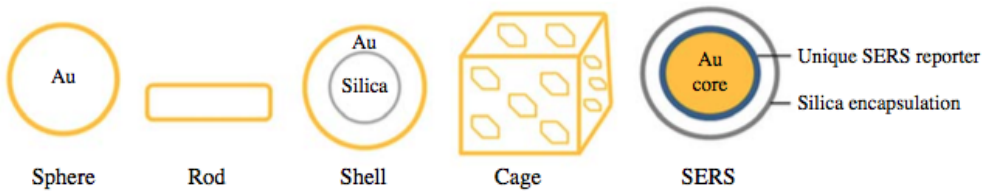

FIGURE 1.7: Some examples of gold nanoparticles

Potential applications of AuNPs in various fields have been studied recently. Their unique optical and physical proprieties make them an interesting candidate for medical applications. As usual in nanoparticles, those proprieties are size and shape dependent. Genomics, biosensors, immunoassays and cancer cell thermolysis are just the most common examples of therapeutic applications, but they can be used also in diagnosis. It is even possible to merge both and enjoy theranostics applications. Its use is based on combining two strategies:

- Properly functionalization at the surface, in a way to maintain their proprieties once in biological environment and to ensure the successful targeting.
- Imaging through excitation of the plasmon band in the vis-NIR. Different techniques can be enjoyed for this aim, like optical tomography[40] , photo acoustic techniques[41] , polarized resonance scattering[42] or two-photon luminescence[43] .

Under light stimulation, electronic excitation is followed by relaxation in short time (sub-picosecond), producing fast increase of the temperature on the surface of the metal[44] and resulting in local heating around AuNPs. Hyperthermia is one of the most effective therapies against cancer and bacteria[45]. Regarding biocompatibility, studies followed by Wyatt

et al showed noncytotoxicity effects in human cells[46] , while other studies say the opposite. Apparently, small sized AuNPs (1,4 nm) produce necrosis of the cells by oxidative stress and mitochondrial damage[47]. The cytotoxicity of AuNPs seems to be size and shape dependent, but it can be decreased by adequate surface modification. Many compatible ligands have been positively tested, and proved non-toxic, but other seemed to have the opposite effect, and increased the cytotoxicity. A frequent example of this fact in literature is the case of CTAB (Cetyl trimethylammonium bromide), commly used for stabilization of the gold nanorods, which is founded to increase the toxicity[48]. AuNPs are considered biocompatible and present less toxicity than other metallic NP, nonetheless, cytoxicity should be always verify .

1.5.2 Graphene oxide

Carbon-based nanomaterials were not considered a suitable choice until 2004, thanks to Andre Geim and Konstantin Novoselov, winners of the Nobel Prize in Physics 2010[49] whom proved graphene being thermodynamically stable under ambient conditions. Their results encouraged scientists to explore this new material.

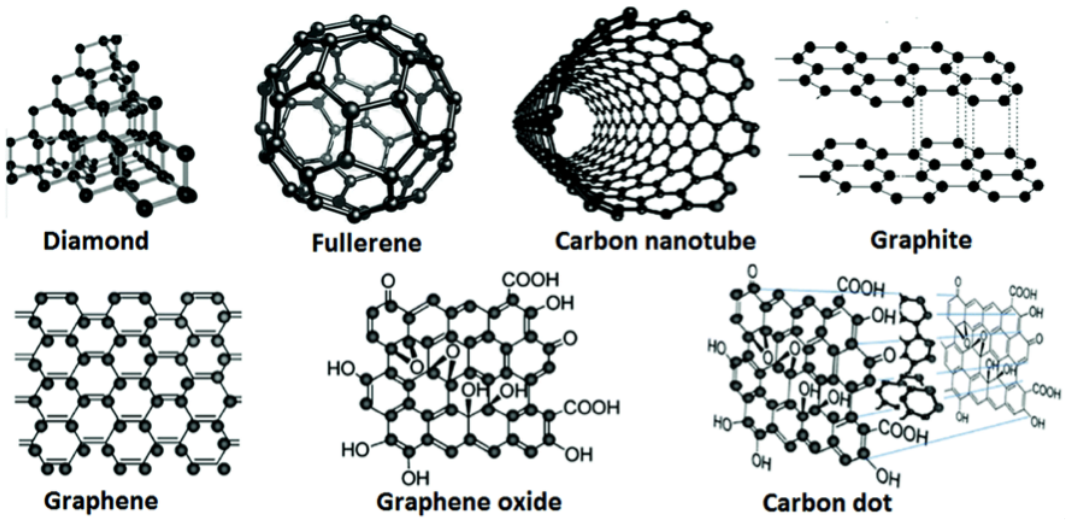

FIGURE 1.8: Some examples of carbon materials

GO is an emerging promising material in several fields: electronics, optics, photovoltaics, but also in nanomedicine. This low cost material[50] exhibits large surface area, which makes it perfect for drug binding, through chemical or even physical interactions. Another propriety that makes it such an interesting material is its high loading capacity, reaching values considerably higher than those observed in different drug delivery systems. As a two-dimensional (2D) nanomaterial, GO has a sheet-like structure, making possible interactions with both side sheets, but also with edges. This gives to GO higher loading capacities ever observed, reaching values superior to 200%wt (235 wt %[51]). This structure gives also to GO flexibility, allowing it to adapt its shape, improving its interaction in biological mediums[52].

As well as graphene is known to be hydrophobic, the presence of epoxy (-O-), hydroxyl (-OH) and carboxylic acid (-COOH) groups[53] provides amphiphilic characteristics to GO. Also, unlike graphite oxide, which has a crystalline structure with more than 10 layers, GO exist in a few layers structure, or even monolayer[52]. Compared to other carbon-based material, another advantage besides the price of production is the lower concentration of toxic metallic impurities due to the fabrication process[54].

1.6 Molecular hybrids based on:

1.6.1 Cyclodextrins

Cyclodextrins are produced by enzymatic conversion from starch or starch derivate thanks to cyclodextrin glycosyl transferase (CGTase). They are cyclic oligosaccharides composed of α-D-glucopyranoside units linked 1->4. Those non-natural macrocycles have from 5 until 32 units of glucosyl residues, but the most common are three:

- α -cyclodextrin (α-CD), 6 units
- β -cyclodextrin(β-CD) 7 units
- γ -cyclodextrin (γ-CD), 8 units

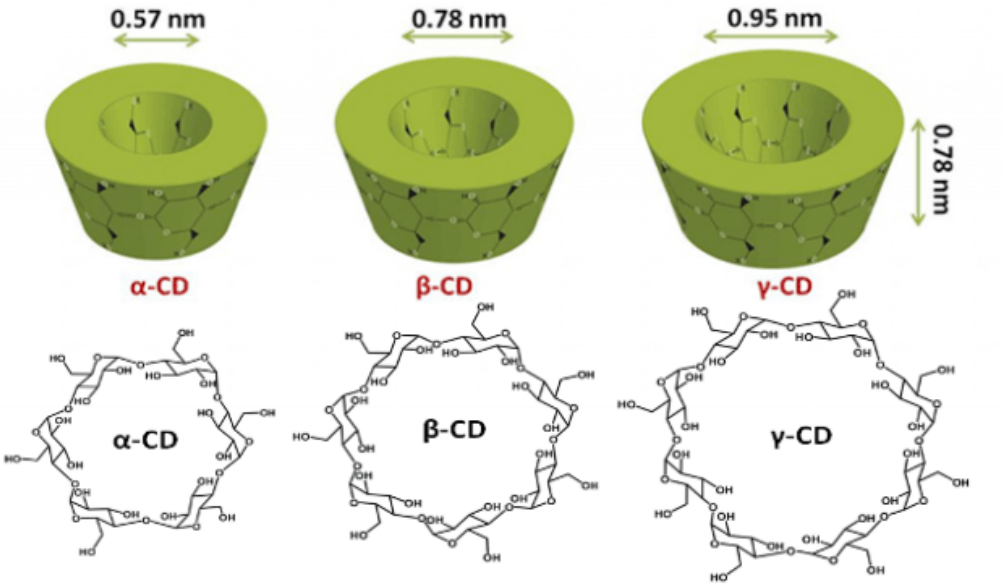

FIGURE 1.9: α-CD, β-CD and γ-CD

Their water solubility differs more than what we could expect; the α-CD and γ-CD have similar values (145 and 232 g·L^{-1}), while β-CD is ten times less soluble than their partners (18,5 g·L^{-1})[55]. But what really makes CD attractive is their cone shape, with a hydrophobic inside and hydrophilic inside, which allows them to interact of even host hydrophobic compounds[56]. Those proprieties make CD interesting candidates for various uses in different fields. They can enhance solubility, bioavailability or stability of other molecules, such as pharmaceutical drugs.

CD and several derivates of them have been FDA approved, and are already in use. The first time that cyclodextrins were putted into the pharmaceutical market was in Japan in 1976. Almost 20 years later, they did the same in European and US market.

1.6.2 Polymers

Another family of materials, which deserve a call of attention, are polymer-based drug delivery systems. Biocompatibility of polymers has been largely studied in several fields, most successful examples are odontology and chirurgical implants. The possibilities offered by

polymers seem to be only limited by scientist's imagination. Small variations in manufacturing process are able to completely alter the proprieties of the final product, for this reason some proprieties will be envisaged, depending on their final application. The most attractive for nanomedicinal use is poly (ethyleneglycol) (PEG), which is known to be non-toxic and non-immunogenic, and has already entered in clinical routine use. When is covalently conjugated to protein drugs, it helps to reduce protein immunogenicity and increases their plasma residence and therapeutic index[57]. Besides the nanometric use of polymers, their applications in larger scales are also promising. Topical and parenteral administration of drugs can be done through water-soluble polymers too. Poly lactic-co-glycolic acid (PLGA) is another example of polymer used for drug delivery and tissue engineering applications. Is biodegradable, biocompatible, FDA approved, and their physical proprieties are tunable, allowing it to control pharmacokinetic freely[58]. The combination of PLGA with PEG leads to the formation of temperature-sensitive materials, with a low Tg (37ºC), over this temperature, they hardens into scaffolds[59]. Another application of biocompatible polymers for drug delivery is the preparation of films, which presents excellent characteristics, such as transparency, easy manufacturing, and high surface loading area[60].

1.7 Multimodal therapy

One century after the discovery of what we call now "traditional antibiotics", the situation requires new smart materials for fighting MDR. The era or broad spectrum antibiotics is ending, and starts the time of target specific and multimodal therapy. Combining different technique to fight DR microorganisms has the goal of maximize their efficacy. Multimodal therapies do not exist only on antibacterial or cancer treatments, the idea of improving the final effect by combining different techniques is being applied in fields like psychology[61] or physiotherapy[62]. A recent study combining the use of doxorubicin combine with the production of NO proved to increase its effect on cancer cells. NO inhibits some efflux pumps, which extrude xenobiotics from the cells. Targeting the immune systems of cancer

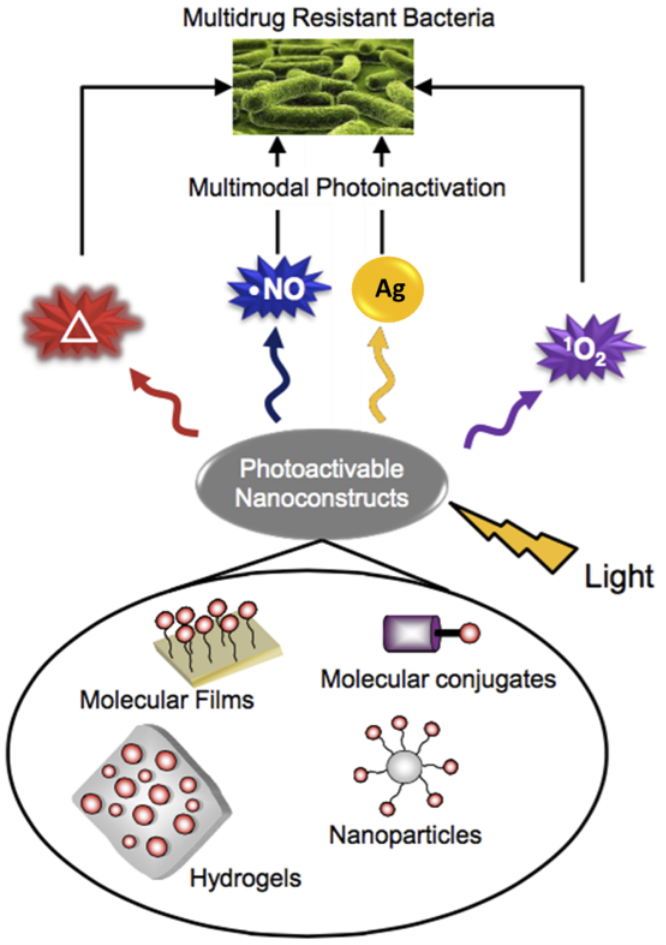

FIGURE 1.10: Examples of photoactivable multimodal systems

cells seemed to increase the effect of several drugs suffering MDR[63]. The combination of PTT with other techniques is presumed to improve the results of the therapy, herein the importance of developing multimodal therapies . Photosensitive systems could be designed to triggered cytotoxic species at different wavelengths, making possible their activation in successive steps[64].Enhancing therapeutic effectiveness to avoid the spread of DR strains by using multimodal therapies could make the difference in the coming days.

Bibliography

[1] Abraham, E. P.; Chain, E. *Nature* **1940**, *146*, 837.

[2] Debono, M.; Barnhart, M.; Carrell, C. B.; Hoffmann, J. A.; Occolowitz, J. L.; Abbott, B. J.; Fukuda, D. S.; Hamill, R. L.; Biemann, K.; Herlihy, W. C. *J Antibiot (Tokyo)* **1987**, *40*, 761–77.

[3] Shute, J. Too much of a good thing. Telegraph.co.uk, http://s.telegraph.co.uk/graphics/projects/antibiotic-resistance/.

[4] Piddock, L. J. *Journal of Antimicrobial Chemotherapy* **2015**, *70*, 2679–2680.

[5] Morgan, D. J.; Okeke, I. N.; Laxminarayan, R.; Perencevich, E. N.; Weisenberg, S. *Lancet Infect Dis* **2011**, *11*, 692–701.

[6] Raviglione, M. C.; Smith, I. M. *New England Journal of Medicine* **2007**, *356*, 656–659.

[7] Udwadia, Z. F.; Amale, R. A.; Ajbani, K. K.; Rodrigues, C. *Clinical Infectious Diseases* **2012**, *54*, 579–581.

[8] Kandoth, N. **2013**,

[9] Munita, J. M.; Arias, C. A. *Virulence Mechanisms of Bacterial Pathogens, Fifth Edition*; American Society of Microbiology, 2016; pp 481–511.

[10] O'Neill, J. *Review on antimicrobial resistance* **2014**, 1–16.

[11] Jonas, O. e. a. Drug-resistant infections : a threat to our economic future (Vol. 2) : final report. Washington, D.C. : World Bank Group, 2017.

[12] Fukuda, H.; Lee, J.; Imanaka, Y. *J Hosp Infect* **2011**, *77*, 93–105.

[13] Allen, T. M.; Cullis, P. R. *Advanced drug delivery reviews* **2013**, *65*, 36–48.

[14] Lancaster, T.; Nalewanski, M.; Zion, T. Polymer-drug conjugates. 2006; US Patent App. 11/583,362.

[15] Sortino, S. *Photochemistry and photobiology* **2006**, *82*, 64–70.

[16] Blanco, E.; Shen, H.; Ferrari, M. *Nature biotechnology* **2015**, *33*, 941–951.

[17] Duncan, R.; Gaspar, R. *Mol Pharm* **2011**, *8*, 2101–41.

[18] Mura, S.; Nicolas, J.; Couvreur, P. *Nature materials* **2013**, *12*, 991.

[19] Ebele, A. J.; Abdallah, M. A.-E.; Harrad, S. *Emerging Contaminants* **2017**,

[20] Jodlbauer, A. *Dtsch Arch Klin Med* **1904**, *80*, 427–487.

[21] Kim, S. Y.; Kwon, O. J.; Park, J.-W. *Biochimie* **2001**, *83*, 437–444.

[22] Wainwright, M.; Crossley, K. B. *International biodeterioration & biodegradation* **2004**, *53*, 119–126.

[23] Koshland, D. *Science* **1992**, *258*, 1861–1861.

[24] Holzer, P. *Pharmacological Reviews* **1991**, *43*, 143–201.

[25] Bell, A.; Brown, D.; Terrett, N. Pyrazolopyrimidinone antianginal agents. 1993; https://www.google.com/patents/US5250534, US Patent 5,250,534.

[26] Karupiah, G.; Xie, Q.-w.; Buller, R. M. L.; Nathan, C.; Duarte, C.; MacMicking, J. D. *Science* **1993**, *261*, 1445–1449.

[27] Liang, H.; Nacharaju, P.; Friedman, A.; Friedman, J. M. **2015**,

[28] Conoci, S.; Petralia, S.; Sortino, S. Use of nitroaniline derivatives for the production of nitric oxide. 2014; US Patent 8,766,006.

[29] Stauffer, P. R. *International Journal of Hyperthermia* **2005**, *21*, 731–744.

[30] Hazle, J. D.; Stafford, R. J.; Price, R. E. *Journal of Magnetic Resonance Imaging* **2002**, *15*, 185–194.

[31] Correa-Gallego, C.; Fong, Y.; Gonen, M.; D'Angelica, M. I.; Allen, P. J.; DeMatteo, R. P.; Jarnagin, W. R.; Kingham, T. P. *Annals of surgical oncology* **2014**, *21*, 4278–4283.

[32] Maloney, E.; Hwang, J. H. *International Journal of Hyperthermia* **2015**, *31*, 302–309.

[33] You, Y.; Wang, Z.; Ran, H.; Zheng, Y.; Wang, D.; Xu, J.; Wang, Z.; Chen, Y.; Li, P. *Nanoscale* **2016**, *8*, 4324–4339.

[34] Norman, R. S.; Stone, J. W.; Gole, A.; Murphy, C. J.; Sabo-Attwood, T. L. *Nano letters* **2008**, *8*, 302–306.

[35] Liu, T.; Wang, C.; Gu, X.; Gong, H.; Cheng, L.; Shi, X.; Feng, L.; Sun, B.; Liu, Z. *Advanced Materials* **2014**, *26*, 3433–3440.

[36] Zou, L.; Wang, H.; He, B.; Zeng, L.; Tan, T.; Cao, H.; He, X.; Zhang, Z.; Guo, S.; Li, Y. *Theranostics* **2016**, *6*, 762.

[37] Göppert-Mayer, M. *Annalen der Physik* **1931**, *401*, 273–294.

[38] Durán, N.; Durán, M.; de Jesus, M. B.; Seabra, A. B.; Fávaro, W. J.; Nakazato, G. *Nanomedicine: Nanotechnology, Biology and Medicine* **2016**, *12*, 789–799.

[39] Sondi, I.; Salopek-Sondi, B. *Journal of colloid and interface science* **2004**, *275*, 177–182.

[40] Gobin, A. M.; Lee, M. H.; Halas, N. J.; James, W. D.; Drezek, R. A.; West, J. L. *Nano letters* **2007**, *7*, 1929–1934.

[41] Kim, J.-W.; Galanzha, E. I.; Shashkov, E. V.; Moon, H.-M.; Zharov, V. P. *Nature nanotechnology* **2009**, *4*, 688–694.

[42] Aaron, J.; de La Rosa, E.; Travis, K.; Harrison, N.; Burt, J.; José-Yacamán, M.; Sokolov, K. *Optics express* **2008**, *16*, 2153–2167.

[43] others,, et al. *Optics Express* **2008**, *16*, 1590–1599.

[44] Ray, P. C.; Khan, S. A.; Singh, A. K.; Senapati, D.; Fan, Z. *Chemical Society Reviews* **2012**, *41*, 3193–3209.

[45] Zharov, V. P.; Mercer, K. E.; Galitovskaya, E. N.; Smeltzer, M. S. *Biophysical journal* **2006**, *90*, 619–627.

[46] Connor, E. E.; Mwamuka, J.; Gole, A.; Murphy, C. J.; Wyatt, M. D. *Small* **2005**, *1*, 325–327.

[47] Pan, Y.; Leifert, A.; Ruau, D.; Neuss, S.; Bornemann, J.; Schmid, G.; Brandau, W.; Simon, U.; Jahnen-Dechent, W. *Small* **2009**, *5*, 2067–2076.

[48] Bozich, J. S.; Lohse, S. E.; Torelli, M. D.; Murphy, C. J.; Hamers, R. J.; Klaper, R. D. *Environmental Science: Nano* **2014**, *1*, 260–270.

[49] Novoselov, K. S.; Geim, A. K.; Morozov, S. V.; Jiang, D.; Zhang, Y.; Dubonos, S. V.; Grigorieva, I. V.; Firsov, A. A. *science* **2004**, *306*, 666–669.

[50] Liu, Z.; Robinson, J. T.; Sun, X.; Dai, H. *Journal of the American Chemical Society* **2008**, *130*, 10876–10877.

[51] Yang, X.; Zhang, X.; Liu, Z.; Ma, Y.; Huang, Y.; Chen, Y. *The Journal of Physical Chemistry C* **2008**, *112*, 17554–17558.

[52] Mu, Q.; Su, G.; Li, L.; Gilbertson, B. O.; Yu, L. H.; Zhang, Q.; Sun, Y.-P.; Yan, B. *ACS applied materials & interfaces* **2012**, *4*, 2259–2266.

[53] Dreyer, D. R.; Park, S.; Bielawski, C. W.; Ruoff, R. S. *Chemical Society Reviews* **2010**, *39*, 228–240.

[54] Bussy, C.; Ali-Boucetta, H.; Kostarelos, K. *Accounts of chemical research* **2012**, *46*, 692–701.

[55] Loftsson, T.; Duchene, D. *International journal of pharmaceutics* **2007**, *329*, 1–11.

[56] Davis, M. E.; Brewster, M. E. *Nature reviews. Drug discovery* **2004**, *3*, 1023.

[57] Duncan, R. *Nature reviews. Cancer* **2006**, *6*, 688.

[58] Makadia, H. K.; Siegel, S. J. *Polymers* **2011**, *3*, 1377–1397.

[59] Dhillon, A.; Schneider, P.; Kuhn, G.; Reinwald, Y.; White, L. J.; Levchuk, A.; Rose, F. R. A. J.; Müller, R.; Shakesheff, K. M.; Rahman, C. V. *J Mater Sci Mater Med* **2011**, *22*, 2599–605.

[60] Lewis, A. L.; Tang, Y.; Fajardo, M. V. G. Loading of hydrophobic drugs into hydrophilic polymer delivery systems. 2011; US Patent 8,007,831.

[61] Norcross, J. C.; Goldfried, M. R. *Handbook of psychotherapy integration*; Oxford University Press, 2005.

[62] Brantingham, J. W.; Cassa, T. K.; Bonnefin, D.; Pribicevic, M.; Robb, A.; Pollard, H.; Tong, V.; Korporaal, C. *Journal of manipulative and physiological therapeutics* **2013**, *36*, 143–201.

[63] others,, et al. *ACS Medicinal Chemistry Letters* **2017**, *8*, 361–365.

[64] Fraix, A.; Kandoth, N.; Manet, I.; Cardile, V.; Graziano, A. C.; Gref, R.; Sortino, S. *Chemical Communications* **2013**, *49*, 4459–4461.

Part I

Nano Materials

Chapter 2

Metallic nanoparticles-based materials

2.1 Introduction

Silver nanoparticles are well known for their bactericidal activity, as well as gold nanoparticles present photothermal activity. This chapter looks for the combination of those two metal in a way to produce a bimodal systems with intrinsically antibacterial activity and PTT. For this aim, preparation of water-soluble AgNPs, AuNPs and core-shell gold-silver nanoparticles (Au@Ag CS-NPs) will be done by using light and a dextran (DXT) functionalized with a benzophenone (BP) chromofore. This molecule can be excited with UVA light (Figure 2.1) and, after intersystem crossing (ISC) is expected to abstract a hydrogen from the DXT producing a highly reducing ketyl radical (Figure 2.1). Its reducing character is big enough to reduce metallic ions such as silver or even, gold, into metallic NPs and, in part, to revert back to the initial compounds after proton elimination.

The main idea is to use this DXT-BP not only to produce a reducing agent, but also to stabilize the metal NPs once formed.

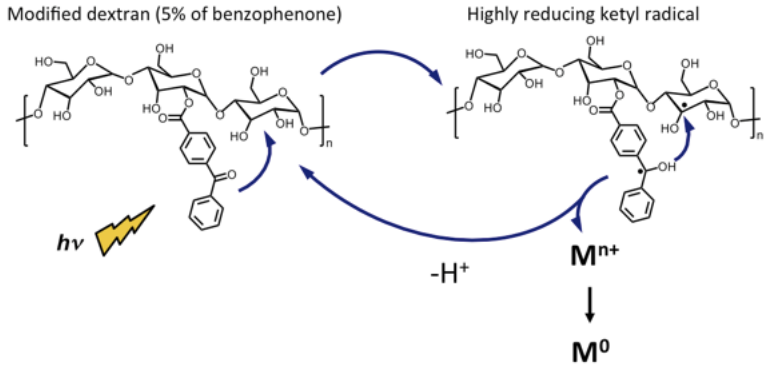

FIGURE 2.1: Mechanism of the formation of the high reducing ketyl radical in DXT

2.2 Experimental

2.2.1 Methods

All the solutions were prepared with MilliQ water, and the reactives were supplied by Sigma-Aldrich. The quartz cells were clean before every experiment with aqua regia. A stock solution of 2,5% dextran was prepared by dissolving it in MilliQ water. The unknown concentration of BP was obtained measuring the UV-visible absorption, then using the Beer-Lamber law (A= $\epsilon \cdot l \cdot c$) it was calculated: at 261 nm, A=1,942 and λ=17 000 $M^{-1} \cdot cm^{-1}$, so $[BP]_0$=1,14$\cdot 10^{-2}$M.

Due to the high hygroscopic behaviour of chloroauric acid (III), the stock solutions concentration in Au^{3+} was calculate by Beer-Lambert's law. The water-saturated solution of pyrene was prepared adding an excess of the compound, stir with a magnet for 1h, then sonicate it for 30 min and finally filtrate the resulting solution with a syringe coupled with a filter Ø=0,45 μm porous.

2.3 Instrumentation

Absorption spectra were recorded with a Jasco V 560 spectrophotometer. Nanoparticle sizes were measured by a dynamic light scattering performed with a Horiba LS 550 apparatus equipped with a diode laser with a wavelength of 650 nm. TEM measurements were performed at the ST microelectronics.

2.3.1 Photochemical experiments

Steady state and pulsed laser irradiation was performed in a thermostated quartz cell (1 cm pathlength, 3 mL capacity) by using a Rayonet photochemical reactor equipped with 5-10 RPR lamps with an emission in the 320-380 nm range with a maximum at 350 nm.

2.3.2 Laser flash photolysis

All solutions were excited with the second harmonic of Nd-YAG Continuum Surelite II-10 (532 nm, 6 ns FWHM), using quartz cells with path length 1,0 cm. The excited solutions were analysed with a Luzchem Research mLFP-111 apparatus with an orthogonal pump/probe configuration. The probe source was a ceramic xenon lamp coupled to quartz fibre-optic cables. The laser pulse and the mLFP-111 system ere synchronized by a Tektronix TDS 3032 digitized, operating in pre-trigger mode. The signals form a compact Hamamatsu photomultiplier were initially captured by the digitizer and then transferred to a personal computer, controlled by Luzchem Research software operating in the National Instruments LabView 5.1 environment. The solutions were deoxygenated by bubbling with a vigorous and constant flux of pure nitrogen (previously saturated with solvent). The solution temperature was 295 $\pm$ 2K. The energy of the laser pulse was measured at each slot with a SPHD25 Scientech pyroelectric meter.

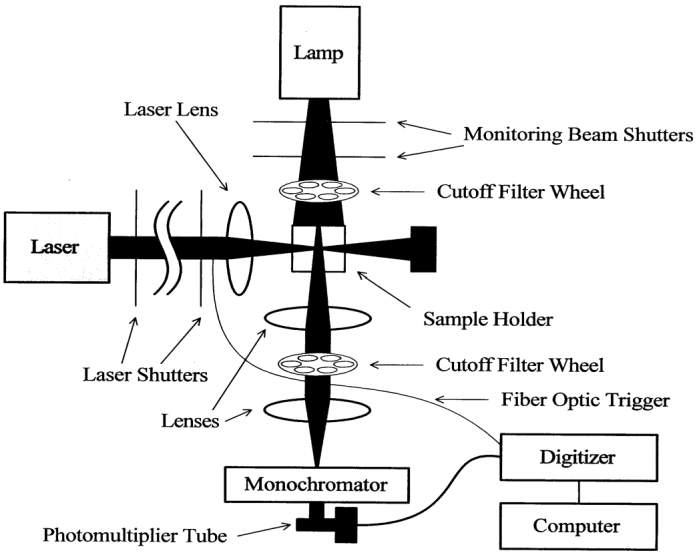

FIGURE 2.2: Laser flash photolysis setup

2.3.3 Photothermal experiments

Photothermal measurements were display in a plastic cell, irradiating with laser and following the temperature increasing assisted with a mercuric thermometer, under magnetic stirring. Irradiation was in a plastic cell (1 cm path length, 3 mL capacity) by 200 mW continuum lasers with λ_{exc} = 532 nm.

2.3.4 Antibacterial tests

MIC for silver particles

The antibacterial action of AgNPs and AgDXT nanoparticles was determined using the dilution method. The 8325-4 S. aureus strain was grown on COS agar plate for 24h at 37ºC. The bacterial load was standardized as followed; a 0,5 McFarland (1.5 x 107 CFU/mL) bacterial suspension (BS) is prepared with fresh colonies and diluted in Mueller Hinton (MH) (SIGMA) to a final concentration of 1,5 x 105 CFU/mL. AgNPs and AgDXT particles at an initial concentration of 200 μg/mL were serially diluted 2-times in MH medium in a 96-well

plate (Falcon, round bottom) from column 1 to 12. Bacteria were added at a final concentration of 0.75 x 105 CFU/mL to each well, resulting in a final particles concentration of 50 μg/mL in column 1. MH and particles in MH were used as positive controls and MH with BS only as negative controls. The plate was incubated for 24h at 37°C in a moist chamber. This experiment was carried out 3 times for each type of particles.

Time-Dose-Effect curves for silver particles

S. aureus at an initial concentration of 106 and 108 CFU·mL^{-1} were exposed to decreasing concentrations (from 50 to 0 μg·mL^{-1} , 2-fold serial dilution) of the AgNPs and AgDXT nanoparticles in Luria-Bertani (LB) medium. The cultures were incubated at 36°C - 180 rpm and bacterial concentrations determined every 2h for 16h by measuring the OD600nm (Tecan, Infinite-200 pro). The minimum bactericidal concentration (MBC) was determined by assessing the total growth inhibition on TSA agar after 24h at 36°C. This experiment was carried out once for each type of particles.

2.4 Results and Discussion

2.4.1 Dextran-benzophenone characterisation

The DXT-BP was provided by the group of Dr. Gref from Paris Sud Université. The concentration of BP in DXT was determinate spectrophotometrically (ϵ=17000M^{-1}·cm^{-1} at λ=261nm).

As explain above, this BP can be excited with 350 nm light, producing a high reducing ketyl radical (Figure 2.1). In order to characterize this key intermediate, we performed laser flash photolysis experiment. Figure 2.3 shows transient spectrum of the ketyl radical with the typical absorption bands at 350 and 560 nm. We were not able to characterize the excited triplet state, the first intermediate of the radical formation process, in according to its very short lifetime (<20 ns) due to the fast hydrogen abstraction. DXT has amphiphillic proprieties; its behaviour depends on the concentration. When the concentration is higher

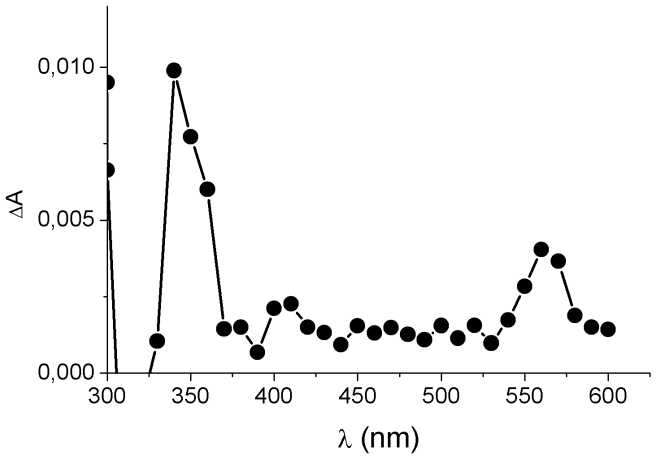

FIGURE 2.3: Transient spectrum obtained after 355 nm laser excitation of a N_2-saturated solution of DXT-BP and recorded 100 ns after the laser pulse.

than the Critical Micelle Concentration (CMC), the molecules mostly arrange themselves in micellar form (Figure 2.4).

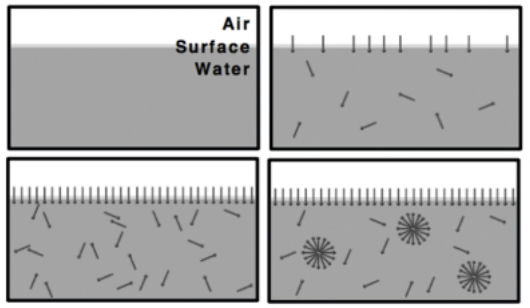

FIGURE 2.4: Arrangement concerning the concentration of an amphiphilic compound.

To determine the CMC of the DXT-BP, we used pyrene as a suitable fluorophore. When pyrene is excited with appropriate wavelength its fluorescence excitation spectra display five characteristic peaks (Figure 2.5).

It has been proven that a relation between the I_1/I_3 rates and different concentrations of

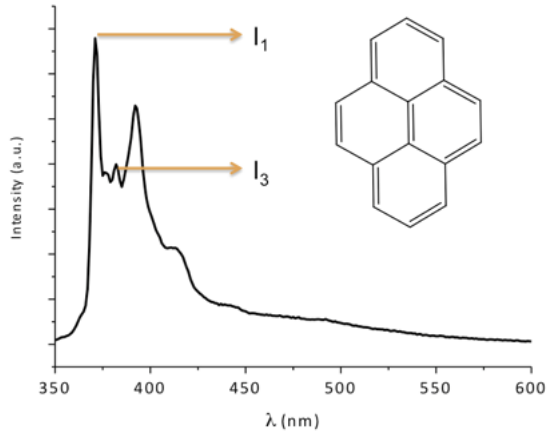

FIGURE 2.5: Emission spectra of pyrene λexc= 373 nm.

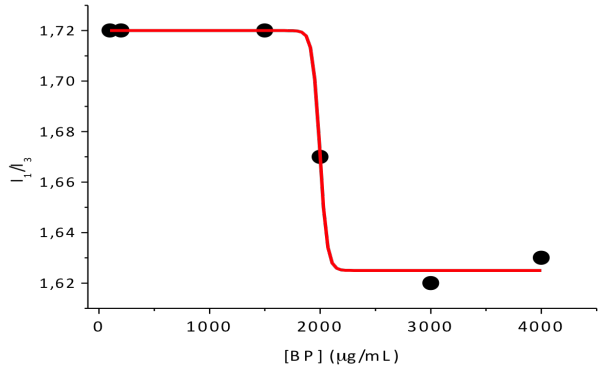

FIGURE 2.6: I_1/I_3 ratio as a function of Dxt concentration. CMC= 2000 μg·mL^{-1}.

the intended amphiphilic compound are correlated[1]. By plotting the I_1/I_3 rates feat [DXT-BP], a sigmoidal graphic was obtained, and the CMC estimated around 2000 μg·mL^{-1}.

2.4.2 Synthesis of NPs

Silver NPs

For the synthesis of AgNPs, to a DXT-BP solution [BP]= 1 mM was added silver nitrate solution as source of metallic ions at [Ag^+]= 0,3 mM. Before irradiation, it is need to remove all the gases from the solution, to avoid parallels reactions with oxygen present in water.

The AgNPs are formed in a few minutes and show the typical plasmon band around 400-410 nm. This maximum is directly related with the dimension of the NPs[2]: small NPs present the maximum at lower wavelength and bigger NPs the opposite. The experiment was performed in a quartz cell, to be able to follow in real time the formation of the AgNPs.

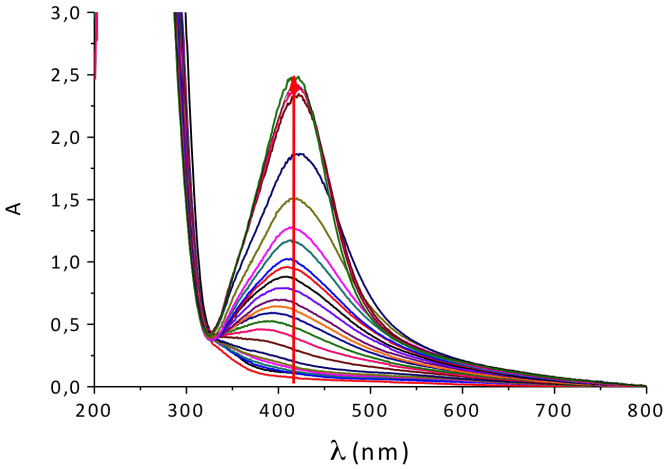

FIGURE 2.7: Absorption spectra following the formation of AgNPs. Conditions: [BP]= 1 mM, [$AgNO_3$]= 0,3 mM; measured at intervals of 1-5 min.

Many tests were made with three different wavelengths excitation sources. The reaction was assisted by a photochemical reactor (circular shape), equipped with 10 lamps with a maximum emission centered at 254 nm, 300 nm and 350 nm, under magnetic stirring. The best results were obtained with 350 nm lamps. After almost one hour of irradiation, all the AgNPs were formed (Figure 2.7)

To prove the efficiency of DXT as a capping compound too, the stability of the sample was followed over time. As is visible in Figure 2.8, they are not significant changes in the absorption spectrum, just the regular stabilization of NPs .

The size of NPs, determinate by Transition Electronic Microscopy (TEM) is about 6 nm. The pictures displayed show NPs have round shape.

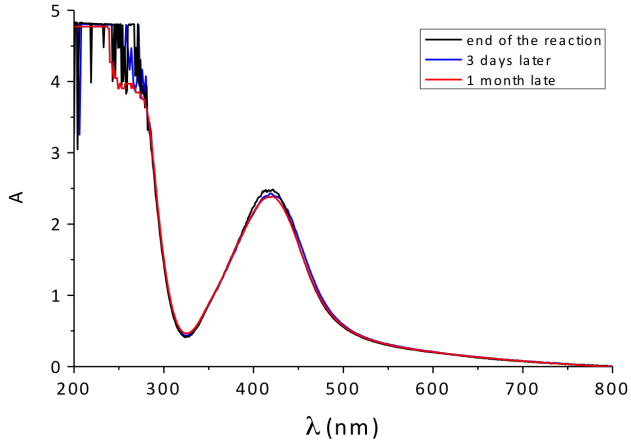

FIGURE 2.8: Absorption spectra observed at different delay time after the formation of the AgNPs.

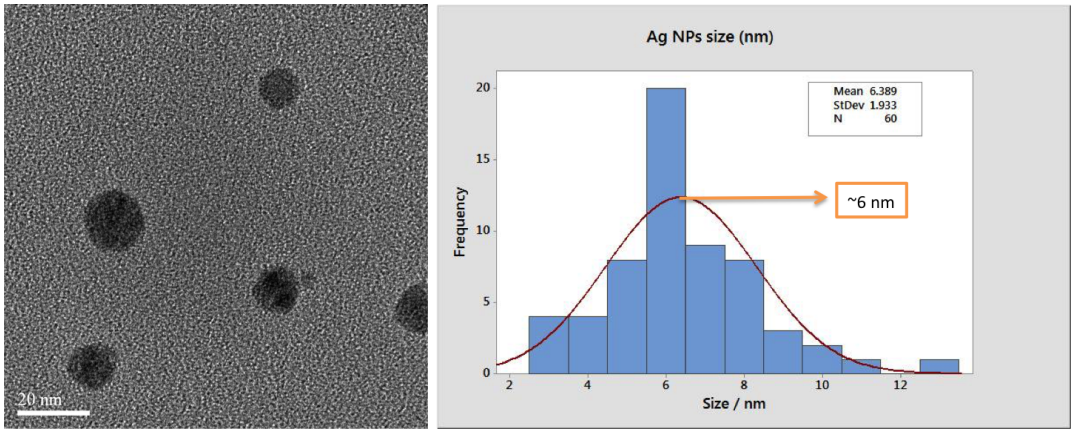

FIGURE 2.9: Representative TEM image (left) and size distribution (right) of the AgNPs.

The same experiments were repeated using a different silver salt: Acetilacetonate of Silver (AcacAg). The interesting point respecting this compound is their instability in aqueous solution, producing spontaneous AgNPs. It could be possible to enjoy this double reducing effect, in a way to get bigger rates. In fact, comparing the results obtained in the same conditions, but with $Acac^-$ as a contra ion, an improvement was observed. The maximum absorption was almost the double in the half time of irradiation.

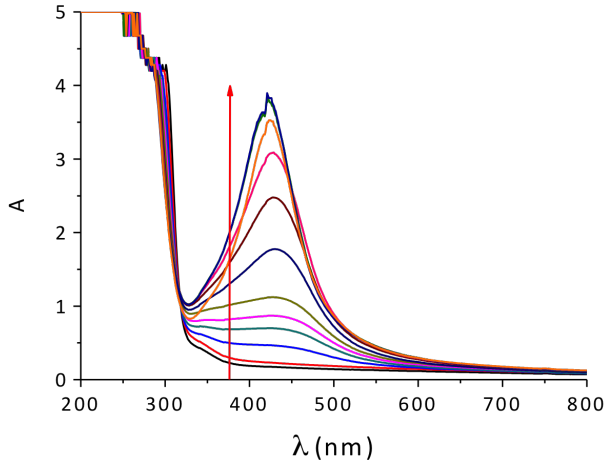

FIGURE 2.10: Absorption spectra following the formation of AgNPs ([BP]= 1 mM, [AgAcac]= 0,3 mM; at intervals of 1 and then 5 min of irradiation).

Core-Shell AuAg NPs

If gold (III) and silver (I) ions are reduced together, the first ones will be reduced first because his potential of reduction is bigger than silver's one: $\epsilon_0(Au/Au^{3+})$= 1.498 V and $\epsilon_0(Ag/Ag^{+})$= 0.799 V. Following the precedents methodologies, core shell NPs were first obtained using silver nitrate (Figure 2.11). The sample was irradiated a little bit more than one hour with 10 lamps at λ= 350nm. As shown in Figure 2.11, we observed the formation of the plasmon band gold absorption first allowed by the formation of the silver plasmon absorption band. The ration of the bands reflects the ration of the concentration of the ions used in the experiments.

The treatment of the NPs with nitric acid leads to the dissolving of the shell as demonstrated by the appearance of the plasmon band related only to gold reappear (Figure 2.12).

Respecting the size, the CS-NP got almost the same size than the AgNPs (Figure 2.14). The results gave by the Electron Difraction Ray-X (EDX) confirmed the Au:Ag proportion is 1:4 (Figure 2.14, left), the same before the photochemical reduction (Figure 2.12).

The complete process was repeat with AgAcac as source of silver ions, having the same

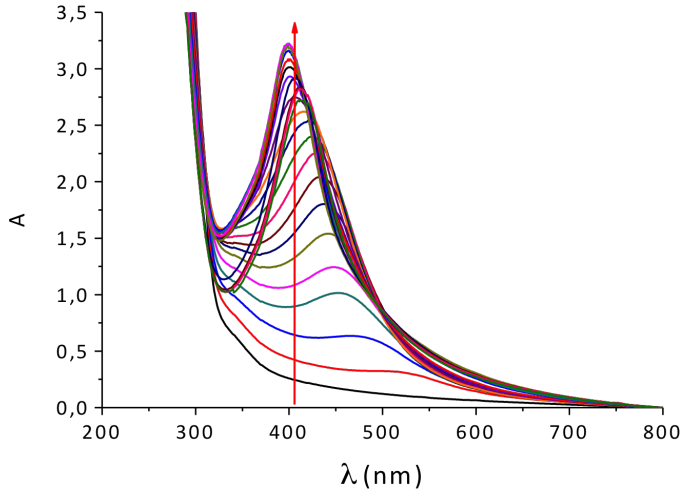

FIGURE 2.11: Absorption spectra following the formation of Au@Ag CS-NPs. Conditions: [BP]= 1 mM, [Au^{3+}]= 0,1 mM, [AgAcac]= 0,3 mM; intervals of 5 min irradiated with 10 lamps 350 nm.

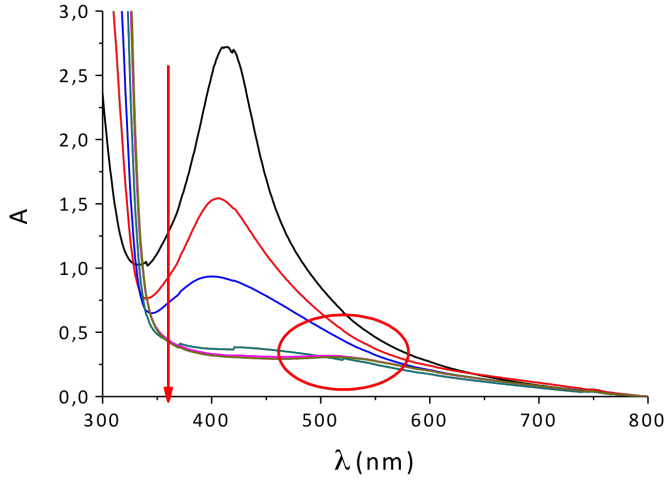

FIGURE 2.12: Degradation of Au@Ag CS-NPs with additions of HNO_3.

concentration of Au^{3+}. We observed that 15 minutes after the addition of AcacAg, the solution presented a purple-violet, characteristic of AuNP, which changed in an orange yellow upon irradiation due to the formation of the silver shell (Figure 2.13).

The size of those CS-NP measured by TEM was 16,8 nm with a core around 10 nm, a little

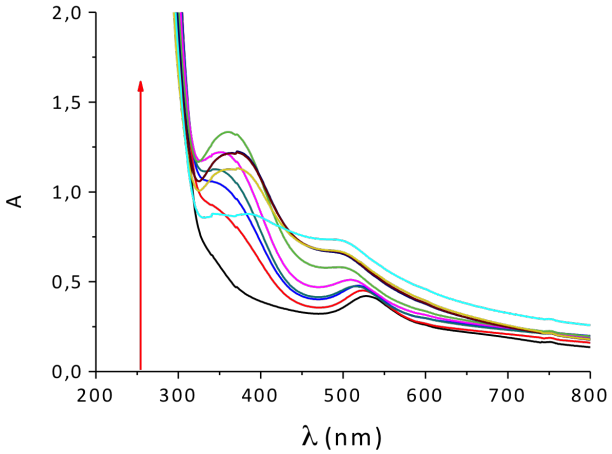

FIGURE 2.13: Absorption spectra following the formation of Au@Ag CS-NPs. Conditions: [BP]= 1 mM, [Au^{3+}]= 0,3 mM, [AgAcac]= 0,3 mM; intervals of 5 min irradiation with 10 lamps at 350 nm.

bigger than the others. In addition, the proportion of between Ag and Au was a different than the expect (Figure 2.14 left). In the other hand, the pictures made show a perfect CS-NP (Figure 2.14 right).

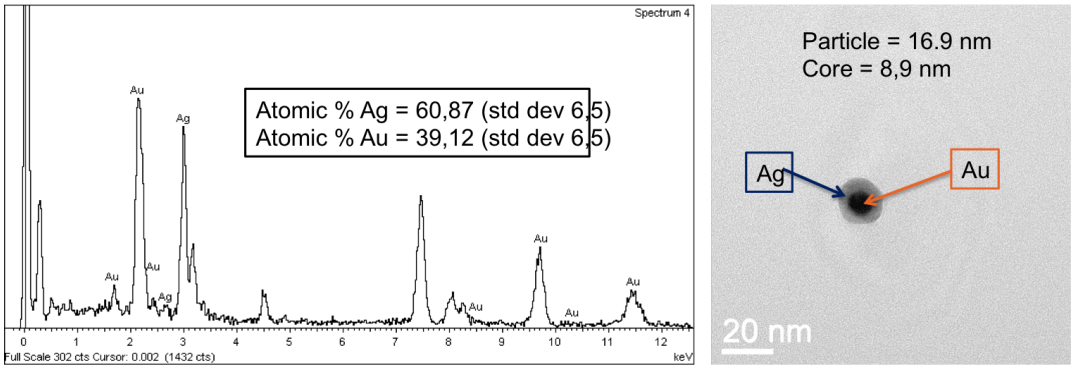

FIGURE 2.14: EDX spectra of Au@Ag CS-NPs (left); TEM picture of Au@Ag CS-NPs (right).

The stability of the nanoparticles was increased by adding citrate as stabilizer. Figure 2.15 shows that after formation of the core-shell NPs, they remains stable for long time.

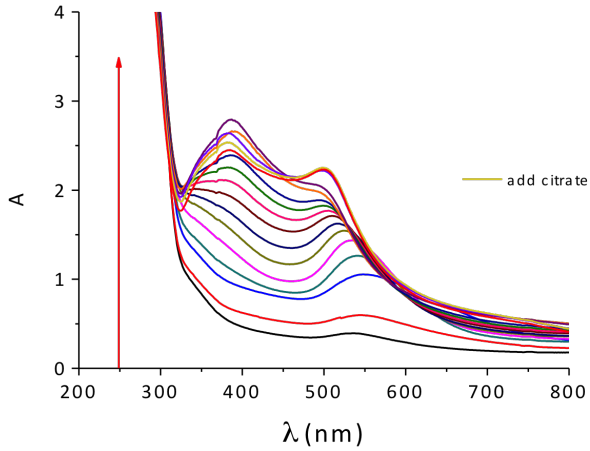

FIGURE 2.15: Absorption spectra following the formation of Au@Ag CS-NPs. Conditions: [BP]= 1 mM, [Au^{3+}]= 0,3 mM, [AgAcac]= 0,3 mM; irradiate with 5 lamps at 350 nm at 5 min intervals, with posterior addition of [$citr^{-}$]= 1 mM.

2.4.3 Photothermal effect

As earlier explained, AuNPs are suited nanoconstructs to convert visible light into heat, leading to interesting photothermal effects. To this goal, the samples were irradiated with a 532 nm CW laser. The results are shown in Figure 2.15 where it can be noted a relevant temperature increase upon light irradiation.

The photothermal effect of AuNPs was evidenced as shown in Figure 2.16. Similar results were observed when the two kinds of Au@Ag CS-NPs were irradiated in the same conditions (Figure 2.17).

2.4.4 Antibacterial results

The antibacterial action of silver nanoparticles was proved against 8325-4 *S. aureus strain* . Two different precursors of AgNs will be compared: with DXT-BP (AgDxt) and with AcacAg (AgNPs)-

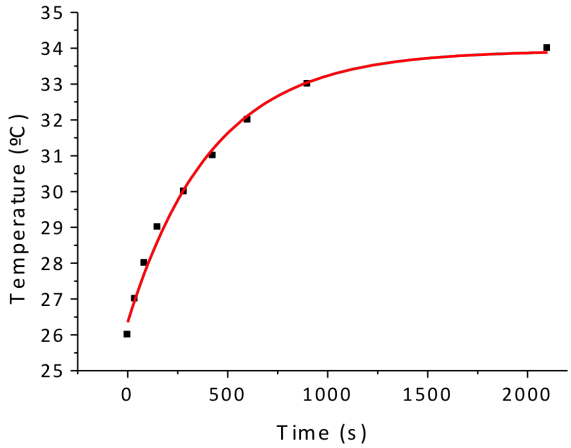

FIGURE 2.16: Temporal evolution of temperature upon 532 nm LASER irradiation of AuNPs.

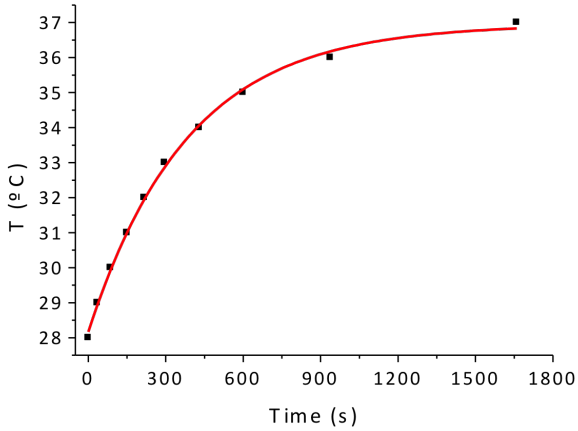

FIGURE 2.17: Temporal evolution of temperature upon 532 nm LASER irradiation of Au@Ag CS-NPs synthetized with silver acetylacetonate.

MIC for silver nanoparticles

After 24h the medium turbidity in the wells was visually assessed. The Minimum Inhibitory Concentration (MIC) of the particles was defined as the concentration corresponding to the first well without visible bacterial growth, i.e. with no development of turbidity. The MICs were 25 μg·mL^{-1} for AgNPs particles and 50 μg·mL^{-1} for AgDXT particles.

Time-Dose-Effect curves for silver particles

The effect of increasing concentrations of AgNPs (0.10 to 50 $\mu g \cdot mL^{-1}$) on the growth of S. aureus at 106 CFU·mL^{-1} and 108 CFU·mL^{-1} are shown in Figure 2.18. For 106 CFU·mL^{-1}, an inhibition is observed when the AgNPs concentration reaches 0.78 $\mu g \cdot mL^{-1}$ while for 108 CFU·mL^{-1} the inhibition is observed from 3.13 $\mu g \cdot mL^{-1}$.

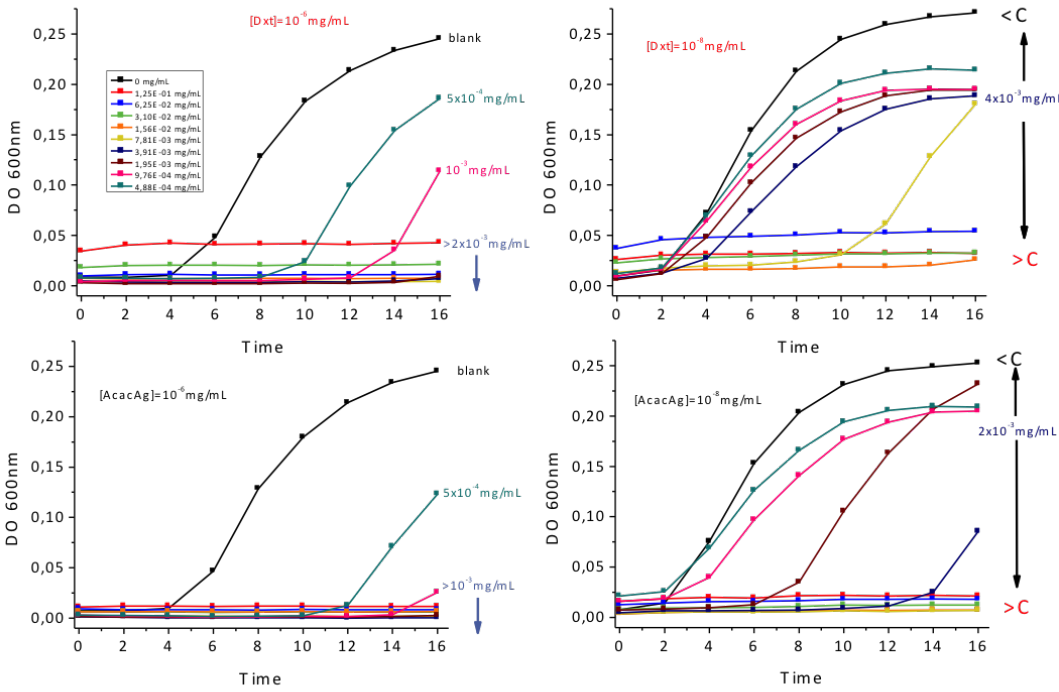

FIGURE 2.18: Antibacterial activity.

The results obtained for AgDXT (0.10 to 50 $\mu g \cdot mL^{-1}$) are presented in Figure 2.18. The bacterial growth inhibition is observed for concentrations from 0.78 $\mu g \cdot mL^{-1}$ and 6.25 $\mu g \cdot mL^{-1}$ for 106 CFU·mL^{-1} and 108 CFU·mL^{-1} respectively. Further increase in AgDXT concentration led to a complete inhibition of the bacterial growth.

AgNPs and AgDXT are both effective at a concentration of 0.78 $\mu g/mL$ to inhibit the

growth of 106 CFU·mL^{-1} of bacteria. However a higher concentration of AgDXT than AgNP is required to inhibit the growth of 108 CFU·mL^{-1} *S. aureus*, indicating a better antibacterial activity of AgNPs. Finally, the MBC's against *S. aureus* are 3.13 μg·mL^{-1} for AgNPs VS. 12.50 μg·mL^{-1} for AgDXT. Bacterial growth inhibition trends observed from CFU data are consistent with OD600 measurement.

2.5 Conclusions

Stable AgNPs, AuNPs were synthetized with a simple compound that acts as source of reduction and stabilizing as the same time. After several experiments, the conditions of photochemical reduction of metallic ions were optimized. Concerning the stability, AgNPs and AuNPs seem being stable for long periods. Instead, the stability of Au@Ag CS-NPs was improved by the Dxt-BP, but stills questionable. The addition of an extra capping compound was needed to increase it over time. Photothermal activity of AuNPs and Au@Ag CS-NPs was demonstrated in laboratory conditions. Additionally AgNPs and AgDXT showed a strong antibacterial property against S. aureus, with AgNPs being more effective than AgDXT when the inhibitory and antibacterial activities are assessed. Further studies to prove the efficacy of PTT as antibacterial agent will be carried out.

Bibliography

[1] Kalyanasundaram, K.; Thomas, J. K. *The Journal of Physical Chemistry* **1977**, *81*, 2176–2180.

[2] Link, S.; El-Sayed, M. A. *The Journal of Physical Chemistry B* **1999**, *103*, 4212–4217.

Chapter 3

Graphene oxide

Graphene oxide nanohybrid that photoreleases nitric oxide

Published as:

Authors: Nino Marino, Salvatore Petralia, Marta Perez-Lloret, Jiri Mosinger, Sabrina Conoci and Salvatore Sortino

Journal: Journal of Materials Chemistry B, 2016, vol. 4, no 35, p. 5825-5830.

Volume 4 | Number 35 | 21 September 2016 | Pages 5763–5948

Journal of Materials Chemistry B

Materials for biology and medicine

www.rsc.org/MaterialsB

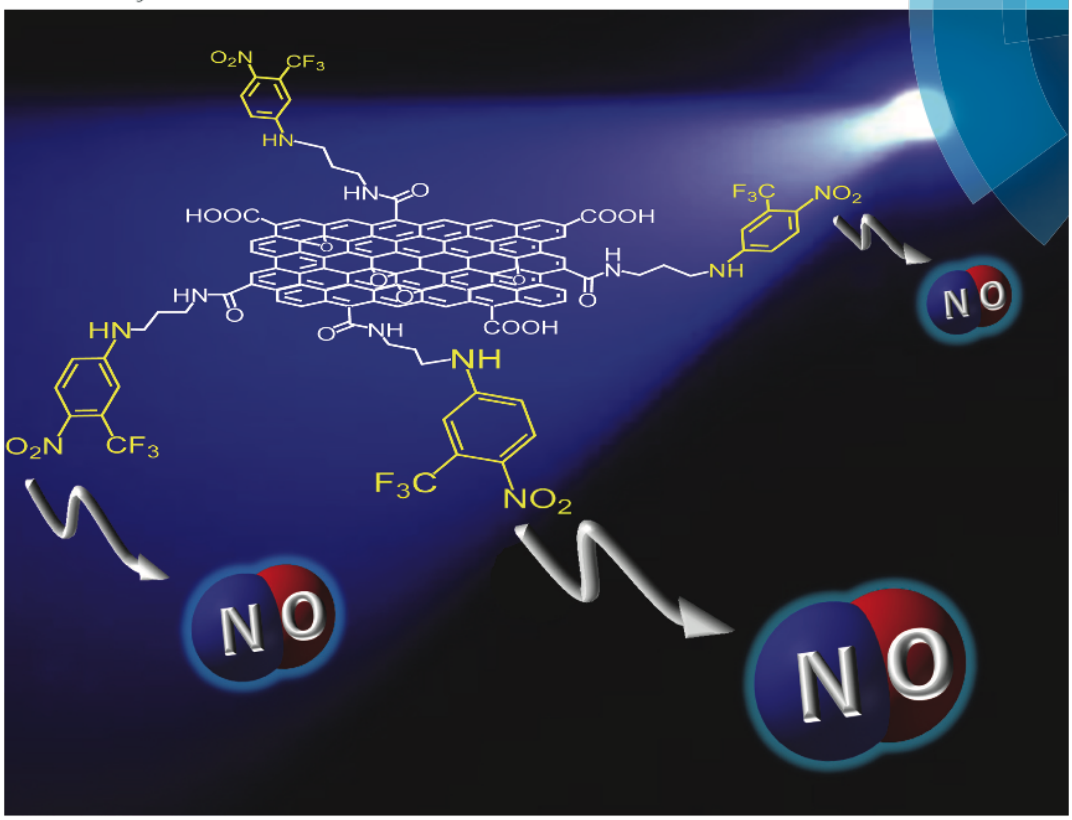

ISSN 2050-750X

ROYAL SOCIETY OF CHEMISTRY

PAPER
Sabrina Conoci, Salvatore Sortino *et al.*
Graphene oxide nanohybrid that photoreleases nitric oxide

175 YEARS

3.1 Introduction

Graphene oxide (GO) is a low cost material that is synthesized from graphite and has a wide range of potential uses in many research areas, including energy storage[1], nanoelectronics[2], molecular biosensing[3] and catalysis[4]. In recent years, GO has also generated much interest in the field of biomedicine, especially as a novel nanomaterial with promising applications in drug delivery[5,6]. GO nano-therapeutic platforms can carry bioactive compounds ranging from small drug molecules to high molecular weight bioactive compounds such as antibodies, polynucleotides and proteins; this has been recently reviewed[5,6,7]. Due to its sheet-like structure, GO has a very large surface area. The two external surfaces are ideal for drug loading through chemical conjugation or physical interaction, reaching values close to 200%, considerably higher than those observed for nanoparticles or other drug delivery systems[8]. Nitric oxide (NO) is an ephemeral inorganic free radical which plays a key role in the bioregulation of many vital functions, including neurotransmission, hormone secretion and vasodilatation[9]. NO is involved in a number of additional important biological processes, including platelet aggregation and adhesion[10], immune response to infections[11], reduction of radical-mediated oxidative pathways[12], wound repair[13], and cancer biology[14,15]. These intriguing features have stimulated tremendous interest in compounds that can store and release NO[16,17], as well as their integration in macromolecular scaffolds[18] and nanomaterials[19], with the final goal of targeting important diseases. In this regard, a key point to be taken into account is that the therapeutic outcome of any NO-releasing system is strictly dictated by three main parameters: (i) concentration, (ii) delivery site and (iii) dosage. Because of these pre-requisites, NO-releasing compounds triggered by light stimuli are very appealing[20,21,22,23,24,25,26]. In view of its easy manipulation in terms of intensity, wavelength, duration and localization, light represents a highly orthogonal, minimally invasive, and finely tunable tool to achieve controlled NO delivery with superb spatiotemporal accuracy. Additionally, the fast reaction rates of photochemical reactions ensure rapid NO release without affecting physiological conditions[20,21,22,23,24,25,26]. Therefore, photocontrolled NO-based therapies are emerging as new "unconventional" treatment modalities[27]

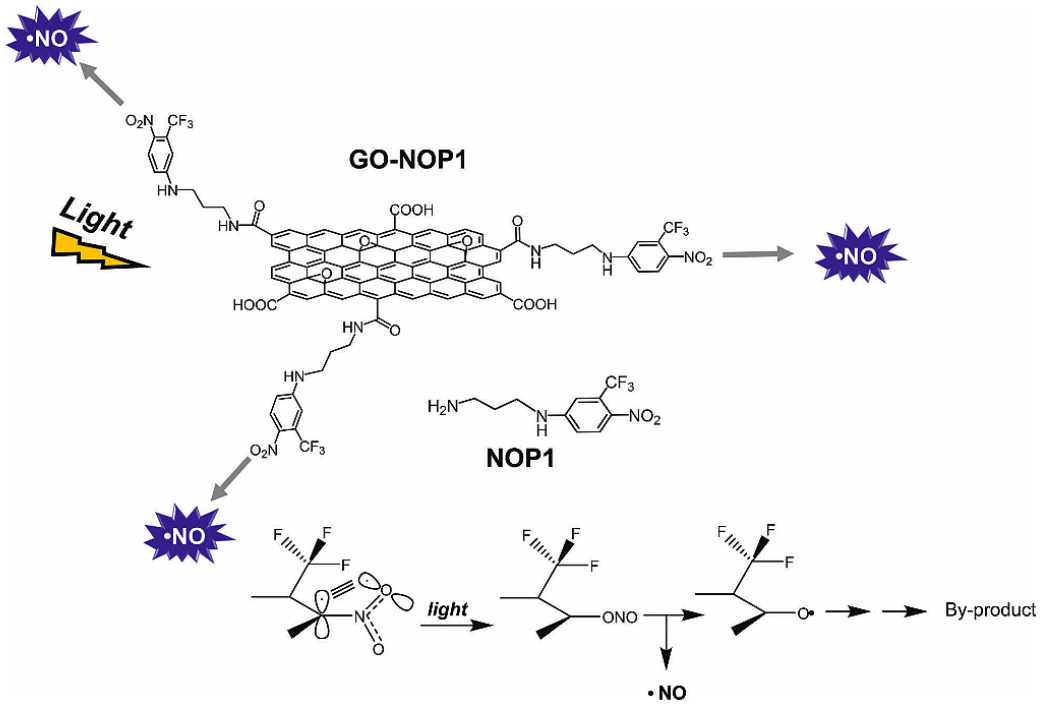

FIGURE 3.1: Schematic of the photoactivatable GO–NOP1 hybrid and the molecular structure of the model NO photodonor NOP1. A sketch of the mechanism for the photochemical NO release is also reported, for the sake of clarity.

that complement better-known photodynamic and photothermal therapies very well[28 29]. In this frame, although a number of photoactivatable GO-based constructs for potential application in photothermal and photodynamic therapies have been recently reported[30 31 32 33], GO-based nanoplatforms exhibiting light-regulated NO delivery are limited only to the recent work by Chen and coworkers[34]. They sandwiched a NO precursor between GO nanosheets. In this case, the former does not directly absorb the incident light but, instead, selectively excites the latter. Photoexcitation of GO triggers electron injection into the NO precursor, resulting in effective NO release. The critical need to develop more photoresponsive nanomedicines based on NO release on the GO scaffold and our ongoing interest in developing light-triggered NO delivering nanomaterials[20 21 22 23], are at the basis of the present work. In this contribution, we report a modified GO nanoplatform in which GO sheets are covalently functionalized with the NO photoreleaser NOP1, chosen as a suitable

model compound (Figure 3.1). The morphology, spectroscopic properties and photochemical behaviour of the resulting hybrid nanomaterial (GO–NOP1) have been characterized, emphasizing its capability to deliver NO remote-controlled by visible light stimuli.

3.2 Results and discussion

NOP1 is a derivative of 4-nitro-3-(trifluoromethyl)aniline, a NO photoreleaser developed in our group[35,36]. This chromogenic moiety possesses several important prerequisites for bioapplications, as it combines dark stability, an adequate absorption coefficient in the visible region, release of NO under the exclusive control of light inputs through a nitro-to-nitrite rearrangement (see Figure

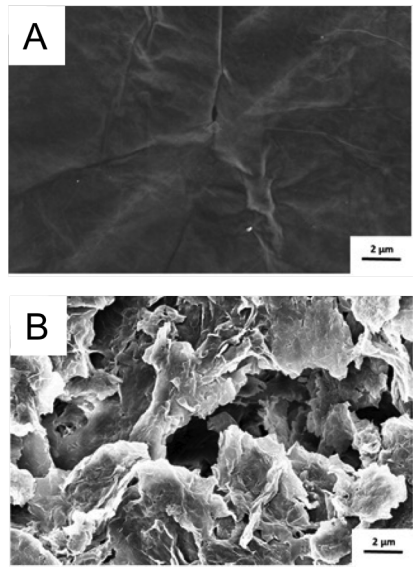

FIGURE 3.2: Representative SEM images of GO (A) and GO–NOP1 (B).

Moreover, its easy chemical modification enables it to be tailored in a number of ways to facilitate its integration into a variety of nanomaterials[20,21,22,23]. The choice of this NO photoreleaser for the preparation of the GO–NO hybrid is not casual and is rooted in the possibility of ruling out, in principle, any quenching effects by the GO platform via photoinduced energy and/or electron transfer processes. In fact: (i) the lack of any significant

emission of NOP1 prevents energy transfer quenching by the FRET mechanism[1]; (ii) the values of the reduction potential of GO (0.75 V vs. NHE)[37], the oxidation potential of NOP1 (41.4 V vs. NHE)[38] and the energy of the lowest excited state of NOP1 (ca. 2.4 eV) [2], make quenching by photoinduced electron transfer only slightly exergonic [3].

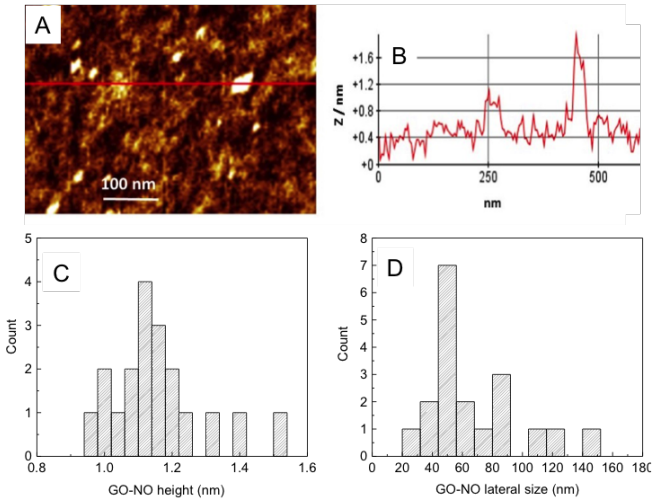

FIGURE 3.3: (A) Contact mode AFM of GO–NOP1 dried on a cleaned silicon surface. (B) Height line profile of the line shown in (A). (C) Height and (D) lateral dimension distributions of GO–NO.

Carboxylic acid groups located at the periphery of GO sheets were utilized to covalently graft NOP1 via amide bonds, exploit- ing its amino termination. The GO–NOP1 hybrid material was eventually obtained after repeated rinsing and centrifugation to remove any unbound NOP1 (see Experimental section). The morphology of NOP1 was investigated by contact-mode SEM, AFM, TEM and EDX. Figure 3.2 A reports a representative SEM image of the GO sheets, revealing a crumpled structure resulting from deformation during the exfoliation and restacking processes. Covalent linking of the amino terminated NOP1 to the carboxylic acid groups of GO gave GO–NO, which exhibits a higher degree of exfoliation (Figure 3.2 B), good dispersibility in water by ultrasonication, and reduced size (see below).

[1] Fluorescence emission from a donor is an indispensable pre-requisite for energy transfer via the FRET mechanism to occur.

[2] Estimated by the end of the absorption spectrum

[3] DG E 0.2 eV, estimated by the Rehm–Weller equation.

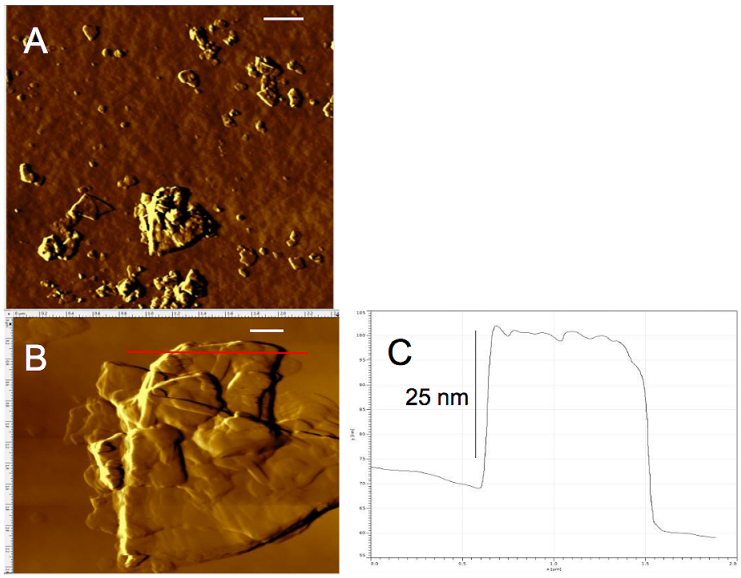

FIGURE 3.4: (A,B) Contact mode AFM of GO dried on cleaned silicon surface (scale bar 1μm in A and 0.2 μm in B). (C) Height line profile of red line shown in (B).

The thickness and the diameter of 19 sheets for a GO–NOP1 sample were measured by AFM in tapping mode. Figure 3.3 A shows the two-dimensional topography of GO–NOP1, and Figure 3.3 B reports the height profile of the continuous red line shown in Figure 3.3 A. The histogram distributions for the height and lateral size, obtained by analysis of different AFM images, are shown in Figure 3.3 C and D, respectively. The analysis revealed the presence of sheets with heights ranging between 0.9 and 1.5 nm and lateral dimensions ranging between 35 and 150 nm. A few sheets larger than 150 nm were found but were not included in the distribution. Considering the height of a single GO sheet as 0.8 to 1.0 nm[39] and the additional contribution from the linked NOP1, the AFM analysis accounts well for the predominance of single layers of exfoliated GO–NO nanosheets. This picture is quite different from that of GO, which showed heights of ca. 25 nm due to the significant presence of multilayers (Figure 3.4).

The morphology of the nanosheets was also investigated by high-resolution TEM. The image shown in Figure 3.5 indicates that the GO–NOP1 nanosheets are corrugated, while

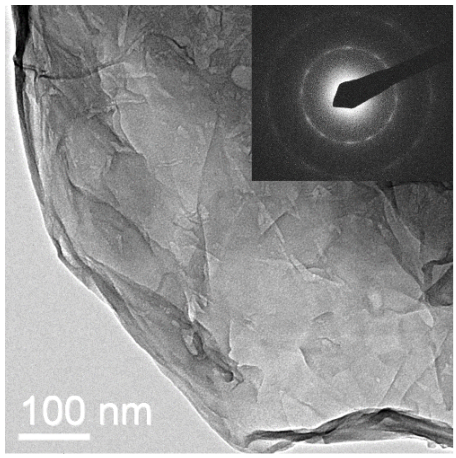

FIGURE 3.5: Representative TEM image of GO–NOP1 nanosheets. The inset shows the SAED pattern.

the selected area electron diffraction (SAED) pattern (see inset) indicates a crystalline structure. The first ring originates from the (1100) plane, while the second ring originates from the (1120) plane. The strong diffraction spots retain the typical hexagonal symmetry. Moreover, the SAED patterns contain information from many GO grains. As widely reported in the literature, this corrugation is typical for GO sheets and is attributed to the disruption of the planar sheets by the introduction of sp3-hybridized carbons during the oxidation process[40].

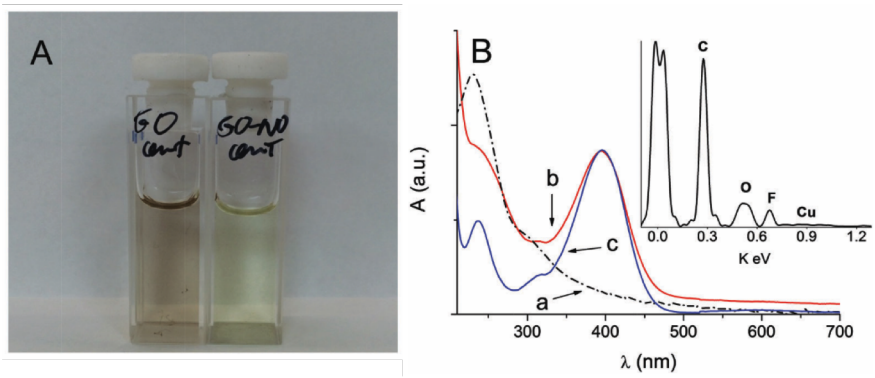

FIGURE 3.6: ((A) Actual images of aqueous suspensions of GO (left) and GO–NOP1 (right). (B) UV-Vis absorption spectra of aqueous suspensions of GO (a) and GO–NOP1 (b) and an aqueous solution of the NO photodonor NOP1 (c). The inset shows the EDX spectrum of the GO–NO sample.

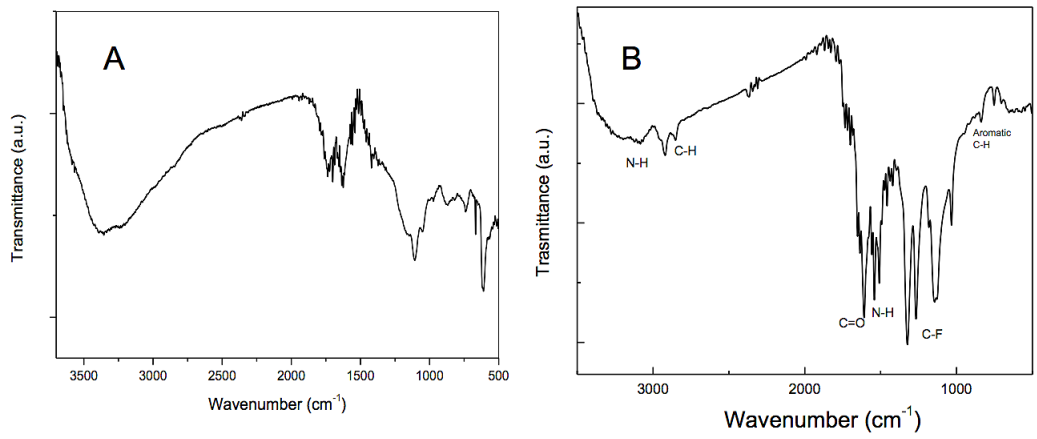

FIGURE 3.7: FTIR spectrum of (A) GO and (B) GO-NOP1

The successful functionalization of GO can be easily evidenced immediately by the naked eye due to the change in colour of the GO suspension from brown-yellow to clear yellow, consistent with the presence of the nitroaniline chromophore in GO–NOP1 (Figure 3.6 A). The covalent linking between NOP1 and the carboxylic group of GO was well supported by FTIR spectroscopy (Figure 3.7), showing the following diagnostic peaks for a primary amide: a sharp peak at 1640 cm^{-1} (CQO stretching), peaks in the region between 2900 and 3100 cm^{-1} (N–H stretching), and peaks in the range of 1550 to 1620 cm^{-1} (N–H bending); moreover, the peaks in the region between 1134 and 1450 cm 1 (C–F stretch) indicate the presence of the CF_3 group. The presence of the NO photodonor in the GO scaffold dominates the UV-Vis absorption spectrum. Figure 3.6 B shows that, in contrast to GO, the aqueous suspension of GO–NOP1 exhibits the unambiguous absorption band of the nitroaniline-derivative chromophore in the visible region, accompanied by an unstructured absorption in the UV due to the GO.

The EDX spectrum (see inset of Figure 3.6 B) showing the diagnostic fluoride peak at 0.68 keV indicates the presence of a fluoride group (such as $–CF_3$) on the GO–NOP1 surface and further supports the linking of the NO photodonor to the GO. The amount of NOP1 in GO–NOP1 was ca. 30% w/w (see Experimental section). Note that the visible absorption band of GO–NOP1 is broadened compared to that of an aqueous solution of the free model

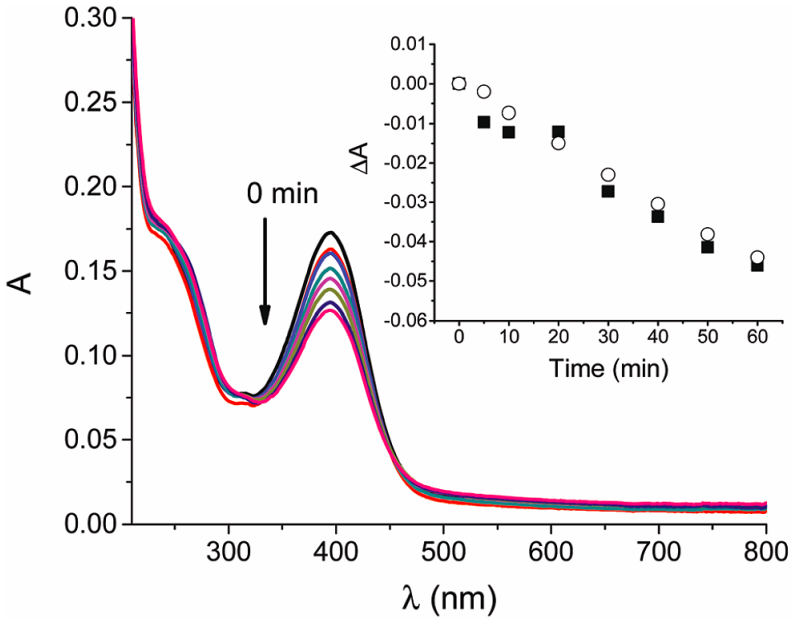

FIGURE 3.8: Absorption spectral changes observed upon 0, 5, 10, 20, 30, 40, 50, and 60 min of 405 nm light irradiation of an aqueous suspension of GO–NOP1 (25 mg mL 1). The inset shows the kinetic profiles, monitored at l = 400 nm observed for GO–NOP1 (■) and the model compound NOP1 (◯).

compound NOP1. This finding corroborates not only the linkage of NOP1 with the GO sheets but is also indicative of electronic interactions between the two species in the ground state, according to previous observations for other chromogenic species grafted to GO[32 41 42]. However, the position of the absorption maximum of GO–NOP1 undergoes a negligible shift if compared to the model NOP1. Our previous work demonstrated that the energy of the visible absorption band of the trifluoromethyl nitroaniline unit is very sensitive to both microenvironment polarity and changes in the geometry of the nitro group[42]. In this view, the similar spectroscopic features observed suggest that the nitro group retains its twisted conformation, which is necessary to trigger the photorelease of NO (Figure 3.1).

Figure 3.8 shows the absorption spectral changes as a function of irradiation time observed for a suspension of GO–NOP1 irradiated with visible light. The observed photobleaching of the main absorption band is in excellent agreement with the photochemical pathway leading to NO release previously proposed in the case of a single NO photodonor

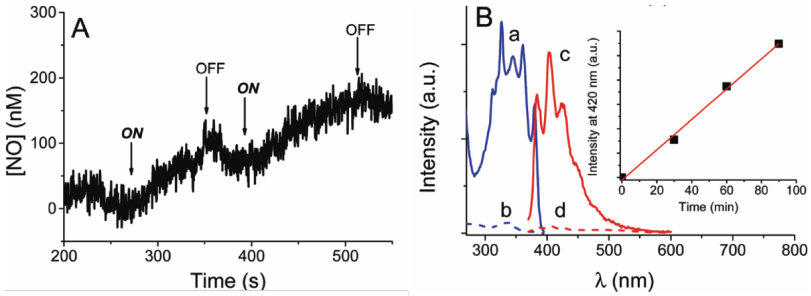

FIGURE 3.9: (A) NO release profile observed upon ON/OFF alternate irradiation cycles at 405 nm of a GO–NOP1 aqueous suspension (25 mg mL 1). (B) Fluorescence excitation (a, b, λ_{em} = 410 nm) and emission (c, d, λ_{ex} = 360 nm) spectra observed for aqueous suspensions of GO–NOP1 (25 mg·mL^{1}) in the dark (dotted) and after 60 min of 405 nm light irradiation (solid) and subsequent treatment with DAN of both samples. The inset shows increasing emission of DANT (characteristic product of DAN and NO) during the time of irradiation.

unit[35]. Comparative photolysis experiments carried out with an optically matched solution of the model compound NOP1 (inset Figure 3.8) show that the kinetics of the photobleaching is not significantly affected by the linkage of the NO photodonor to GO. This finding is in excellent agreement with our logical design (see above), ruling out any quenching effects (i.e. photoinduced energy/electron transfer) by the GO on the excited state of the NO photodonor involved in the photodecomposition. The most unambiguous methodology to demonstrate the generation of NO from GO–NOP1 nanosheets under visible light stimuli is direct and real-time monitoring of this radical species. To this end, we have used an ultrasensitive NO electrode which directly detects NO, with nM concentration sensitivity, by an amperometric technique[43]. The results illustrated in Figure 3.9A provide clear evidence that GO–NOP1 is stable in the dark, but supplies NO upon illumination with visible light. As confirmed by repeated ON/OFF cycles of illumination, the release process is strictly regulated by the external light inputs. The capability of GO–NOP1 to photorelease NO was also demonstrated by a very sensitive fluorimetric assay based on the use of 2,3-diaminonaphthalene (DAN) as a chemical trap[44]. The reaction of the non-fluorescent DAN with nitrite, which is formed by the reaction of NO with O_2, produces the highly fluorescent 2,3-naphthotriazole (DANT), which has characteristic fluorescence emission and excitation

spectra. As is evident from Figure 3.9B, only the irradiated GO–NOP1 sample leads to well-structured emission and excitation spectra typical of the DANT probe. Furthermore, the emission intensity of DANT increased linearly upon irradiation as a result of increasing NO photogeneration (inset of Figure 3.9B).

3.3 Conclusions

We have presented the synthesis of a new GO–NOP1 hybrid nanomaterial by condensation of an amino-terminated NO photodonor with GO. In this material, the photoactive component has been covalently grafted at the periphery of the GO platform, leading mainly to single nanosheets of GO–NOP1 that can be dispersed in aqueous media, are stable in the dark and can supply NO under exclusive control of visible light. Overall, this is one of the first and most promising reports of graphene-based hybrid materials for light-triggered NO delivery and can open intriguing opportunities for further studies in biomedical research, due to the multiple fascinating properties of the NO radical in medicine and biology.

3.4 Experimenta Sectionl

3.4.1 Chemicals

All chemicals were obtained from commercial sources at the highest possible purity and were used as received. All solvents used were spectrophotometric grade. Milli-Q-grade water was used in all preparations.

3.4.2 Synthetic procedures

NOP1 was synthetized according to a previous work[45].

N-(3-aminopropyl)-3-(trifluoromethyl)-4-nitrobenzenamine (NOPD): 1,3-propyldiamine (1.7 mL, 20 mmol) and Na_2CO_3 (2.12 g, 20 mmol) were refluxed in 50 ml of ethanol for 15 min. 4-cloro-2-(trifluoromethyl)-1-nitrobenzene (600 μL, 4 mmol) was then added and the

mixture was kept under continuous stirring for 3 days. After cooling down to ambient temperature the resulting suspension was filtered. The organic solution was concentrated under reduced pressure and purified by column chromatography (methanol 100%) to give NOPD (yield 45 %) as a yellow powder. Anal. Calcd (%) for $C_{10}H_{12}F_3N_3O_2$: C, 45.63; H, 4.60; N, 15.96; found: C, 44.33; H, 4.92; N, 16.54. ESI-MS m/z: [M+H]+ 264.2 (100%). ^{1}H-NMR CD_3OD: δ 7.93 (1H, d, J = 9.2 Hz), 6.90 (1H, d, J = 2.6 Hz), 6.69 (1H, dd, J_1 = 9.2 Hz, J_2 = 2.6 Hz), 3.19 (NH2CH2CH2CH2NH, 2H, t, J = 7.0 Hz), 2.71 (NH2CH2CH2CH2NH, 2H, t, J = 7.1 Hz), 1.74 (NH2CH2CH2CH2NH, 2H, m).

GO was synthesized at room temperature using the simplified Hummer method[46]. GO aqueous suspension (50 mL, 2 mg·mL^{-1}) was bath sonicated for 1 h to give a clear solution. NaOH (6.0 g) and chloroacetic acid (ClCH2COOH) (5.0 g) were then added to the GO suspension and bath sonicated for 3 h to convert the OH groups to COOH via conjugation of acetic acid moieties, giving GO–COOH[32]. The resulting GO–COOH solution was neutralized and purified by repeated rinsing and filtration. The GO–COOH was suspended in 40 mL MES solution (50 mM) to give a concentration of 2 mg mL 1. Then, 400 mg NHS and 200 mg EDC were added to the suspension and the mixture was sonicated for 60 min. The NO photodonor GO–NOP1 (300 mg) was then added, and the mixture was allowed to react overnight. The final product (GO–NOP1) was obtained by repeated rinsing and filtration. The loading capacity (LC%) was ca. 30% and was calculated using the formula below: LC% = W1/(WGO–NO) 100 where W1 is the amount of NOP1 in the GO–NO and WGO–NOP1 is the amount of GO–NOP1. The amount of NOP1 in the GO–NOP1 was determined spectrophotometrically at 400 nm (ϵ = 10 000 M^{-1} cm-1)[45].

3.4.3 Chemical detection of NO

We used the highly sensitive (detection limit on the order of the picomoles) fluorimetric bioassay of Misko et al.[44], based on the ring closure of DAN with nitrite to form the highly fluorescent product DANT. Briefly, once NO is photogenerated in aerobic conditions, in the absence of other scavengers, it is rapidly converted into nitrite and nitrate, its stable

metabolites. Nitrite reacts quantitatively with DAN to afford DANT. 1 mL aliquots of aqueous suspensions of GO–NOP1 were irradiated or maintained in the dark. Afterwards, 3.5 mL of 0.31 mM DAN in 0.62 M HCl were added, and the solutions were stirred for 20 min at room temperature. Afterwards, 100 mL of NaOH 2.8 M was added to the fluorescent cuvette, and the fluorescence emission and excitation spectra were recorded at λ_{exc} = 360 nm and λ_{em} = 410 nm, respectively

3.4.4 Instrumentation

Atomic Force Microscopy (AFM) images were acquired in air using a Digital 3100 instrument in tapping mode. Commercially available tapping etched silicon probes (Digital) with a pyramidal shape tip having a nominal curvature of 10 nm and a nominal internal angle of 35° were used. The samples for AFM analysis were prepared as follows: a water-diluted suspension of GO-NOP1 was treated with ultrasound for 5 minutes. 10 mL of the sample solution were deposited on a freshly cleaned silicon slide (the silicon slide was cleaned by the Plasma-O_2 process for 10 min at 100 W). After that, the residual liquid on the surface was removed. The sample was dried in air before the measurement. SEM images were obtained using a high performance Schottky field emission LEO 1550 SEM. The instrument was operated at 5 kV in secondary electron imaging mode. Transmission electron microscopy (TEM) experiments were performed using the bright field in conventional parallel beam (CTEM) mode (BF). A JEOL JEM-2010 TEM equipped with a 30 mm^2 window energy dispersive X-ray (EDX) spectrometer was used. UV-Vis spectra were recorded with a JascoV-560 spectrophotometer using quartz cells with a path length of 1 cm. FTIR spectra were recorded with a Perkin-Elmer spectrophotometer. Irradiation of the samples was performed in a thermostated quartz cell (1 cm path length, 3 mL capacity) under gentle stirring using a continuum laser with λ_{ex}c = 405 nm (ca. 200 mW) having a beam diameter of ca. 1.5 mm. NO release was measured with a World Precision Instruments ISO-NO meter equipped with a data acquisition system based on direct amperometric detection of NO with a short response time (<5 s) and a sensitivity range of 1 nM to 20 mM. The analog

signal was digitalized with a four-channel recording system and transferred to a PC. The sensor was accurately calibrated by mixing standard solutions of $NaNO_2$ with 0.1 M H_2SO_4 and 0.1 M KI according to the reaction:

$$4H^+ + 2I^- + 2NO_2 \longrightarrow 2H_2O + 2NO + I_2$$

Irradiation was performed in a thermostated quartz cell (1 cm path length, 3 mL capacity) under gentle stirring using the 405 nm laser described above. NO measurements were carried out with the electrode positioned outside the light path in order to avoid false NO signals due to photoelectric interference on the ISO-NO electrode.

3.5 Additional results

GO is also able to convert visible light into heat, leading to interesting photothermal effects. To this goal, the samples were irradiated with a 532 nm CW laser. The results are shown in Figure 3.10 where it can be noted a relevant temperature increase upon light irradiation, which is also dependent on the concentration of nanoGO.

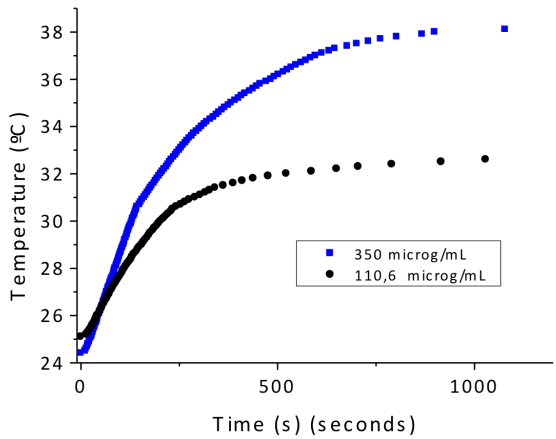

FIGURE 3.10: Increase of temperature depending on irradiation time with 532 nm laser (200 mA) of GO 1,5 mL in a Eppendorf.

3.5.1 Conclusions

A GO nanoplatform covalently grafted to a NO photodonor was made and characterized. It presents stability in the dark, leading to the NO production only under visible light stimulation. In addition, the GO nanoplatform exhibits photothermal under visible light irradiation. These proprieties confer to the nano-GO a light triggered bimodal action, which will be exploding in forthcoming biological investigations. Future strategies pretend the incorporation of a fluorescent reporter, or others molecules producing different cytotoxic species, again, to enjoy the benefits of a multimodal antibacterial system.

Bibliography

[1] Stoller, M. D.; Park, S.; Zhu, Y.; An, J.; Ruoff, R. S. *Nano letters* **2008**, *8*, 3498–3502.

[2] Li, X.; Wang, X.; Zhang, L.; Lee, S.; Dai, H. *science* **2008**, *319*, 1229–1232.

[3] Robinson, J. T.; Perkins, F. K.; Snow, E. S.; Wei, Z.; Sheehan, P. E. *Nano letters* **2008**, *8*, 3137–3140.

[4] Pyun, J. *Angewandte Chemie International Edition* **2011**, *50*, 46–48.

[5] Zhang, H.; Grüner, G.; Zhao, Y. *Journal of Materials Chemistry B* **2013**, *1*, 2542–2567.

[6] Mao, H. Y.; Laurent, S.; Chen, W.; Akhavan, O.; Imani, M.; Ashkarran, A. A.; Mahmoudi, M. *Chemical reviews* **2013**, *113*, 3407–3424.

[7] Liu, J.; Cui, L.; Losic, D. *Acta biomaterialia* **2013**, *9*, 9243–9257.

[8] others,, et al. *Nature reviews. Drug discovery* **2008**, *7*, 771.

[9] Ignarro, L. J. *Nitric oxide: biology and pathobiology*; Academic press, 2000.

[10] Walford, G.; Loscalzo, J. *Journal of Thrombosis and Haemostasis* **2003**, *1*, 2112–2118.

[11] Fang, F. C. *Nitric oxide and infection*; Springer, 1999.

[12] Packer, L. *Nitric Oxide: Biological and antioxidant activities*; Gulf Professional Publishing, 1999; Vol. 301.

[13] others,, et al. *Acta Pharmacologica Sinica* **2005**, *26*, 259–264.

[14] Fukumura, D.; Kashiwagi, S.; Jain, R. K. *Nature reviews. Cancer* **2006**, *6*, 521.

[15] Mocellin, S.; Bronte, V.; Nitti, D. *Medicinal research reviews* **2007**, *27*, 317–352.

[16] Wang, P. G.; Xian, M.; Tang, X.; Wu, X.; Wen, Z.; Cai, T.; Janczuk, A. J. *Chemical reviews* **2002**, *102*, 1091–1134.

[17] Wang, P. G.; Cai, T. B.; Taniguchi, N. *Nitric oxide donors: for pharmaceutical and biological applications*; John Wiley & Sons, 2005.

[18] Riccio, D. A.; Schoenfisch, M. H. *Chemical Society Reviews* **2012**, *41*, 3731–3741.

[19] Seabra, A. B.; Durán, N. *Journal of Materials Chemistry* **2010**, *20*, 1624–1637.

[20] Sortino, S. *Chemical Society Reviews* **2010**, *39*, 2903–2913.

[21] Sortino, S. *Journal of Materials Chemistry* **2012**, *22*, 301–318.

[22] Fraix, A.; Sortino, S. *Chemistry–An Asian Journal* **2015**, *10*, 1116–1125.

[23] Fraix, A.; Marino, N.; Sortino, S. *Light-Responsive Nanostructured Systems for Applications in Nanomedicine*; Springer, 2016; pp 225–257.

[24] Ford, P. C. *Nitric oxide* **2013**, *34*, 56–64.

[25] Ford, P. C. *Accounts of chemical research* **2008**, *41*, 190–200.

[26] Fry, N. L.; Mascharak, P. K. *Accounts of chemical research* **2011**, *44*, 289–298.

[27] Ostrowski, A. D.; Ford, P. C. *Dalton Transactions* **2009**, 10660–10669.

[28] Hasan, T.; Moor, A. C. E.; Ortel, B. *Inc.: Hamilton, Ontario, Canada* **2000**,

[29] Jain, P. K.; Huang, X.; El-Sayed, I. H.; El-Sayed, M. A. *Accounts of chemical research* **2008**, *41*, 1578–1586.

[30] Sahu, A.; Choi, W. I.; Lee, J. H.; Tae, G. *Biomaterials* **2013**, *34*, 6239–6248.

[31] Robinson, J. T.; Tabakman, S. M.; Liang, Y.; Wang, H.; Sanchez Casalongue, H.; Vinh, D.; Dai, H. *Journal of the American Chemical Society* **2011**, *133*, 6825–6831.

[32] Zhang, W.; Guo, Z.; Huang, D.; Liu, Z.; Guo, X.; Zhong, H. *Biomaterials* **2011**, *32*, 8555–8561.

[33] Markovic, Z. M.; Harhaji-Trajkovic, L. M.; Todorovic-Markovic, B. M.; Kepić, D. P.; Arsikin, K. M.; Jovanović, S. P.; Pantovic, A. C.; Dramićanin, M. D.; Trajkovic, V. S. *Biomaterials* **2011**, *32*, 1121–1129.

[34] Fan, J.; He, N.; He, Q.; Liu, Y.; Ma, Y.; Fu, X.; Liu, Y.; Huang, P.; Chen, X. *Nanoscale* **2015**, *7*, 20055–20062.

[35] Caruso, E. B.; Petralia, S.; Conoci, S.; Giuffrida, S.; Sortino, S. *Journal of the American Chemical Society* **2007**, *129*, 480–481.

[36] Conoci, S.; Petralia, S.; Sortino, S. Use of nitroaniline derivatives for the production of nitric oxide. 2014; US Patent 8,766,006.

[37] Shao, Y.; Wang, J.; Engelhard, M.; Wang, C.; Lin, Y. *Journal of Materials Chemistry* **2010**, *20*, 743–748.

[38] Jonsson, M.; Lind, J.; Eriksen, T. E.; Merenyi, G. *Journal of the American Chemical Society* **1994**, *116*, 1423–1427.

[39] Gómez-Navarro, C.; Weitz, R. T.; Bittner, A. M.; Scolari, M.; Mews, A.; Burghard, M.; Kern, K. *Nano letters* **2007**, *7*, 3499–3503.

[40] others,, et al. *Chemistry of materials* **2007**, *19*, 4396–4404.

[41] Karousis, N.; Sandanayaka, A. S.; Hasobe, T.; Economopoulos, S. P.; Sarantopoulou, E.; Tagmatarchis, N. *Journal of Materials Chemistry* **2011**, *21*, 109–117.

[42] Sortino, S.; Marconi, G.; Condorelli, G. *Chemical Communications* **2001**, 1226–1227.

[43] Coneski, P. N.; Schoenfisch, M. H. *Chemical Society Reviews* **2012**, *41*, 3753–3758.

[44] Misko, T. P.; Schilling, R.; Salvemini, D.; Moore, W.; Currie, M. *Analytical biochemistry* **1993**, *214*, 11–16.

[45] Callari, F. L.; Sortino, S. *Chemical Communications* **2008**, 1971–1973.

[46] Huang, N.; Lim, H.; Chia, C. H.; Yarmo, M. A.; Muhamad, M. *International journal of nanomedicine* **2011**, *6*, 3443.

Part II

Molecular hybrids systems

Chapter 4

Hydrogel

4.1 Introduction

Another research line to fight DR is the development of hydrogels and films with antibacterial activity. Some polymers soluble in water are able to form hydrogels by covalent bond, or physical interactions (hydrophobic, electrostatic or hydrogen bond)[1,2]. Supramolecular gels manufactured in water is a green chemistry choice, and Inclusion of silver nanoparticles inside the hydrogel is expected to give it antibacterial activity. For this aim, the same polymer used in chapter 2 will be used in addition to poli-β-CD polymer. The formation is this supramolecolar structure is expected to follow the "lock and key" mechanism: dextran chains will be included into cyclodextrin cavities[3].

Thanks to the transparency of the gel, benzophenone could be activated subsequently by light to form AgNPs.

4.2 Experimental

Dextran-benzophenone and poli-β-CD polymer polymer have been furnish by Dr. Gref's groups, from Universitd de Paris. All the solutions were prepared with MilliQ water, and the reactives were supplied by Sigma-Aldrich. The quartz cells were clean before every experiment with aqua regia. A stock solution of 2,5% dextran was prepared by dissolving it

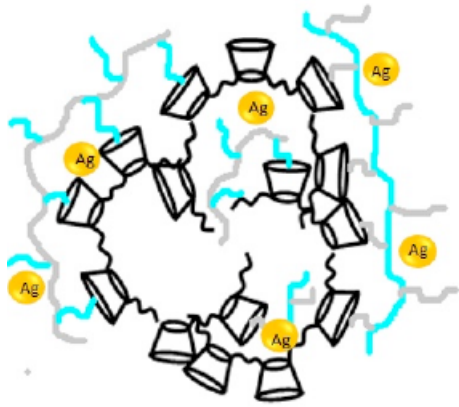

FIGURE 4.1: Hypothetical structure of gel

in MilliQ water. The unknown concentration of BP was obtained measuring the UV-visible absorption, then using the Beer-Lamber law (A= $\epsilon \cdot l \cdot c$) it was calculated:

A(261)=1,942 and λ=17 000 M^{-1}·cm^{-1}, so $[BP]_0$=1,14·10^{-2}M.

4.3 Instrumentation

UV-vis absorption and fluorescence spectra were recorded with a Jasco V 650 spectrophotometer. Irradiation was performed in a thermostated quartz cell (1 cm pathlength, 3 mL capacity) by using a Rayonet photochemical reactor equipped with 5-10 RPR lamps with an emission in the 320-380 nm range with a maximum at 350 nm.

4.4 Results and discussion

Under magnetic stirring, DXT-BP 500 μL (140 mg/mL) and AcacAg 30 μL were mixed togheter. The posterior addition of p-β-CD 500 μL (140 mg/mL) produced a partial gelification (Figure **??**).

The subsequent irradiation of the mixture in the photoreactor with 10 lamps at λ_{exc}= 350 nm under magnetic stirring increased the viscosity of the gel as we can se in Figure X. We can also observe intensification of yellow colour after the irradiation, due to the formation

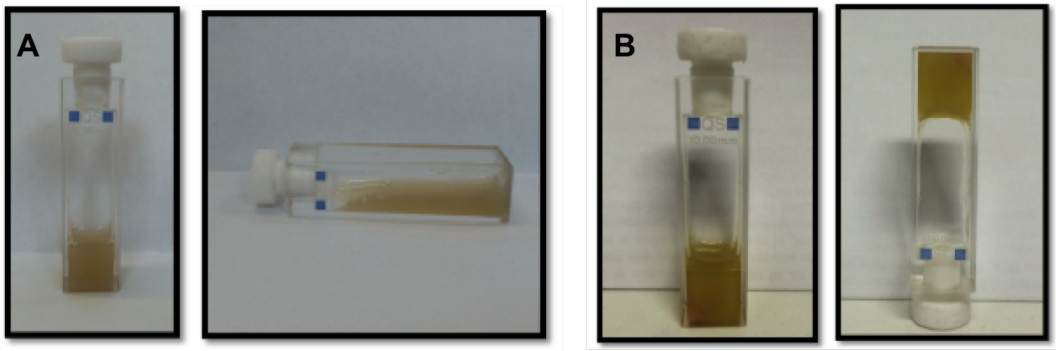

FIGURE 4.2: Hydrogel before (A) and after (B) irradiation

of silver nanoparticles, confirmed by UV-visible spectra. As we can se in Figure X, the apparition of the characteristic plasmon band around 400 nm confirms the presence of silver nanoparticles.

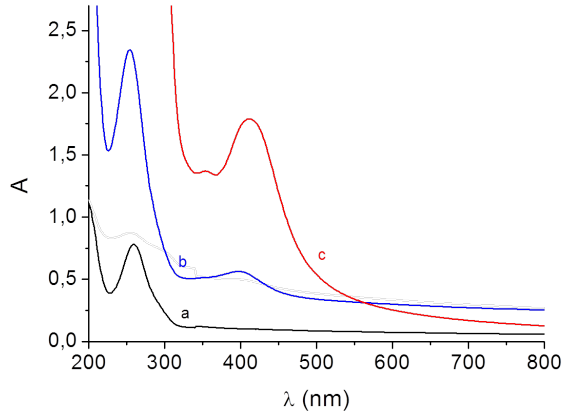

FIGURE 4.3: UV-visible absorption spectra of gel before irradiation (a), after (b) and water supernatant stirred 5h (c).

Once formed, 2 mL of water were added to gel and kept at dark under magnetic stirring for 5h. The UV-visible absorption spectrum shows release of AgNPs to the water.

4.5 Conclusions

We achieved the formation of a hydrogel encapsulating AgNPs and able to release them in water suspension. Further experiments will be carried out to confirm their antibacterial activity.

Bibliography

[1] Hunt, J. N.; Feldman, K. E.; Lynd, N. A.; Deek, J.; Campos, L. M.; Spruell, J. M.; Hernandez, B. M.; Kramer, E. J.; Hawker, C. J. *Advanced Materials* **2011**, *23*, 2327–2331.

[2] Lemmers, M.; Sprakel, J.; Voets, I. K.; van der Gucht, J.; Stuart, C.; Martien, A. *Angewandte Chemie International Edition* **2010**, *49*, 708–711.

[3] Fraix, A.; Gref, R.; Sortino, S. *Journal of Materials Chemistry B* **2014**, *2*, 3443–3449.

Chapter 5

Antibacterial Film

Photo-antimicrobial polymeric films releasing nitric oxide with fluorescence reporting under visible light

Published as:

Authors: Nino Marino, Marta Perez-Lloret, Anna R. Blanco, Alessandro Venuta, Fabiana Quaglia and Salvatore Sortino.

Journal: Journal of Materials Chemistry B, 2016, vol. 4, no 30, p. 5138-5143.

5.1 Introduction

The emergence of multi-drug resistance (MDR) bacteria[1 2 3] and the increase of opportunistic infections[4 5] associated with the alarmingly low turnover of new clinically approved antibiotic drugs[6] call for a shift of attention to other underappreciated or unexploited antibacterial treatment modalities. In this frame, one of the most promising approaches is based on the use of nitric oxide (NO) as a powerful antimicrobial agent[7 8]. This small sized and uncharged radical does not suffer MDR problems[9] and represents a multitarget therapeutic species[10] with broad-spectrum antibacterial activity. Besides, as a result of its short half-life in blood (<1 s), NO diffuses into the cellular environment over short distances (<200 μm)[11] confining the region of action and consequently avoiding systemic toxicity issues. Difficulties in the delivery of gaseous NO to selected targets have inspired the development of a range of molecular NO-donors[12;13] and their integration within a variety of materials where NO delivery is triggered by metabolic or light stimuli has been recently reported[14 15 16 17 18 19 20]. Among these, photobactericidal film coatings are of particular relevance[21 22 23 24] not only due to the superb spatiotemporal control of NO that the light input offers[18] but also because they can be designed for a large use both inside and outside the human body. The therapeutic effects of NO are, however, strictly dictated by its concentration[25]. This feature makes the quantification of the NO delivery a very important issue to be faced, especially when one is interested to reach a critical molecule concentration to induce a specific effect. A suitable way to address this quantification task is based on the use of a fluorescent reporter. This elegant strategy relies on the simultaneous photorelease of the desired bioactive species, i.e. NO, and a fluorescent component (the reporter) from the same nonfluorescent precursor[26 27 28]. In such a way, the release process can be easily quantified by monitoring the fluorescence emission of the reporter, which acts exactly as an optical counter of the bioactive species. NO photoreleasers with fluorescence reporting function have only recently attracted attention[29;30 31 32], mainly limited to the solution phase. In the frame of our ongoing interest in NO photoreleasing constructs for therapeutic applications[17 18 33 34], we report herein the first example of an NO photoreleasing antibacterial

film with fluorescence reporting function.

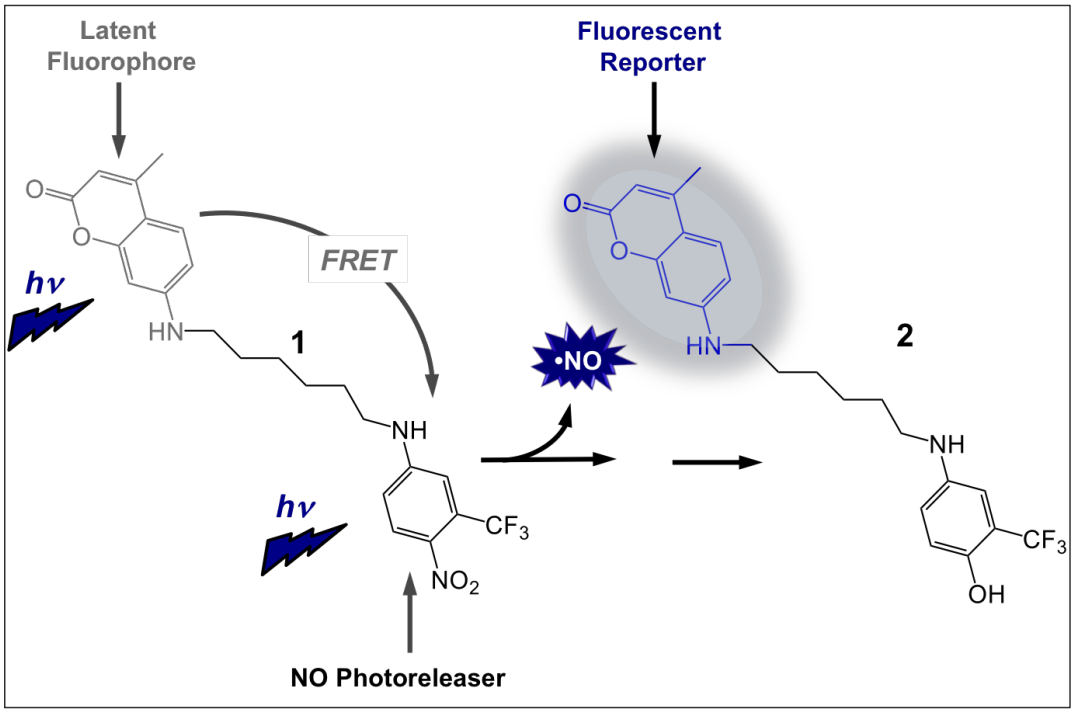

FIGURE 5.1: The working principle of the functional molecular hybrid 1.

5.2 Results and discussion

To achieve our goal, we have designed the molecular hybrid 1 as a multifunctional component (Figure 5.1). It consists of a nitroaniline-based NO photodonor developed in our group[35,36], linked to the coumarin 120 through an alkyl spacer. The working principle of 1 is sketched in Figure 5.1 and the rationale behind the design of this molecular hybrid is described in the following.

The coumarin component has been chosen because its intense fluorescence emission spectrum overlaps extensively the absorption spectrum of the nitroaniline NO photodonor (Figure 5.2). This condition, the close proximity of the two chromophores and the flexibility of the alkyl spacer are key prerequisites to make the fluorescence of the coumarin

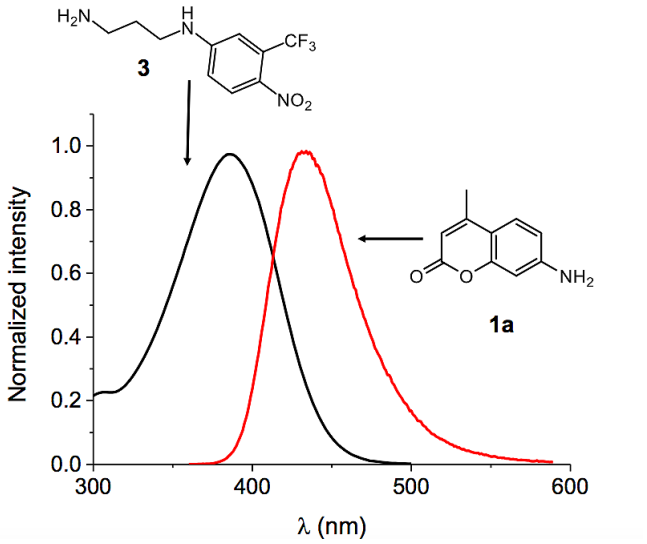

FIGURE 5.2: Spectral overlap between the fluorescence emission of coumarin 1a (red) and the absorption of the NO photoreleaser 3 (black). This latter was synthesized according to our already reported procedure[37].

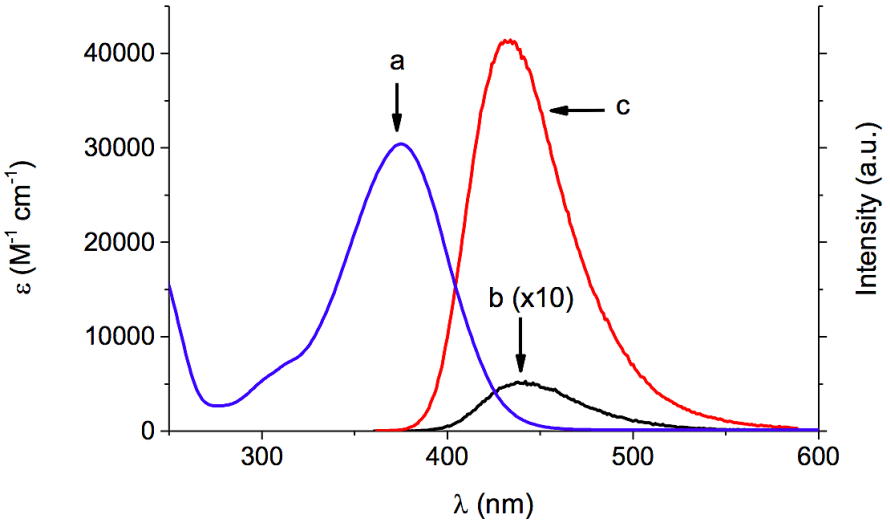

FIGURE 5.3: Absorption spectrum of the molecular hybrid 1 in methanol (a) (left y axis) and fluorescence emission spectrum of optically matched methanol solutions of 1 (b) and the coumarin derivative 1a (c) (λ_{exc} = 360 nm) (righ y axis). Spectrum b has been multiplied for 10, for a sake of clarity.

significantly quenched in the conjugate 1 by a Förster resonance energy transfer (FRET) mechanism. Excitation with visible light is expected to trigger NO photorelease from the nitroaniline moiety leading to a phenol derivative as a stable byproduct[35 36]. In contrast to the nitroaniline chromophore this moiety is not able to accept the energy from the excited coumarin since its absorption spectrum, falling in the UV region, does not overlap any more the emission spectrum of the coumarin, making the FRET process thermodynamically not feasible. Consequently, the coumarin fluorescence is expected to be restored upon NO photorelease. The validity of our design was firstly proven by spectroscopic and photochemical experiments performed in solution. The absorption spectrum of 1 reflects fairly well the sum absorption spectrum of the independent coumarin and nitroaniline compounds (Figure 5.3), ruling out any significant interaction between the coumarin and nitroaniline chromophores in the ground state. On the other hand, the fluorescence emission of the coumarin fluorophore is significantly quenched in the case of the conjugate 1 (Figure 5.3), suggesting a remarkable interaction between the two chromophores in the excited state.

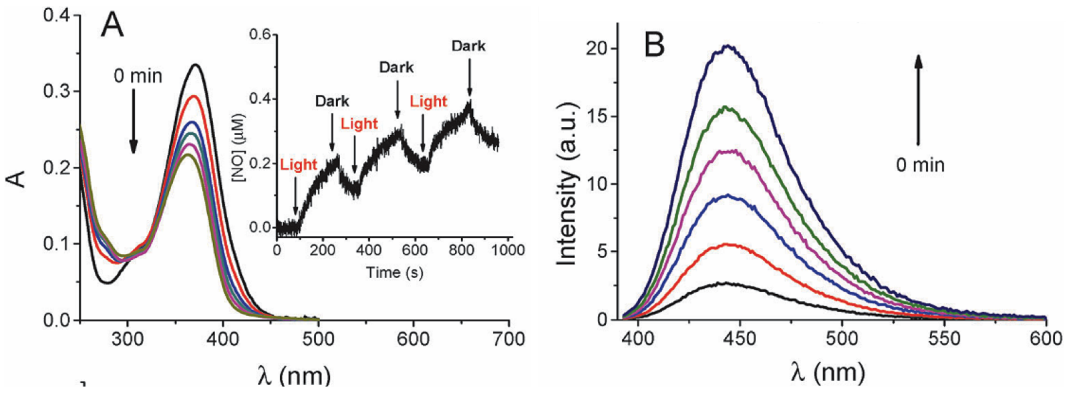

FIGURE 5.4: (A) Absorption spectral changes observed upon exposure of a water:methanol (20:80 v/v) solution of 1 (15 mM) at λ_{exc} = 405 nm for regular intervals of 10 min. T = 25°C; the inset shows a representative NO release profile from 1. (B) Evolution of the fluorescence emission spectra corresponding to the sample of (A) and recorded at λ_{exc} = 380 nm.

Photoexcitation of 1 leads to a bleaching of the main absorption band (Figure 5.4A). This behaviour accords with the photorelease of NO and the formation of the phenol derivative 2 as a stable photoproduct since it is in line with the photochemical pathway leading to NO

release previously proposed in the case of the single NO photodonor unit[35,36]. This was confirmed by the typical NO release profile obtained by the direct amperometric detection of this species in alternating cycles of light/dark shown in the inset of Figure 5.4A. Besides, the ESI-MS analysis of the crude reaction mixture carried out immediately after the photolysis experiments (ca. 20% transformation) revealed a main peak with a [M + 1]+ value of 434.2, corresponding to the structure of the conjugate 2 (Figure 5.1) in addition to that of the remaining starting compound. Figure 5.4B shows the evolution of the fluorescence emission spectra corresponding to the absorption changes reported in Figure 5.4A. These findings clearly indicate that photodecomposition of 1 leads to a dramatic revival of the characteristic emission of the coumarin fluorophore which can be used as an optical reporter for the NO release.

Polymeric films containing the functional conjugate 1 (16 mg·cm^2) were prepared by solvent casting using poly(lactic- co-glycolic acid) (PLGA) as a suitable polymeric matrix. PLGA is a highly biocompatible polymer approved for biomedical use, which has been recently used as a scaffold for the fabrication of NO releasing films triggered by pH changes[38,39] or chemically modified to achieve NO release under UV light irradiation[21]. The film exhibited a homogeneous distribution of 1 in the polymeric matrix (see Experimental) and an excellent optical transparency which allowed us to record its UV-Vis absorption spectra in transmission mode (vide infra). The incorporation of the functional molecular hybrid into the polymeric film does not change the nature of the photochemical process. Figure 5.5A and B show the absorption and fluorescence spectral changes observed upon irradiation of the film with visible light.

Apart from a slight spectral shift due to a solvent effect, the behaviour observed is very similar to that exhibited by 1 in solution (see comparison with Figure 5.3), since characterized by a bleaching of the main absorption band accompanied by a remarkable increase of the fluorescence intensity upon irradiation. NO photorelease from the film was detected by means of the sensitive and selective chemical method for NO detection based on the reaction between N2O3 (formed by reaction of NO with O_2) and 2,3-diamino-naphthalene

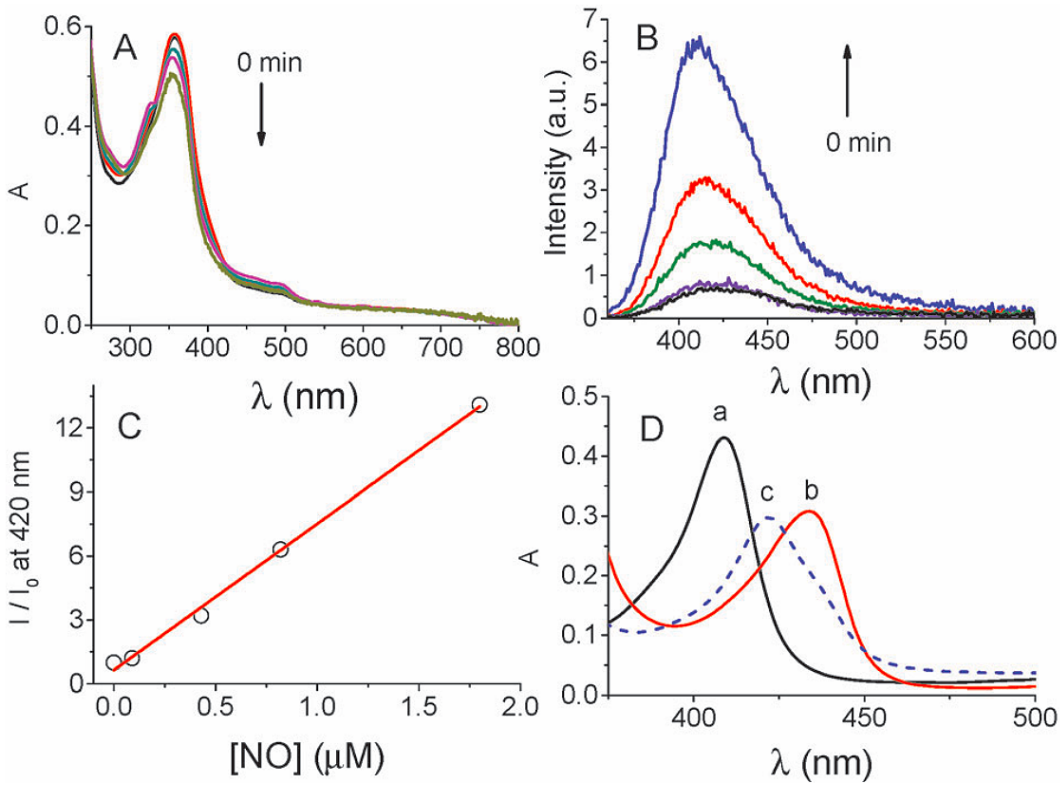

FIGURE 5.5: Absorption (A) and fluorescence (B) (λ_{exc} = 350 nm) spectral changes observed upon irradiation of the PLGA film doped with 1 for 0, 1, 5, 10 and 20 min with a Xe lamp (cut-off filter l 4 400 nm). (C) Correlation of the fluorescence increase observed in (B) and the concentration of NO released from the film (I and I0 represent the fluorescence intensities after and before irradiation, respectively). (D) Transfer of NO from the PLGA film to reduced Mb in phosphate buffer. Absorption spectra of oxidized Mb(FeIII) (a) and reduced Mb(FeII) before (b) and after (c) 50 min of irradiation of the film. [Mb] = 2.5 mM; cell pathlength = 1 cm.

(Figure 5.6). As illustrated in Figure 5.5C, we found an excellent linear correlation between the concentration of NO photogenerated and the increase of the fluorescence intensity of the optical reporter. The doped PLGA film is a convenient NO dispenser for biological targets as demonstrated by its capability to transfer NO to a solution of equine skeletal myoglobin (Mb)[40] where the film was immersed. NO delivery to Mb can be easily monitored by absorption spectroscopy and the results obtained are illustrated in Figure 5.5D. Mb exhibits its Soret absorption band at 410 nm (spectrum a). The addition of dithionite resulted in a shift of the absorption maximum at 432 nm, corresponding to the reduction of Mb (spectrum

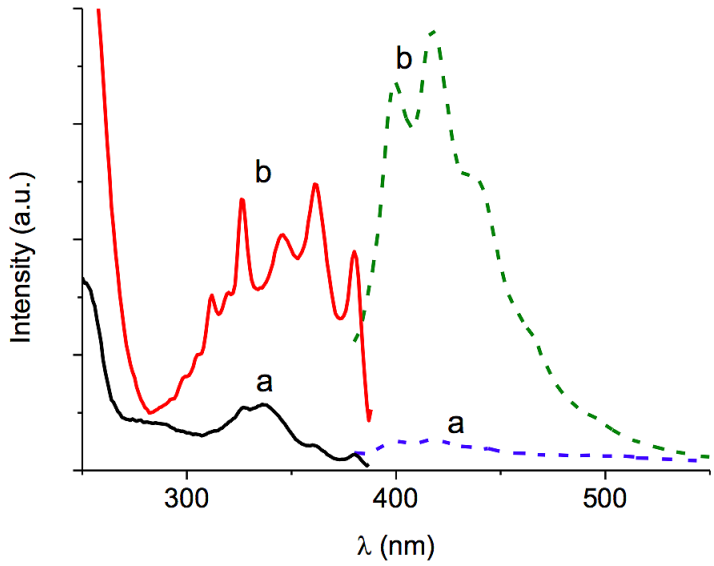

FIGURE 5.6: Representative fluorescence emission (dotted) and excitation (solid) spectra obtained after fluorimetric assay of non-irradiated (a) and irradiated (b) polymeric film of PLGA doped with 1 in phosphate buffer solutions 10 mM at pH 7.4. Emission spectrum at λ_{exc} = 360 nm; excitation spectrum at λ_{em} = 410 nm

b). After irradiation of the film, the spectrum of the supernatant showed the appearance of a new Soret absorption band at 420 nm which, according to the literature,18 confirms the binding of NO to the Fe(II) of the heme group of Mb (spectrum c). Control experiments performed irradiating the solution containing the reduced Mb (i) in the absence of the film, (ii) in the presence of the film without 1 or (iii) keeping the film doped with 1 in the dark did not show any evidence for the formation of the 420 nm band. It is important to note that NO is indeed released from the film and not from molecules of 1 diffusing from the film to the supernatant solution. In fact, the leaching test performed by leaving the film immersed in a phosphate buffer solution (pH 7.4, 10 mM) at room temperature in the dark did not show any detectable absorption spectrum of 1 in the solution over a period of one week, according to the insolubility of 1 in this medium.

Interestingly, the release process with fluorescence reporting in the polymeric film is also triggered by sunlight and can be easily followed by the naked eye. The as-prepared PLGA

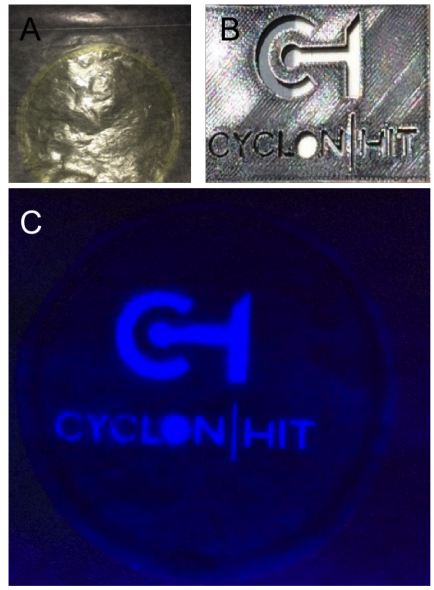

FIGURE 5.7: PLGA film (A) and its selective exposition to sunlight for 30 min with a black plastic mask on top (B). Fluorescence image (λ_{exc} = 350 nm) of the irradiated film after removing the mask (C).

film (Figure 5.7A) was covered with a black plastic mask (Figure 5.7B) and left for 30 min outdoor under sunlight. Figure 5.7C shows the typical blue fluorescence of the reporter arising only from the illuminated sites, accounting for a remarkable spatial differentiation between the illuminated and non-illuminated areas. This finding clearly demonstrates that it is therefore possible to deliver NO to a specific location by either the covering of the surrounding areas or appropriately focusing the light source.

Antibacterial activity of the film was tested towards Gram- negative *Escherichia coli* ATCC 25922 bacteria strain. The results in Figure 5.8 show that no effect on the bacterial growth is observed both in the presence of the film in the dark (A) and under illumination in the absence of the film (B). On the other hand, a remarkable reduction of the number of colonies was observed after irradiation with visible light in the presence of the PLGA film, in a manner clearly dependent on the irradiation time (C and D).

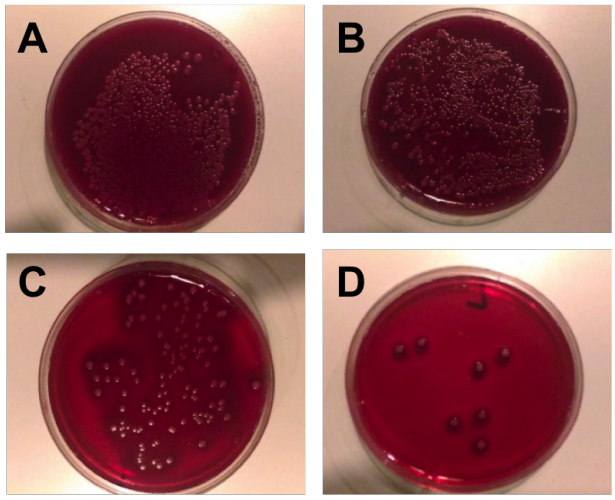

FIGURE 5.8: MacConkey's agar plates inoculated with 20 mL of bacterial suspensions of Escherichia coli ATCC 25922 (ca. CFU 5 104 mL1) after incubation with the PLGA film in the dark (A) and irradiated for 5 min (C) and 20 min (D). Control of the bacterial suspension after 20 min of irradiation in the absence of the PLGA film (B). Irradiation was performed with a 470 W Xe lamp, cut-off filter $\lambda > 400$ nm

5.3 Conclusions

We have achieved a biocompatible film of PLGA incorporating a novel tailored NO photoreleaser. The polymeric film is stable in the dark but it is able to release substantial amounts of NO with spatiotemporal control under excitation with visible light. The release process can be activated even by sunlight exposure and can be followed in real time by the intense blue fluorescence of a by-product, which acts as a convenient optical reporter of the NO concentration. To our knowledge, this is the first time that NO release with fluorescence reporting is demonstrated in film samples. Once photogenerated, the NO radical promptly diffuses out of the polymeric matrix to reach biological targets. The film shows excellent and strictly light-dependent bactericidal activity against the Gram-negative E. Coli ATCC 25922 bacterial strain, opening intriguing possibilities for its further engineering in the perspective of coating and devices for biomedical applications. Finally, we would like to stress that the FRET mechanism occurring in compound 1 and the high two-photon cross-section

of the coumarin chromophore offer, in principle, the possibility to trigger the NO photorelease and to detect the fluorescence of the reporter by two-photon excitation (TPE) of the coumarin component. In this regard, the study in progress in our laboratories is ongoing to demonstrate the possibility of the present system to eradicate biofilms with very high spatial resolution via TPE.

5.4 Experimental Section

5.4.1 Chemicals

All chemicals were from commercial sources at the highest possible purity and used as received. All solvents used were of spectrophotometric grade.

5.4.2 Synthesis

Compound 1 was synthesized according to the synthetic steps illustrated in Figure 5.9 and described in the following. Syntheses were carried out at a low intensity level of visible light. Compounds 1a and 1b were synthesized according to literature procedures[41].

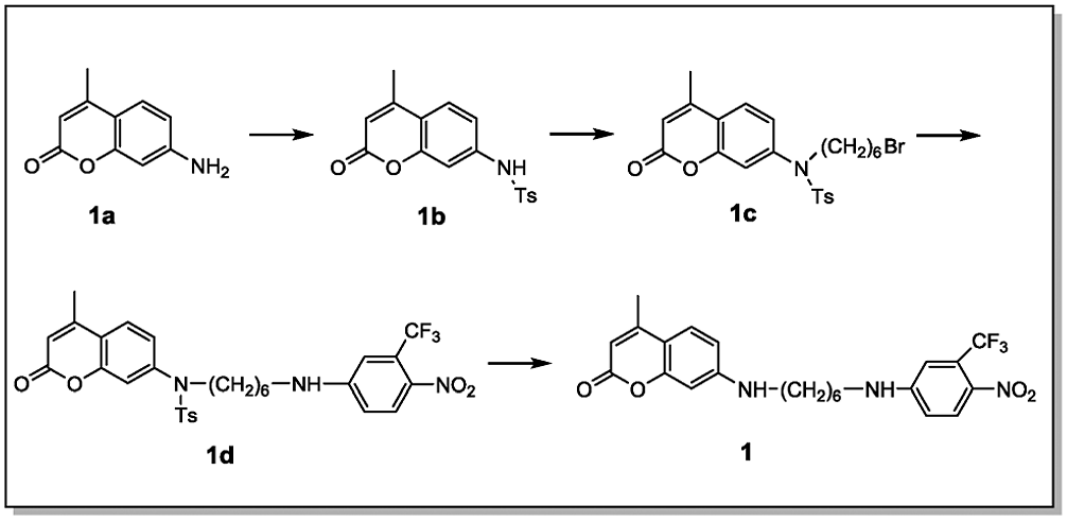

FIGURE 5.9: Reaction scheme

7-[6-Bromohexyl-(4-methanesulfonyl-phenyl)-amino]-4-methyl-coumarin (1c). Compound 1b (0.50 g, 1.52 mmol) was dissolved in CH_3CN (100 mL). Then Cs_2CO_3 (0.54 g, 2.28 mmol) and excess of 1,6-dibromohexane (3.7 g, 0.015 mol) were added to the solution under confined conditions, and the reaction was refluxed for 3 h. After filtration, the solution was evaporated and purified by means of silica gel column chromatography (EtOAc/hexane 1:2) to give a colourless solid 1c (0.72 g, 95% yield), Rf = 0.75 (EtOAc/hexane 1 : 2). ^{1}H NMR ($CDCl_3$, 500 MHz): d = 7.60 (d, J=8Hz,1H),7.47(d, J=8.5Hz,2H),7.28(d,J=8Hz,2H),7.26 (dd, J = 8.5, 2 Hz, 1H), 6.87 (d, J = 2 Hz, 1H), 6.30 (s, 1H), 3.56 (t, J = 6.5 Hz, 2H), 3.37 (t, J = 6.5 Hz, 2H), 2.45 (s, 3H), 2.44 (s, 3H), 1.80 (m, J=7Hz, 2H), 1.43(m, J=6.5Hz, 2H), 1.37(m, 4H).^{13}CNMR (500 MHz, $CDCl_3$): 160.2, 153.4, 151.8, 143.9, 142.2, 134.4, 129.6, 127.4, 125.2, 124.9, 119.1, 115.2, 115.1, 49.8, 33.6, 32.4, 27.7, 27.4, 25.4, 21.5, 18.6 ppm. 7-[Hexyl(4-nitro-3-(trifluoromethyl)phenyl)amine-(4-methane-sulfonyl-phenyl)-amino]-4-methylcoumarin (1d). A mixture of 1c (400 mg, 0.83 mmol), 4-nitro-3-(trifluoromethyl)aniline (172 mg, 0.83 mmol) and Cs_2CO_3 (407 mg, 1.25 mmol) was heated at reflux in acetonitrile overnight. The reaction mixture was allowed to cool to room temperature. After filtration, the solvent was removed under vacuum and the residue was purified by column chromatography (EtOAc/hexane 70:30) to afford compound 1d as a yellowish powder (0.36 g, 70% yield), Rf = 0.6 (EtOAc/hexane 1 : 2). ^{1}H-NMR ($CDCl_3$, 200 MHz): d = 8.03 (d, J=9Hz,1H), 7.59 (d, J=8.6Hz,1H),7.46 (d,J=8.4Hz, 2H), 7.28 (d, J = 8.4 Hz, 2H), 7.24 (dd J = 8.6, 2.2 Hz, 1H), 6.87 (d, J = 2.2 Hz, 2H), 6.66 (dd, J = 8.8, 2.8 Hz, 1H), 6.29 (d, J = 1.2 Hz, 1H), 4.86 (broad t, 1H), 3.57 (m, 2H), 3.23 (m, 2H), 2.43 (s, 6H), 1.64 (m, 2H), 1.41 (m, 6H). ^{13}C-NMR (500 MHz, $CDCl_3$): 160.3, 153.4, 152.0, 151.9, 144.1, 142.1, 135.8, 134.3, 129.7, 129.2, 127.3, 126.7, 124.9, 124.9, 119.1, 115.4, 115.1, 112.1, 104.9, 49.5, 42.8, 28.4, 27.4, 25.7, 25.4, 21.5, 18.5 ppm. 7-[Hexyl(4-nitro-3-(trifluoromethyl)phenyl)amine-amino]-4-methylcoumarin (1). Compound 1d (100 mg, 1.75 mmol) was added to concentrate sulfuric acid (5 mL) and the solution was stirred for 12 h at room temperature. The reaction mixture was cooled and carefully poured into water. The mixture was neutralized with saturated aqueous sodium bicarbonate and extracted with EtOAc three times. The organic solution was dried and evaporated to give 1 as a yellow

powder (0.76 g, 94%), Rf = 0.38 (EtOAc/hexane 1 : 2). ^{1}H-NMR ($CDCl_3$, 200 MHz):d=8.03 (d, J=9.2Hz,1H), 7.35 (d,J=8.6Hz, 1H), 6.87 (d, J=3Hz, 1H), 6.66 (dd, J=9,2.6Hz, 1H), 6.50 (dd, J= 8.6, 2.2 Hz, 1H), 6.42 (d, J = 2.2 Hz, 1H), 5.97 (s, 1H), 4.66 (broad t, 1H), 4.21 (broad s, 1H), 2.33 (s, 6H), 169–144 (m, 8H). ^{13}C-NMR (500 MHz, $CDCl_3$): 162.1, 155.9, 152.3, 151.9, 151.5, 135.9, 129.3, 126.9, 126.2, 124.9, 119.5, 112.1, 111.2, 110.3, 109.0, 97.64, 43.2, 28.9, 28.7, 26.6, 18.5 ppm.

5.4.3 Instrumentation

UV-Vis spectra were recorded using a JascoV-560 spectrophoto- meter using either quartz cells with a path length of 1 cm or a specific holder for thin films. Fluorescence emission spectra were recorded using a Spex Fluorolog-2 (mod. F-111) in air- equilibrated solutions either in right angle or in front face mode for solution or film samples, respectively. ^{1}H NMR and ^{13}C spectra were recorded on a VARIAN INOVA 200 spectrometer at room temperature at 200 MHz and 50 MHz, respectively, and calibrated using SiMe4 as an internal reference. Chemical shifts (d) are given in parts per million (ppm) and the coupling constants (J) in Hertz (Hz).

Irradiation conditions

Irradiation of the samples in solution was performed in a thermostated quartz cell (1 cm pathlength, 3 mL capacity) under gentle stirring, by using a continuum laser with λ_{exc} = 405 nm (ca. 3 W·cm^2) having a beam diameter of ca. 1.5 mm. Irradiation of the film samples was performed using a 150 W xenon lamp having a beam diameter of ca. 3.5 cm, mounting a cut-off filter at 400 nm.

Amperometric NO detection

NO release for samples in solution was measured using a World Precision Instrument, ISO-NO meter, equipped with a data acquisition system, and based on direct amperometric detection of NO with a short response time (<5 s) and a sensitivity range of 1 nM–20 mM.

The analog signal was digitalized using a four-channel record- ing system and transferred to a PC. The sensor was accurately calibrated by mixing standard solutions of $NaNO_2$ with 0.1 M H_2SO_4 and 0.1 M KI according to the reaction:

$$4H^+ + 2I^- + 2NO_2 \longrightarrow 2H_2O + 2NO + I_2$$

Irradiation was performed in a thermostated quartz cell (1 cm pathlength, 3 mL capacity) using the above continuum laser with λ_{exc} = 405 nm. NO measurements were carried out under stirring with the electrode positioned outside the light path in order to avoid NO signal artefacts due to photoelectric interference on the ISO-NO electrode.

5.4.4 Chemical detection of NO

NO release was also measured by means of the well-known, highly sensitive (detection limit on the order of the picomoles) fluorimetric bioassay of Misko et al.[42], based on the ring closure of the nonfluorescent 2,3-diaminonaphthalene (DAN) with nitrite to form the highly fluorescent product 2,3-diamino- naphthotriazole (DANT). Pieces of PLGA films (2 cm^2) were placed in a quartz cell (3 mL capacity) filled with water and were irradiated at different times or kept in the dark. Once photo- generated under aerobic conditions, NO, in the absence of other scavengers, is rapidly converted into nitrite and nitrate, its stable metabolites. Since only nitrite reacts quantitatively with DAN to give rise to DANT, the samples (1 mL) were incubated with nitrate reductase from Aspergillus niger and b-nicotinamide adenine dinucleotide phosphate in reduced form for 20 min at 37 1C, in order to convert nitrate to nitrite before addition of DAN. Afterwards 100 mL of 0.31 mM DAN in 0.62 M HCl were added and the solutions were stirred for 20 min at room temperature. After adding 100 mL of NaOH 2.8 M to the above solutions, the fluorescence emission and excitation spectra were recorded (Figure 5.6). A standard calibration curve was obtained by using freshly prepared solutions of sodium nitrite in phosphate buffer 10 mM at pH 7.4.

5.4.5 Film preparation

A polymer film integrating the compound 1 was prepared by the solvent casting method. Resomer®RG 855 (85 : 15 D,L-lactide : glycolide molar ratio, inherent viscosity 1.3–1.7 dL g^{-1} for 0.1% solution in chloroform at 25°C) from Boehringer Ingelheim (Germany) was used. Resomer®RG 855 (150 mg) and polyethylene glycol 400 Da (37 mg) as plasticizers were first dissolved in 5.9 mL of methylene chloride by overnight stirring. Thereafter, 100 mL of a solution of 1 in methylene chloride (7 mg·mL^{-1}) were added to the polymer solution. The mixture was then cast onto a Teflon®Petri dish (diameter 75 mm), covered with punctured Parafilm®and placed on a levelled surface under a hood for 24 h to allow solvent evaporation. The thickness and the weight of the films were measured using a digital micrometer and a digital balance (sensitivity = 0.01 mg), respectively. The film thickness was quite uniform across all the sample (0.050 $\pm$ 0.002 mm). The content of 1 in the film was 16 mg cm^2 . Distribution of 1 in the polymer film was evaluated by dividing the film into 8 slices, which were singularly weighed and dissolved in 5 mL of tetrahydrofuran. The amount of 1 was quantified by UV absorption at λ = 390 nm. A calibration curve in the range of 3–60 μg·mL^{-1} was constructed and the linearity of response was verified (r^2 = 0.995). The amount of 1 in the film was 3.38$\pm$0.018 μg·mg^{-1} film. Distribution of 1 in the polymer film was evaluated by dividing the film into 8 slices, which were singularly weighed and dissolved in 5 mL of tetrahydrofuran. The amount of 1 was quantified by UV absorption at λ = 400 nm. A calibration curve in the range of 3–60μg·mL^{-1} was constructed and the linearity of response was verified (r^2 = 0.995). The amount of 1 in the film was 3.38$\pm$0.018 μg·mg^{-1} film.

5.4.6 Antibacterial assay

One hundred mL of a bacterial suspension (50 000 CFU per mL) of *Escherichia coli* ATCC 25922 were placed into a 96-well microplate containing at the bottom the PLGA film (circular disk, diameter = 6 mm, each containing 4.5 mg of 1) and were irradiated for 5 and 20 min by using a 470 W Xe lamp equipped with a cut-off filter λ> 400 nm or kept in the

dark. Equal aliquots of the bacterial suspension were also placed into a 96-well microplate in the absence of the PLGA film and were irradiated under the same conditions. Afterwards, an aliquot of the bacterial suspension (20 μL) was placed on the sterile agar plate of MacConkey (Biokar diagnostics), where *Escherichia coli* grows with a typical pink color. The plates were incubated for 20 h at 37°C to allow bacterial growth.

Bibliography

[1] Taubes, G. The bacteria fight back. 2008.

[2] Cohen, M. L. *Nature* **2000**, *406*, 762–767.

[3] Laxminarayan, R. et al. *Lancet Infect Dis* **2013**, *13*, 1057–98.

[4] Pittet, D.; Allegranzi, B.; Storr, J.; Donaldson, L. *International Journal of Infectious Diseases* **2006**, *10*, 419–424.

[5] Page, K.; Wilson, M.; Parkin, I. P. *Journal of Materials Chemistry* **2009**, *19*, 3819–3831.

[6] Shlaes, D. M.; Sahm, D.; Opiela, C.; Spellberg, B. *Antimicrobial agents and chemotherapy* **2013**, *57*, 4605–4607.

[7] Schairer, D. O.; Chouake, J. S.; Nosanchuk, J. D.; Friedman, A. J. *Virulence* **2012**, *3*, 271–279.

[8] Fang, F. C. *Nitric oxide and infection*; Springer, 1999.

[9] Gardner, P. R.; Gardner, A. M.; Martin, L. A.; Salzman, A. L. *Proceedings of the National Academy of Sciences* **1998**, *95*, 10378–10383.

[10] Fang, F. C. *Nature reviews. Microbiology* **2004**, *2*, 820.

[11] Ignarro, L. J. *Nitric oxide: biology and pathobiology*; Academic press, 2000.

[12] Wang, P. G.; Xian, M.; Tang, X.; Wu, X.; Wen, Z.; Cai, T.; Janczuk, A. J. *Chemical reviews* **2002**, *102*, 1091–1134.

[13] Wang, P. G.; Cai, T. B.; Taniguchi, N. *Nitric oxide donors: for pharmaceutical and biological applications*; John Wiley & Sons, 2005.

[14] Riccio, D. A.; Schoenfisch, M. H. *Chemical Society Reviews* **2012**, *41*, 3731–3741.

[15] Seabra, A. B.; Durán, N. *Journal of Materials Chemistry* **2010**, *20*, 1624–1637.

[16] M Halpenny, G.; K Mascharak, P. *Anti-Infective Agents in Medicinal Chemistry (Formerly Current Medicinal Chemistry-Anti-Infective Agents)* **2010**, *9*, 187–197.

[17] Sortino, S. *Chemical Society Reviews* **2010**, *39*, 2903–2913.

[18] Sortino, S. *Journal of Materials Chemistry* **2012**, *22*, 301–318.

[19] Ford, P. C. *Nitric oxide* **2013**, *34*, 56–64.

[20] Fry, N. L.; Mascharak, P. K. *Accounts of chemical research* **2011**, *44*, 289–298.

[21] Joslin, J.; Neufeld, B.; Reynolds, M. M. *RSC Advances* **2014**, *4*, 42039–42043.

[22] Roveda, A. C.; de Fazio Aguiar, H.; Miranda, K. M.; Tadini, C. C.; Franco, D. W. *Journal of Materials Chemistry B* **2014**, *2*, 7232–7242.

[23] Dolanský, J.; Henke, P.; Kubát, P.; Fraix, A.; Sortino, S.; Mosinger, J. *ACS Appl Mater Interfaces* **2015**, *7*, 22980–9.

[24] Mosinger, J.; Lang, K.; Kubát, P. *Top Curr Chem* **2016**, *370*, 135–68.

[25] Bishop, A.; Anderson, J. E. *Toxicology* **2005**, *208*, 193–205.

[26] Veldhuyzen, W. F.; Nguyen, Q.; McMaster, G.; Lawrence, D. S. *J Am Chem Soc* **2003**, *125*, 13358–9.

[27] Pellois, J.-P.; Hahn, M. E.; Muir, T. W. *J Am Chem Soc* **2004**, *126*, 7170–1.

[28] Weinstain, R.; Segal, E.; Satchi-Fainaro, R.; Shabat, D. *Chem Commun (Camb)* **2010**, *46*, 553–5.

[29] Fry, N. L.; Wei, J.; Mascharak, P. K. *Inorg Chem* **2011**, *50*, 9045–52.

[30] Zheng, Q.; Bonoiu, A.; Ohulchanskyy, T. Y.; He, G. S.; Prasad, P. N. *Mol Pharm* **2008**, *5*, 389–98.

[31] Vittorino, E.; Sciortino, M. T.; Siracusano, G.; Sortino, S. *ChemMedChem* **2011**, *6*, 1551–4, 1534.

[32] Kirejev, V.; Kandoth, N.; Gref, R.; Ericson, M. B.; Sortino, S. *Journal of Materials Chemistry B* **2014**, *2*, 1190–1195.

[33] Fraix, A.; Sortino, S. *Chem Asian J* **2015**, *10*, 1116–25.

[34] Fraix, A.; Marino, N.; Sortino, S. *Top Curr Chem* **2016**, *370*, 225–57.

[35] Caruso, E. B.; Petralia, S.; Conoci, S.; Giuffrida, S.; Sortino, S. *Journal of the American Chemical Society* **2007**, *129*, 480–481.

[36] Conoci, S.; Petralia, S.; Sortino, S. Use of nitroaniline derivatives for the production of nitric oxide. 2014; US Patent 8,766,006.

[37] Callari, F. L.; Sortino, S. *Chemical Communications* **2008**, 1971–1973.

[38] Cai, W.; Wu, J.; Xi, C.; Meyerhoff, M. E. *Biomaterials* **2012**, *33*, 7933–44.

[39] Brisbois, E. J.; Bayliss, J.; Wu, J.; Major, T. C.; Xi, C.; Wang, S. C.; Bartlett, R. H.; Handa, H.; Meyerhoff, M. E. *Acta biomaterialia* **2014**, *10*, 4136–4142.

[40] Møller, J. K. S.; Skibsted, L. H. *Chem Rev* **2002**, *102*, 1167–78.

[41] Lin, Q.; Bao, C.; Fan, G.; Cheng, S.; Liu, H.; Liu, Z.; Zhu, L. *Journal of Materials Chemistry* **2012**, *22*, 6680–6688.

[42] Misko, T. P.; Schilling, R.; Salvemini, D.; Moore, W.; Currie, M. *Analytical biochemistry* **1993**, *214*, 11–16.

Chapter 6

β-CD derivates

A Multifunctional β-Cyclodextrin-Conjugate Photodelivering Nitric Oxide with Fluorescence Reporting

Published as:

Authors: Gabor Benkovics, Marta Perez-Lloret, Damien Afonso, Andras Darcsi, Szabolcs Beni, Eva Fenyvesi, Milo Malanga and Salvatore Sortino.

Journal: International Journal of Pharmaceutics, 2017.

6.1 Introduction

Cyclodextrins (CDs) have been greatly developed during the last thirty years as carriers of "conventional" drugs[1,2]. However, the use of CDs as suitable vehicles for photoactivable therapeutic compounds has been only recently object of attention[3]. Due to their hydrophobic cavity, natural CDs can host a variety of photosensitive agents by supramolecular interactions[4,5]. Nevertheless, in most cases, the low binding constants between unmodified CDs and guest molecules represent a major drawback of these systems as biocarriers, making the modification of the CD structure strictly necessary in view of actual applications[6]. Modification of the CDs molecular scaffold through functionalization of the primary and/or secondary hydroxyl groups with suitable photoresponsive units allows to obtain multifunctional nanocarriers with intriguing properties whilst, at the same time, maintaining the macrocycle's capacity for guests encapsulation[7,8,9]. Nitric oxide (NO) is a pleiotropic bioregulator of important physiological and pathophysiological processes encompassing neurotransmission, vasodilatation and hormone secretion in living bodies[10]. Besides, NO is an excellent sacrificial antioxidant, anticancer and antibacterial agent[11]. This scenario has open a fervent research activity devoted to developing compounds able to release NO under physiological conditions as potential pharmaceuticals to fight a variety of diseases[12,13,14,15]. However, the biological effects of NO are strictly depending on its concentration, location and dose[16]. This has made the light-activated NO donors very appealing due to the superb spatiotemporal accuracy the light triggering offers[17,18,19]. Several NO photodonors (NOPD) have been supramolecularly combined with CDs derivatives[20]. In contrast, only limited examples of NO, photodonor covalent conjugates with CDs are reported to date[21]. Quantification of the NO delivery in real time is another important issue to be faced, especially when the main interest is to reach a critical molecule concentration to induce a specific effect. A suitable way to address this quantification task is based on the use of a fluorescent reporter. This elegant strategy relies on the simultaneous photorelease of the desired bioactive species, i.e. NO, and a fluorescent component (the reporter) from the same nonfluorescent

precursor[22 23 24]. The release process can be thus easily quantified by monitoring the fluorescence emission of the reporter, which acts exactly as an optical counter of the bioactive species. Recently, we have reported interesting properties of an ad-hoc designed molecular conjugate integrating two chromogenic centers within the same covalent skeleton[25 26], an anthracene moiety and a nitroaniline derivative, this latter as a suitable NOPD[27]. In this compound, the typical emission of the anthracene fluorophore is completely suppressed by a photoinduced energy transfer to the nitroaniline moiety. We demonstrated that the photorelease of NO leads to the revival of the fluorescence of anthracene fluorophore which acts as a fluorescent reporter for the NO delivery in living cells[25 26].

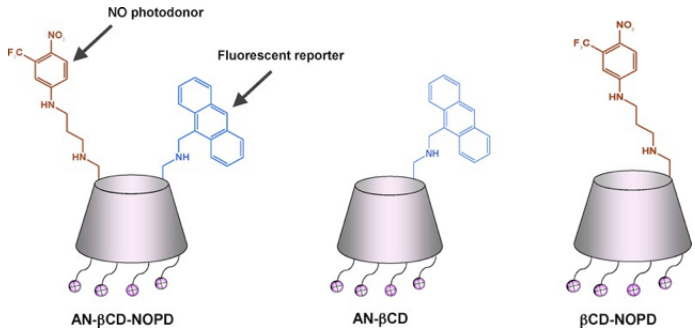

FIGURE 6.1: Structure of β-CD-Ant-NOPD, Ant-β-CD and β-CD-NOPD

Based on the above scenario we considered it of value to translate this NO photorelease with fluorescent reporting concept in a novel conjugate, which covalently integrates the NO photoreleaser and the anthracene moiety within the same positively charged β-CD scaffold. This contribution reports the synthesis, characterization and photochemical properties of the cationic β-CD conjugate AN-β-CD-NOPD and the suitable model compounds AN-β-CD and β-CD-NOPD (Figure 6.1).

6.2 Experimental section

6.2.1 Chemicals

6-Monodeoxy-6-monoazido-β-CD and 6-monotosyl-β-CD are fine chemical products of CycloLab, 1,3- diaminopropanol ($\geq$ 99%), 4-nitro-3- (trifluoromethyl)aniline (98%), glycidyltrimethylammonium chloride (technical grade, $\geq$ 90%), sodium azide (ReagentPlus®, $\geq$ 99.5%), hydrazine monohydrate (reagent grade, 98%), sodium borohydride ($\geq$ 98.0%), anthracene-9-carboxaldehyde ($\geq$ 97.0%), p-toluenesulfonyl chloride (ReagentPlus®, $\geq$ 99%), trimethylamine ($\geq$ 99%), 1,3-propanedithiol ($\geq$ 99%), palladium on carbon (5%), were sourced from Sigma-Aldrich. Dimethyl sulfoxide, formic acid, methanol, pyridine were obtained from Molar Chemicals.

6.2.2 Instrumentation

^{1}H-, ^{13}C- NMR spectra and DEPT-ed-HSQC spectra were recorded in DMSO-d_6 or D_2O (10 mg dissolved in 0.8 mL of deuterated solvent) on a Varian DDR-600 at 600 MHz spectrometer at 298 K. Mass spectra were obtained on Bruker ESQUIRE 3000 ES-ion trap instrument with electrospray ionization (ESI) in negative mode. All samples were dissolved in water.

Preparative chromatographic separations were performed on a Buchi preparative chromatography system using SiliCycle Silica Cartridge (4 cm x 15 cm) packed with Lichroprep (120 g) RP-18 Phase (40-63 μm) as a stationary phase and water-methanol gradient elution. The chromatographic station was equipped with Buchi UV Photometer C-635 as a detector (detection wavelength set at 390 nm for NOPD appended derivatives and at 245 nm for the tosylated intermediate). UV–vis absorption and fluorescence spectra were recorded with a Jasco V 650 spectrophotometer and a Fluorolog-2 (Model, F111) spectrofluorimeter, respectively. Fluorescence lifetimes were recorded with the same spectrofluorimeter equipped with a TCSPC Triple Illuminator. The samples were irradiated by a pulsed diode excitation source Nanoled at 370 nm. The kinetic was monitored at 420 nm and each solution itself

was used to register the prompt at 370 nm. The system allowed measurement of fluorescence lifetimes from 200 ps. The multiexponential fit of the fluorescence decay was obtained using the following equations:

$$I(t) = A_1 exp^{(t/\tau_1)} + A_2 exp^{(t/\tau_2)}$$

$$I(t) = A_1 exp^{(t/\tau_1)} + A_2 exp^{(t/\tau_2)} + A_3 exp^{(t/\tau_3)}$$

Multiexponential fitting were used because they gave much better chi-square values than monoexponential fitting. $^1O_2$ emission was registered with the same spectrofluorimeter as above equipped with a NIR-sensitive liquid nitrogen cooled photomultiplier, exciting the air-equilibrated samples in D_2O solution at 380 nm with the fluorimeter lamp. Photolysis of the samples in solution was performed in a thermostated quartz cell (1 cm pathlength, 3 mL capacity) under gentle stirring, by using a continuum laser with λ_{exc} = 405 nm (ca. 100 mW) having a beam diameter of ca. 1,5 mm.

NO release was measured with a World Precision Instrument, ISO-NO meter, equipped with a data acquisition system, and based on direct amperometric detection of NO with short response time (<5 s) and sensitivity range 1 nM–20 μM. The analog signal was digitalized with a four-channel recording system and transferred to a PC. The sensor was accurately calibrated by mixing standard solutions of $NaNO_2$ with 0,1 M H_2SO_4 and 0,1 M KI according to the reaction:

$$4H^+ + 2I^- + 2NO_2 \longrightarrow 2H_2O + 2NO + I_2$$

Irradiation was performed in a thermostated quartz cell (1 cm path length, 3 mL capacity) under gentle stirring by using the same 405 nm laser sources described above. NO measurements were carried out with the electrode positioned outside the light path in order to avoid false NO signal due to photoelectric interference on the ISO-NO electrode.

6.3 Results and discussion

6.3.1 Syntheses

The model compound AN-β-CD was synthesized according to the procedure illustrated in Figure 6.2 and briefly described in the following (the full details are reported in the Supporting Information).

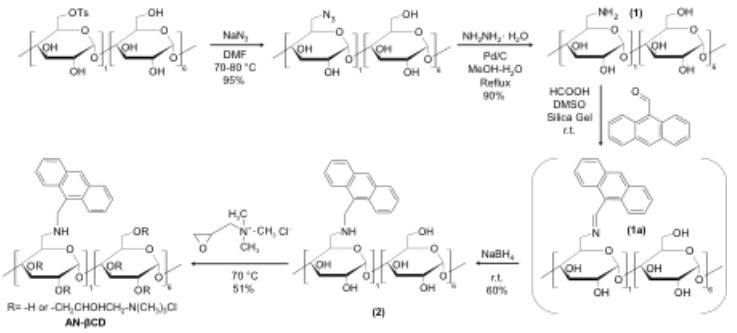

FIGURE 6.2: Reaction scheme for the synthesis of AN-β-CD

6-monotosyl-β-CD was promptly converted to the amino-analogue 1 by exhaustive reduction of the intermediate 6-monodeoxy-6-monoazido β-CD, according to literature[28]. The amino group, located on the primary rim of CD scaffold, is a suitable anchoring point for the introduction of the anthracene chromophore. As compound 1 is obtained as free base, the coupling could be achieved by a nucleophilic substitution in DMF with the commercially available 9-(chloromethyl)anthracene. This reaction setting was explored, but the conversion rate was not satisfactory (∼30% formation of compound 2) and N-dialkylated product (CD scaffold containing two anthracene moieties) was considerably formed under the tested experimental conditions (∼10%). Although chromatographic purification of the crude can be attempted, the procedure is time- consuming, not effective and resulted in low-yield. As efficient alternative for the preparation of compound (2) a two-steps one-pot reaction based on imine-reduction, allowing good conversion rate and avoiding chromatographic purification, was applied. The addition of silica gel to the reaction mixture during the first step was a fundamental requirement for achieving quantitative conversion to the

imine intermediate 1a. The nano-porous material was effective in removing the water accumulated during the condensation process thus making convenient the coupling reaction. The second step based on the mild reducing agent sodium borohydride proceeded quantitatively within expectations. The introduction of the permanent charges on the CD scaffolds was achieved by using the alkylating agent, glycidyltrimethylammonium chloride, as reaction solvent. This approach has the advantages of minimizing the by-products formation and reducing the work-up to simple fractional crystallization cycles.

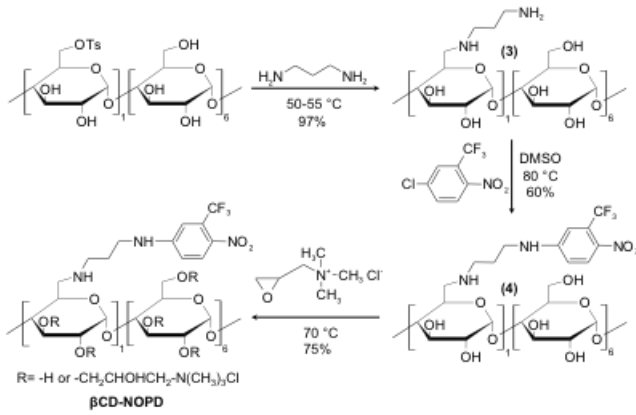

FIGURE 6.3: Reaction scheme for the synthesis of β-CD-NOPD

The model compound β-CD-NOPD was synthesized according to the procedure illustrated in Figure 6.3 and briefly described in the following (the full details are reported in the Supporting Information). The flexible linker, 1,3-diaminopropane, was effectively introduced on the CD scaffold by nucleophilic substitution on the 6-monotosyl-β-CD. In order to reduce the formation of by-products such as CD dimers (two or more CD units connected through the linker) and 3,6-anhydro derivatives, 1,3- diaminopropane was used in large excess (reaction solvent) and 6-monotosyl-β-CD was added portion- wise to the warm solvent solution. These precautions ensured that 6-monotosyl-β-CD was always acting as limiting reagent and promptly converted to 6-monodeoxy-6-mono-(3-aminopropylamino) β-CD. The large excess of 1,3-diaminopropane in combination with an adequate work-up (evaporation under reduced pressure and precipitation with methanol-diisopropyl ether

mixture) also maintained compound 3 in free base form. This is a strict requirement to successfully accomplish the following reaction step as no extra base can be added to the reaction mixture due to the high reactivity of 4-chloro-1-nitro-2-(trifluoromethyl)benzene towards these species. It is worth to mention that the decision of attaching the NOPD moiety to the CD scaffold through a linker, was the result of several unsuccessful attempts to directly introduce the chromophore on the CD rim. No adequate reaction conditions were found to react the reagent 4-chloro-1-nitro-2-(trifluoromethyl)benzene with the free base of 6-monoamino-6-monodeoxy-β-CD. The most probable reason is that the nitrobenzene derivative formed a strong inclusion complex with the β-CD cavity locating the chlorine atom on the secondary side[29]. The establishment of this supramolecular interaction precludes primary-side substitution. Compound 4 was obtained in moderate yield by reacting the free base of compound 3 with 4-chloro-1- nitro-2-(trifluoromethyl)benzene. As no extra base could be added to the reaction mixture without consuming the chromophore, the product was formed only at around 40% conversion rate. Reversed- phase chromatographic purification was needed to separate the unreacted compound 3 from the target product. The solubility profile of compound 4 was improved by modifying some of the hydroxyl groups with permanently charged side-chains.

The multifunctional conjugate AN-β-CD-NOPD was synthesized according to the procedure illustrated in Figure 6.4 and briefly described in the following (the full details are reported in the Supporting Information). In order to introduce both the chromophores on the primary side of the CD scaffold, tosylation of 6-monoazido-6-monodeoxy-β-CD was performed in pyridine. This approach is selective for the modification of the primary rim of the macrocycle[30] and generates a mixture of three pairs of pseudoenantiomers (6A-monodeoxy-6A-monoazido-6X-monotosyl-β-CD, compound 5). The mixture of primary-side heterodisubstituted β-CD was isolated by preparative reversed-phase chromatography. The strategy developed for the introduction of the NOPD chromophore in model compound β-CD-NOPD was applied at this stage almost without modifications. The azido moiety remained unaltered both in harsh alkaline conditions (preparation of compound 6) and during the

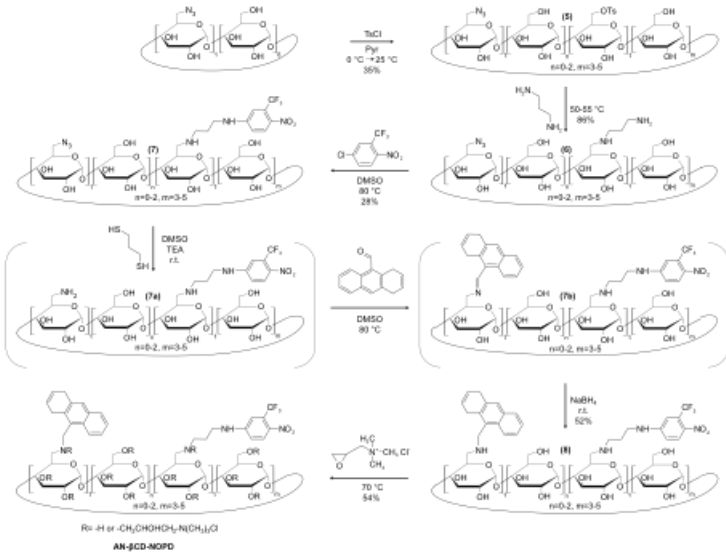

FIGURE 6.4: Reaction scheme for the synthesis of AN-β-CD-NOPD.

prolonged heating required for the nitrobenzene installation (preparation of compound 7). The most challenging part of the synthetic work was the introduction of the anthracene fluorophore on the NOPD-appended CD. A three-step one-pot reaction was carefully designed to fulfill all the necessary requirements. First, a mild reduction method was chosen for the selective reduction of azido group in the presence of the aromatic nitro group. This approach was based on the use of 1,3-propanedithiol and trimethylamine as reduction mixture to obtain the amino-intermediate 7a. Addition of anthracene-9-carboxaldehyde and heating of the reaction mixture resulted in almost complete conversion (90% conversion rate based on TLC estimation) to anthracene-appended imine-intermediate 7b. Portion-wise addition of $NaBH_4$ and prolonged stirring at room temperature afforded anthracene-appended amine-intermediate, compound 8, in quantitative conversion. Preparative reversed-phase chromatographic purification allowed the removal of the unreacted compound 7a and the isolation of targeted compound 8. As the CD scaffold is modified simultaneously with two aromatic units, its solubility in aqueous environment is limited. This drawback was overcome by introducing quaternary ammonium bearing moieties in the system, obtaining the desired compound AN-β-CD-NOPD.

6.3.2 Syntheses

All compounds synthesized are well soluble in aqueous medium due to the presence of the cationic termination mainly located at the secondary rim of the β-CD scaffold. The absorption spectrum of AN- β-CD-NOPD (a in Figure 6.1A) exhibits the distinctive spectral features of the anthracene chromophore below 400 nm and an intense absorption at longer wavelengths extending beyond 450 nm, due to the contribution of the nitroaniline moiety. This spectrum reflects quite well the sum absorption spectrum of the independent model compound AN-β-CD and β-CD-NOPD (b and c in Figure 6.5A), ruling out any significant interaction between the anthracene and nitroaniline chromophores in the ground state. On the other hand, the intense fluorescence emission of the anthracene fluorophore observed in the case of AN-β-CD (d in Figure 6.5) is significantly quenched in the bichromophoric conjugate AN-β-CD-NOPD (e in Figure 6.5B), suggesting a remarkable interaction between the two chromophores in the excited state. According to what already demonstrated in our previous studies[31 26], this drastic fluorescence quenching can be explained on the basis of a photoinduced energy transfer between the anthracene fluorophore and the nitroaniline components in the conjugate, which is encouraged by the close proximity of the donor and acceptor, both linked at the same rim.

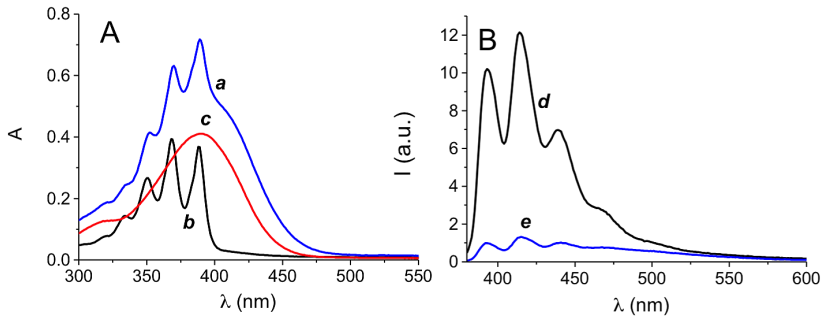

FIGURE 6.5: (A) Absorption spectra of 40 μM aqueous solution AN-β-CD-NOPD (a) and the model compounds AN-β-CD (b) and β-CD-NOPD (c). (B) Fluorescence emission spectra (λ_{exc} = 370 nm) of the model compound AN-β-CD (d) and AN-β-CD-NOPD (e)

The capability of AN-β-CD-NOPD to deliver NO under light stimuli was investigated

by the direct and real-time monitoring of this transient species using an ultrasensitive NO electrode which directly reveals NO with nM concentration sensitivity by an amperometric technique[32]. The absorption spectral features of AN-β-CD-NOPD allow the selective excitation of the NO photoreleaser component of the conjugate at λ_{exc} > 400 nm. The results illustrated in Figure 6.6 provide unambiguous evidence that the bichromophoric CD conjugate is very is stable in the dark but supplies NO upon illumination with λ_{exc} = 405 nm. Note that, the rate of photorelease is very similar to that observed for an optically matched solution of the model compound β-CD-NOPD.

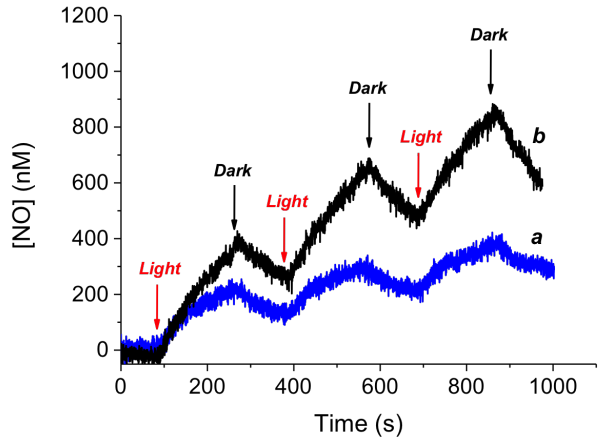

FIGURE 6.6: NO release profile observed for optically matched aqueous solutions of AN-β-CD-NOPD (a) and β-CD-NOPD (b) upon irradiation with λ_{exc} = 405 nm at 25°C.

NO photorelease from AN-β-CD-NOPD is accompanied by dramatic revival of the characteristic emission arising from the anthracene fluorophore. Figure 6.7A shows the fluorescence emission spectra observed at regular irradiation times with visible light up to 45 min. This fluorescence restoring is due to the formation of a reaction product formed after the loss of NO that, in contrast to the nitroaniline derivative, is not a good energy acceptor and thus is not able to quench the fluorescence of the anthracene fluorophore. This behavior also reflects in the dynamic of the emission. As shown in the inset in Figure 6.7A, the fluorescence decay of AN-β-CD-NOPD (trace a) was shorter than that of the model compound

AN-β-CD (trace b). However, after 45 min irradiation of the AN-β-CD-NOPD solution, the fluorescence dynamic become slower (trace c), according to the revival of the fluorescence. In such a way, the anthracene unit represents an excellent optical reporter for the NO release. In fact, as illustrated in Figure 6.7 B, we found an excellent linear correlation between the concentration of NO photogenerated and the increase of the fluorescence intensity of the optical reporter.

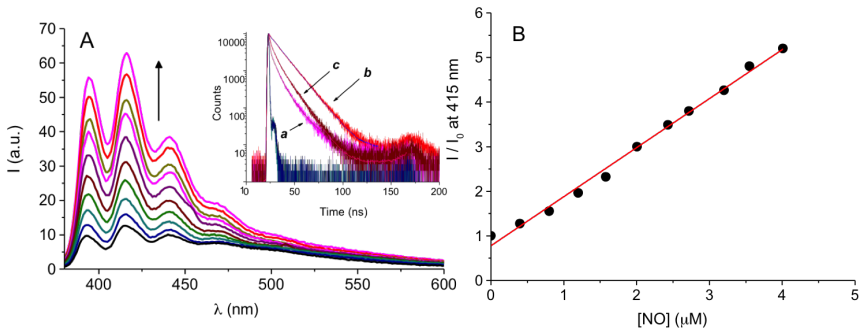

FIGURE 6.7: (A) Fluorescence (λ_{exc} = 370 nm) spectral changes observed upon irradiation of an aqueous solution of AN-β-CD-NOPD (40 μM) at regular irradiation times of 5 min (from bottom to top) with visible light (λ_{exc} = 405 nm). The inset shows the fluorescence decay and the related multiexponential fitting for solutions of AN-β-CD-NOPD (a), the model compound AN-β-CD (b) and AN-β-CD-NOPD after 45 min irradiation with visible light (c); λ_{exc} = 370 nm; λ_{em} = 420 nm. (B) Correlation of the fluorescence increase observed in Figure 6.7A and the concentration of NO released from the same solution (I and I0 represent the fluorescence intensities at 420 nm after each irradiation time and that of the non-irradiated solution, respectively).

Note that, the suppression of the quenching of the excited state of anthracene after NO release reflects also in the capability of this component to photosensitize the formation of singlet oxygen ($^1O_2$), the key species in photodynamic therapy of cancer and bacterial diseases[33]. This was directly demonstrated by direct detection through monitoring of the typical phosphorescence of $^1O_2$ in the near-IR spectral window[34]. Figure 6.8 shows that excitation of AN-β-CD-NOPD at λ_{exc}= 370 nm does not lead to any detectable formation of $^1O_2$, according to effective quenching occur- ring of the anthracene by the nitroaniline

component. On the other hand, excitation at the same wavelength after irradiating the AN-β-CD-NOPD solution for 1 h at 405 nm, leads to the appearance of the of the characteristic luminescence signals of $^1O_2$ with maximum at ca. 1270 (Figure 6.8).

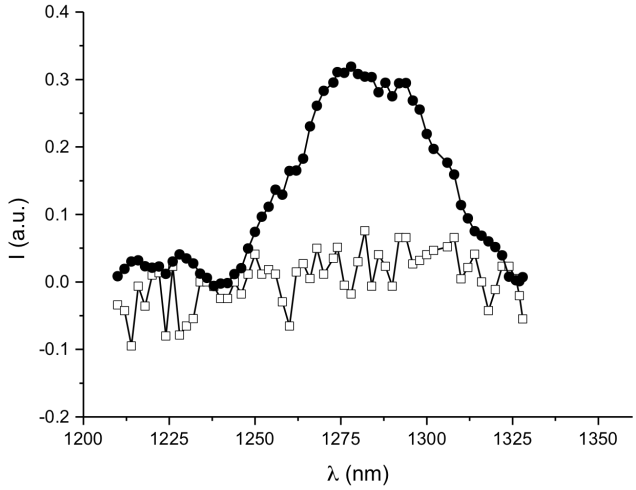

FIGURE 6.8: Luminescence spectra detected upon 370 nm light excitation of a D_2O solutions of AN-β-CD- NOPD (40 μM) before (□) and after (•) 1 h irradiation at λ_{exc} = 405 nm.

Despite the covalent linking with the two chromophores, the CD cavity of AN-β-CD-NOPD is still able to accommodate hydrophobic guests. This was proven by using naphthalene as a model compound, which is insoluble in water medium. To this end, a methanol solution of naphthalene was prepared. After drying the solvent, the resulting dried sample was added of an aqueous solution of AN-β-CD- NOPD and the sample was stirred for 1 h at room temperature. The mixture was then filtered and analysed by UV-Vis absorption. Figure 6.9 shows the spectroscopic properties of AN-β-CD-NOPD before the addition to the film sample (a) and after the filtration procedure (b). The presence of the typical structured absorption bands of the naphthalene at ca. 275 and 285 nm (b) provides unambiguous evidence for the encapsulation of the guests within the CD cavity. Besides, the characteristic fluorescence emission of naphthalene (c in Figure 6.9) further confirms the effective formation of the host- guest supramolecular complex.

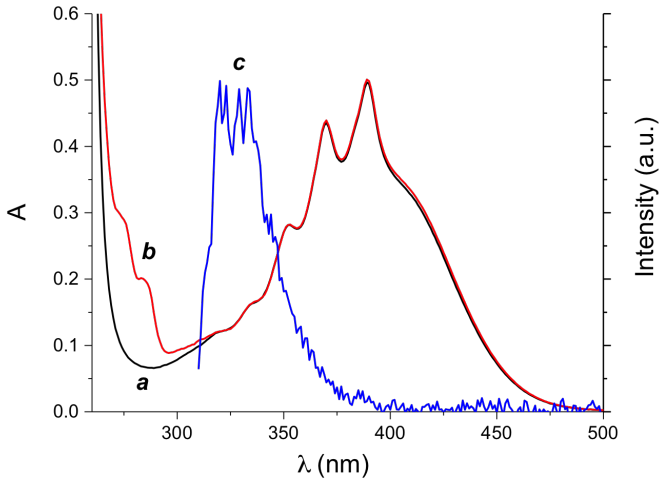

FIGURE 6.9: Absorption spectra of an aqueous solution of AN-β-CD-NOPD (30 μM) (a) and its complex with naphthalene (b) (left Y-axis). Fluorescence emission spectrum (c) observed upon excitation at λ_{exc} = 280 nm of the sample b (right Y-axis).

6.4 Conclusions

We have devised and synthesized a novel multifunctional CD conjugate, bearing a nitroaniline and an anthracene chromophoric unit, able to incorporate a number of functionalities within the same molecular skeleton. AN-β-CD-NOPD is well soluble in water due to the cationic appendages present at the lower rim of the CD scaffold and is able to deliver NO under the exclusive control of visible light stimuli. NO photorelease restores the fluorescence of the anthracene fluorophore, which acts as an optical reporter of NO concentration. To the best of our knowledge, this represents the first example of NO photodispenser with fluorescence reporting integrated in a CD scaffold. Furthermore, we have demonstrated that the anthracene component is also capable to photogenerate $^1O_2$ sequentially to the NO release. The AN-β-CD-NOPD conjugate is also able to accommodate hydrophobic guests within the β-CD cavity, as proven by using naphthalene as a model compound. In view of the key role NO and 1O2 plays in photodynamic therapy, this β-CD derivative represents an intriguing candidate for biopharmaceutical research. Studies in this direction are currently underway in our laboratories.

Bibliography

[1] Davis, M. E.; Brewster, M. E. *Nat Rev Drug Discov* **2004**, *3*, 1023–35.

[2] Loftsson, T.; Duchêne, D. *Int J Pharm* **2007**, *329*, 1–11.

[3] Mazzaglia, A.; Sciortino, M.; Kandoth, N.; Sortino, S. *Journal of Drug Delivery Science and Technology* **2012**, *22*, 235–242.

[4] Bortolus, P.; Monti, S. *Advances in photochemistry* **1996**, *21*, 1–134.

[5] Monti, S.; Sortino, S. *Chem Soc Rev* **2002**, *31*, 287–300.

[6] Mazzaglia, A.; Micali, N.; Scolaro, L. M. *Cyclodextrins Materials: Photochemistry, Photophysics and Photobiology, Elsevier, Amsterdam* **2006**, 203–222.

[7] Mourtzis, N.; Paravatou, M.; Mavridis, I. M.; Roberts, M. L.; Yannakopoulou, K. *Chemistry* **2008**, *14*, 4188–200.

[8] Mourtzis, N.; Eliadou, K.; Aggelidou, C.; Sophianopoulou, V.; Mavridis, I. M.; Yannakopoulou, K. *Org Biomol Chem* **2007**, *5*, 125–31.

[9] Yannakopoulou, K.; Jicsinszky, L.; Aggelidou, C.; Mourtzis, N.; Robinson, T. M.; Yohannes, A.; Nestorovich, E. M.; Bezrukov, S. M.; Karginov, V. A. *Antimicrob Agents Chemother* **2011**, *55*, 3594–7.

[10] Ignarro, L. J. *Nitric oxide: biology and pathobiology*; Academic press, 2000.

[11] Ignarro, L. J. *Arch Pharm Res* **2009**, *32*, 1099–101.

[12] Wang, P. G.; Cai, T. B.; Taniguchi, N. *Nitric oxide donors: for pharmaceutical and biological applications*; John Wiley & Sons, 2005.

[13] Wang, P. G.; Xian, M.; Tang, X.; Wu, X.; Wen, Z.; Cai, T.; Janczuk, A. J. *Chemical reviews* **2002**, *102*, 1091–1134.

[14] Riccio, D. A.; Schoenfisch, M. H. *Chemical Society Reviews* **2012**, *41*, 3731–3741.

[15] Seabra, A. B.; Durán, N. *Journal of Materials Chemistry* **2010**, *20*, 1624–1637.

[16] Janczuk, A. J.; Jia, Q.; Xian, M.; Wen, Z.; Wang, P. G.; Cai, T. *Expert Opinion on Therapeutic Patents* **2002**, *12*, 819–826.

[17] Ford, P. C. *Accounts of chemical research* **2008**, *41*, 190–200.

[18] Fry, N. L.; Mascharak, P. K. *Accounts of chemical research* **2011**, *44*, 289–298.

[19] Ford, P. C. *Nitric oxide* **2013**, *34*, 56–64.

[20] Fraix, A.; Marino, N.; Sortino, S. *Top Curr Chem* **2016**, *370*, 225–57.

[21] Piras, L.; Theodossiou, T. A.; Manouilidou, M. D.; Lazarou, Y. G.; Sortino, S.; Yannakopoulou, K. *Chem Asian J* **2013**, *8*, 2768–78.

[22] Veldhuyzen, W. F.; Nguyen, Q.; McMaster, G.; Lawrence, D. S. *J Am Chem Soc* **2003**, *125*, 13358–9.

[23] Pellois, J.-P.; Hahn, M. E.; Muir, T. W. *J Am Chem Soc* **2004**, *126*, 7170–1.

[24] Weinstain, R.; Segal, E.; Satchi-Fainaro, R.; Shabat, D. *Chem Commun (Camb)* **2010**, *46*, 553–5.

[25] Vittorino, E.; Sciortino, M. T.; Siracusano, G.; Sortino, S. *ChemMedChem* **2011**, *6*, 1551–1554.

[26] Kirejev, V.; Kandoth, N.; Gref, R.; Ericson, M. B.; Sortino, S. *Journal of Materials Chemistry B* **2014**, *2*, 1190–1195.

[27] Caruso, E. B.; Petralia, S.; Conoci, S.; Giuffrida, S.; Sortino, S. *Journal of the American Chemical Society* **2007**, *129*, 480–481.

[28] Jicsinszky, L.; Iványi, R. *Carbohydrate polymers* **2001**, *45*, 139–145.

[29] Ueno, A.; Breslow, R. *Tetrahedron Letters* **1982**, *23*, 3451–3454.

[30] Matsui, Y.; Yokoi, T.; Mochida, K. *Chemistry Letters* **1976**, *5*, 1037–1040.

[31] Vittorino, E.; Sciortino, M. T.; Siracusano, G.; Sortino, S. *ChemMedChem* **2011**, *6*, 1551–4, 1534.

[32] Coneski, P. N.; Schoenfisch, M. H. *Chem Soc Rev* **2012**, *41*, 3753–8.

[33] Hasan, T.; Moor, A. C. E.; Ortel, B. *Inc.: Hamilton, Ontario, Canada* **2000**,

[34] Wilkinson, F.; Helman, W. P.; Ross, A. B. *Journal of physical and chemical reference data* **1993**, *22*, 113–262.

Chapter 7

General Conclusions

In this thesis, we successfully integrated photoactivable molecules with different materials. Light has been demonstrated to be a perfect trigger for the production of cytotoxic species. The proofs of its good spatiotemporal release only under light stimulation are numerous. In addition, we succeed by creating fluorescent reporting systems for NO release, and this one show good antibacterial activity. The increase of temperature thanks to light excitation was positive too, and we are expecting for the results of its effects on bacteria damage. We are aware that this is just a first step in the fight of MDR, but the results we obtained are promising, and elegible for further studies in some cases. Other examples not presented in this thesis are under studies at the moment, hoping to find an appropriate platform able to integrate as many therapies as possible.

Acknowledgements

I want to deeply thanks my research supervisor Prof. Salvatore Sortino for giving me the chance of doing my PhD in his group. Thanks also to Prof. Guido De Guidi for his advices and hosting us. Without their help, this would never happened.

Deep thanks to the entire Cyclon-Hit network, ITN Marie Curie Program. I feel so grateful to Dr. R. Gref for her efforts in making this possible. Thanks to all the partners who allowed me to work with their samples: Again, Dr. R. Gref, CNRS Université Sud de Paris; Prof. A. Vargas-Berenguel, Universidad de Almería; Prof. A. Feiler, Nanologica and Dr. Eva Fenyvesi, Cyclolab. Special mention to the last one and Dr. M. Malanga for hosting and teaching me during two intense weeks. Thanks and good luck to my fellows with their career and future projects, specially to those who acquired the biggest responsibility ever, parenthood. I want also express my gratitude to Dr. S. Conoci and Dr. S. Petralia, from STMicroelectronics, not just for measurements, also for listen and advising me. I own you several beers, Salvuccio. Thanks to Dr. A. R. Blanco from SIFI S.p.A and Dr. F. Laurent from CHU de Lyon for the antibacterial tests, and Prof. F. Quaglia from Unversità di Napoli for the film preparation.

Merci Aurore, for helping me on my first steps in the laboratory, and funny moments that I am not going to tell in here. Grazie to Nino and Ivana, for sharing with me stressing afternoons stuck in the lab, and puases coffee-cigarettes. Muito obrigado Damien, for teaching me more than you thought. Grazie also to the students who share the laboratory during the last three years, in particular to my students, Tamara and Martina, I learned a lot by teaching you. I am so grateful with my PhD colleges from all the cycles, and the researchers at university, you have been a nice support and better company. Thanks to all the professors whom helped me with an advice, an instrument, or even a coffee, the simplest gesture can cheer up your day. With a special mention to Carmela and Francesca, for her words of wisdom when everything seemed lost, again and again. I am also grateful to Sabrina and Fabio, for being always available to make our bureaucratic issues simpler. Thanks to Portineria's people, not only staff, but also friends. I am deeply indebted to Didattica's team, for the

material and personal support that I received from them. I acknowledge Dr. J.L. Cenis for our email conversations, look forward to working together quite soon.

Grazie al mio sole, che mi ha portato luce quando tutto era buio, che mi ha fatto sentire forte quando ero indebolita, che mi ha guarito quando ero ferita. Grazie Lorenzo. E grazie anche alla sua intera famiglia, che mi ha accolto come una di loro. Voglio ringraziare anche Natasha, Leandro e il non così piccolo Zion, per fare diventare il Macondo un luogo d'incontro per personaggi come Valegrillo, o Ray.

Gracias a la gente de cafeta, todos aquellos con los que compartí y compartieron conmigo apuntes y tardes de estudio. Y de no tan estudio, verdad Gema? Gracias a toda mi familia de la nocturnidad y alevosia, en especial a la gente del Calaveras, de los cuales muchos entraron como clientes y se han quedado para siempre como amigos. Gracias a La Puta Jungle y todo su séquito por momentos inolvidables, cada vez que vuelvo hacéis que me sienta especial. I am thankful also to my Roller Derby's sisters, specially from Sigonella Ash Kickers, for making me really feel that I belong to the team.

I am so grateful to my family: Papá y Mamá por haberme enseñado (o intentado) disciplina y tenacidad, a mis hermanos, Laura y Sergio por compartir juegos y secretos. A mis abuelos, en especial a mi padrino, Pedro, el cual creo que hubiera estado muy orgulloso de ver cuanto he crecido. A mis tíos Jai e Isa, y por supuesto a Raúl, por interminables tardes de risas en casa de los abuelos. Al clan Marco y arrejuntados (¡no cabéis todos!) por todas las aventuras que se seguirán contando en la bodega año tras año, y a Magüevo aunque no sea del clan. Gracias a todos.